



## REMOVAL OF PHARMACEUTICALS FROM WATER USING MODIFIED BIOCHAR

Lappeenranta–Lahti University of Technology LUT

Master's in Chemical Engineering and Water Treatment, Master's Thesis

2022

Kanchan Nakarmi

Examiner(s): Professor Amit Bhatnagar

Ehsan Daneshvar, Ph.D.

## ABSTRACT

Lappeenranta–Lahti University of Technology LUT  
LUT School of Engineering Science  
Chemical Engineering and water treatment

Kanchan Nakarmi

### Removal of pharmaceuticals from water using modified biochar

Master's thesis

2022

80 pages, 30 Figures and 13 Tables

Examiner(s): Professor Amit Bhatnagar and Ehsan Daneshvar, Ph.D.

Keywords: Microalgal biochar, modification, diclofenac, ciprofloxacin, adsorption, isotherm, kinetics, fixed bed studies, water treatment.

The production of microalgae in wastewater is a sustainable method to obtain microalgal biomass because it biofixes carbon while remediating wastewater. The microalgae can then be pyrolyzed to produce valuable products such as biochar, bio-oil, and syngas after extracting high-value products. Microalgal biochar received attention as a potential adsorbent material because it contains diverse oxygen-containing and nitrogen-containing functional groups which interact with pollutants. In the algal harvesting process, coagulation with  $\text{FeCl}_3$  is used, which is a cheap and efficient method and provides iron-containing microalgal biomass. The iron containing microalgal biomass can be used to synthesize iron modified biochar with improved adsorption performance.

In this study, biochar synthesized from iron-containing (Fe-MA) and iron-free (MA) microalgal biomass and used for adsorption of ciprofloxacin (CIP) and diclofenac (DIC) from water. Screening tests were conducted to determine the best biochar based on highest adsorption performance. The best biochar material was used for batch and continuous adsorption studies. In batch studies, adsorption process parameters were optimized. Then, the adsorption isotherms and kinetics were studied. Further, its adsorption performance was compared with commercial activated carbon and evaluated in presence of competing ions. In continuous adsorption studies, breakthrough curves were used to evaluate the performance of adsorption column. The iron-free biochar and iron-containing biochar (before and after adsorption) were characterized to determine physicochemical properties of biochar and to verify adsorption.

The results showed that biochar prepared at 750 °C from iron-containing biomass (FBC 750W) had the best adsorption performance. Characterisation studies showed that the presence of iron enhanced specific surface area, pore volumes and formed iron carbide/zero-valent iron. The maximum adsorption capacity of FBC 750W was **75.97 mg/g for CIP** and **40.99 mg/g for DIC** and kinetics data followed Elovich model. The **equilibrium** occurred within **150 min for CIP** and **180 min for DIC**. Continuous adsorption studies were conducted using fixed beds filled with FBC 750W and had maximum bed capacities of **40.67 mg/g for CIP** and **24.69 mg/g for DIC**. Therefore, this study shows that iron present in microalgae coagulated with  $\text{FeCl}_3$  can be used to synthesize Fe modified biochar which has potential use for adsorptive removal of pharmaceuticals from water.

## ACKNOWLEDGEMENTS

First and foremost, I am deeply grateful for Prof. Amit Bhatnagar for providing me the opportunity to work in this interesting project. I would like to extend my gratitude to Ehsan Daneshvar (Ph.D), who became my mentor during this work. I am especially thankful towards them for guiding me and providing me practical suggestions, valuable feedbacks, insights, advice, and encouragement during each stage of my work which helped me tremendously in completing my work.

Many thanks to Liisa Puro, Ghada Mohamed and Nikolai Ponomarev, who helped me with analyses regarding characterization studies. I very much appreciate Ghada and Nikolai for providing me guidance to interpret the BET, XRD and FTIR results. I would also like to take this opportunity to thank Pimchanok Ieamviteevanich with whom I had pleasure working with and I learned a lot from her past laboratory experience.

Special thanks to our research team in Mikkeli for welcoming me during my stay in Mikkeli and for the fun and memorable moments. Also, thanks to the staffs at the Mikkeli laboratory for technical assistance

Last but not the least, I would also like to take this opportunity to thank my family and friends who provided me moral support and encouragement during my work.

Kanchan Nakarmi

Mikkeli, 2022

## SYMBOLS AND ABBREVIATIONS

### Roman Characters

Symbols	Description	Units
$A$	Cross-sectional area of the column	[cm <sup>2</sup> ]
$c$	Intercept value for intraparticle diffusion model	[mg/g]
$C$	Concentration	[mg/L]
$h$	Fractal like Bohart-Adam's homogeneity factor	
$k_1$	Pseudo first order rate constant	[1/min]
$k_2$	Pseudo second order rate constant	[g/mg/min]
$K_{BA}$	Bohart-Adam's rate constant	[L/mg/min]
$K_{BA0}$	Fractal like Bohart-Adam's rate constant	[L/mg/min <sup>(1-h)</sup> ]
$K_F$	Freundlich constant	[(mg/g) (L/mg) <sup>1/n</sup> ]
$K_{ID}$	Intraparticle diffusion rate constant	[mg/g/min <sup>0.5</sup> ]
$K_L$	Langmuir constant	[L/mg]
$K_S$	Sips constant	[L/mg]
$K_{ow}$	Octanol-water partition coefficient	
$m_{ads}$	Mass of adsorbent	[mg]
$M_{tot}$	Total mass of adsorbate in a solution	[mg]
$n$	Freundlich adsorption intensity parameter	
$N_0$	Bed capacity	[mg/L]
$n_s$	Sips exponential factor	
$pK_a$	Ionisation constant	
$Q$	Volumetric flowrate	[mL/min]
$q$	Equilibrium adsorption capacity	[mg/g]
$R^2$	correlation coefficient	
$R_L$	Langmuir separation factor	
$t$	Time	[min]
$u$	Superficial velocity	[cm/min]
$V$	Volume of solution	[mL]
$Z$	Bed height	[cm]

## Greek characters

Symbols	Description	Units
$\alpha$	Elovich initial adsorption rate	[mg/g/min]
$\beta$	Elovich desorption constant	[g/mg]
$\tau$	Time to reach 50% breakthrough	[min]
$\lambda$	Wavelength	[nm]

## Subscripts

$b$	Fixed bed
$t$	effluent or at time “t”
$e$	At equilibrium
$f$	final
$i$	Influent or initial
$m$	Maximum
$zpc$	Zero-point of charge
$eff$	effluent

## LIST OF ABBREVIATIONS

BET	Brunauer, Emmett and Teller
CIP	Ciprofloxacin
C-AC	Commercial activated carbon
DI	De-Ionised
DIC	Diclofenac
EC <sub>10</sub>	10% maximal effective concentration
EC <sub>50</sub>	Half maximal effective concentration
EDS	Energy dispersive x-ray spectroscopy
FBC	Fe modified microalgal Biochar
FTIR	Fourier Transformed Infra-Red
IUPAC	International Union of Pure and Applied Chemistry
MTZ	Mass Transfer Zone
MA	Microalgae

Fe-MA	Iron containing Microalgae
LOEC	Lowest Observed Effect Concentration
MBC	Microalgal Biochar
NOEC	No Observed Effect Concentration
PFO	Pseudo-First Order
PSO	Pseudo-Second Order
R.E. %	Removal Efficiency %
sBET	Surface area from BET analysis
SEM	Scanning Electron Microscope
RMSE	Root Mean Squared Errors
UV-vis	Ultra-Violet and visible light
XRD	X-Ray diffractometer
ZVI	Zero Valent Iron

## Table of Contents

Abstract

(Acknowledgements)

(Symbols and abbreviations)

1	Introduction.....	9
2	Literature review.....	12
2.1	Adsorption: Theory .....	15
2.1.1	Dynamic equilibrium .....	16
2.1.2	Basis of separation .....	17
2.1.3	Adsorbent properties .....	18
2.1.4	Pharmaceutical properties.....	20
2.2	Adsorption batch studies .....	22
2.2.1	Adsorption isotherms .....	23
2.2.2	Adsorption kinetics .....	24
2.3	Continuous adsorption studies: Fixed bed .....	27
2.3.1	Bohart-Adams model.....	29
2.3.2	Fractal-like Bohart-Adams model .....	30
2.4	Modified biochar .....	31
2.4.1	Microalgae as precursor for biochar .....	31
2.4.2	Effect of pyrolysis condition.....	33
2.4.3	Synthesis of iron modified biochar/ Fe-biochar composites. ....	36
3	General aims and objectives .....	40
4	Methodology .....	42
4.1	Materials and chemicals .....	42
4.2	Biochar preparation .....	43
4.3	Preparation of solutions and standard curves .....	43

4.4	Batch tests .....	44
4.4.1	Screening tests .....	45
4.4.2	Optimization study.....	46
4.4.3	Kinetic study .....	46
4.4.4	Isotherm study.....	47
4.4.5	Effect of competing ions.....	47
4.5	Continuous adsorption studies .....	47
4.6	Biochar characterization.....	50
5	Results and Discussions.....	51
5.1	Characterization .....	51
5.1.1	Specific surface area and pore characteristics .....	51
5.1.2	Surface morphology.....	54
5.1.3	Elemental composition .....	57
5.1.4	Surface functional groups .....	59
5.1.5	X-Ray diffraction .....	61
5.2	Batch tests .....	64
5.2.1	Screening test.....	64
5.2.2	Optimization studies .....	65
5.2.3	Adsorption Kinetics .....	72
5.2.4	Adsorption Isotherm .....	76
5.2.5	Comparison with commercial granular activated carbon .....	77
5.2.6	Effect of competing ions.....	79
5.3	Continuous adsorption studies .....	81
6	Conclusions.....	87
	Reference .....	90



# 1 Introduction

Water is quintessential for life and a renewable resource on Earth. However, anthropogenic activities have added different pollutants to the water bodies causing water pollution. Additionally, development in analytical technology has allowed the identification of many trace pollutants present in water that was previously not observed (Crittenden et al., 2012). Such pollutants that are unregulated by current environmental laws but have potential implications on health and the ecosystem are known as emerging contaminants (Crittenden et al., 2012; Parida et al., 2021). Pharmaceuticals and personal care products are a class of such pollutants (Daughton et al., 1999) that are now being detected in every environmental water (Patel et al., 2019). Wastewater disposal is the main source of pharmaceuticals in the environment (Daughton et al., 1999; Patel et al., 2019). Moreover, conventional wastewater treatment technologies are inefficient in complete removal of pharmaceuticals (Clara et al., 2005). Besides wastewater disposal, reuse and reclamation of wastewater are currently being encouraged for mitigating water scarcity (UNESCO, 2017). Here, the wastewater reuse for irrigation is already well established (Rizzo et al., 2020). So, subtle effects associated with the presence of pharmaceuticals in water over public health safety and environmental protection have raised concerns (Daughton et al., 1999; Rizzo et al., 2020). Therefore, low-cost, and efficient wastewater treatment technologies are required to eliminate pharmaceuticals from water.

Adsorption has gained wide interest for the removal of a variety of pollutants from water and wastewater. It is a simple phase separation process that removes pollutants (adsorbate) from water using a solid material (adsorbent), without generating secondary pollutants in the water. The selection of a proper adsorbent is a crucial step for any adsorption process as it can affect the cost, efficiency, and sustainability of the process (Piccin et al., 2017). Currently, activated carbon is used for the adsorptive removal of broad range of pollutants from water, however, its high costs and difficult regeneration has led researchers to seek alternative low cost adsorbents (De Andrade et al., 2018; Cheng et al., 2021; Krasucka et al., 2021). Recently, biochar has received much attention for the adsorption of emerging contaminants, especially antibiotics (Cheng et al., 2021; Krasucka et al., 2021).

Biochar is a porous carbonaceous residue obtained after pyrolysis of biomass, in an oxygen-free atmosphere. It is an environment-friendly and cheaper alternative to expensive activated carbon, for water treatment (De Andrade et al., 2018) because it requires lower energy for production and has net-negative greenhouse gas emissions (Dai et al., 2019). Moreover, waste biomass such as agricultural waste, forestry waste, municipal solid waste, and sludge from biological wastewater treatment plants can be used to synthesize biochar (Ok et al., 2018; Dai et al., 2019; Singh et al., 2021). Even though biochar has environmental and economic benefits, biochar with high adsorption performance is required (Singh et al., 2021). Adsorption performance is dependent upon the physiochemical properties of adsorbate and adsorbent (Yang et al., 2010). Recently, utilisation of microalgal biochar has gained attention for the adsorptive removal of pollutants from water because it is rich in oxygen-containing and nitrogen-containing functional groups which can interact with a wide range of organic pollutants (Leng et al., 2019; Kwon et al., 2020).

Further, utilising microalgae for biochar synthesis can be a sustainable option (Singh et al., 2021). This is because microalgae can be grown in nutrient-rich wastewater where they can bio-fix a high amount of carbon dioxide into organic matter through photosynthesis (Goswami et al., 2021). Additionally, they have high growth rate and short life span (Goswami et al., 2021). Therefore, microalgal biomass can be rapidly replenished while sequestering carbon and treating wastewater. Lastly, microalgae, after harvesting, can be used in a biorefinery to produce valuable bioproducts such as biofuel, syngas, and biochar (Yu et al., 2017). Therefore, microalgal biorefinery could be integrated with wastewater treatment plant for economic and environmental benefits (Goswami et al., 2021) and the biochar can be used for advanced treatment of wastewater.

Pristine biochar has lower adsorption potential and scope compared to activated carbon (Cheng et al., 2021; Singh et al., 2021). Therefore, they are often modified via different physical, chemical or biological processes to create modified biochar which can have higher adsorption performance or different functional properties. One of the modification methods involves using iron salts as biomass feedstock additive before pyrolysis to create iron modified biochar. The presence of iron and pyrolysis temperature are two key parameters that affect the physiochemical properties of biochar (Krasucka et al., 2021; Li et al., 2021b). The pyrolysis temperature affects the speciation of iron on iron modified biochar. At low

pyrolysis temperatures (500-600 °C) iron oxides are formed whereas at high temperatures (>600 °C) iron carbide and zero-valent iron are formed (Hoch et al., 2008). Also, at high temperatures (>600 °C) presence of iron can increase specific surface area, pore structures, graphitization degree and hydrophobicity of biochar which could be beneficial for adsorption of pharmaceuticals (Xia et al., 2019; Li et al., 2021b). Previously, modified biochar was synthesized by pyrolysis of biomass with  $\text{FeCl}_3$  at 800 °C which had higher adsorption capacity for nitrobenzene than pristine biochar (Liu et al., 2021). Additionally, pyrolysis of biomass with iron salt promotes formation of gaseous products (Xia et al., 2019) which could be combusted to supplement energy requirements of the pyrolysis process (Wurzer et al., 2021).

One of the bottlenecks for microalgal biomass utilization is the harvesting of microalgae from their cultivation media (Singh et al., 2018; Goswami et al., 2021). Current prevalent harvesting methods for microalgae are centrifugation, coagulation-flocculation, filtration, sedimentation and floatation (Singh et al., 2018). Within the given harvesting techniques, coagulation-flocculation is an inexpensive and fast harvesting technique that can harvest microalgae from large volumes of water (Singh et al., 2018). However, microalgal biomass becomes contaminated with coagulant. Previously, microalgae from harvested via coagulation with  $\text{FeCl}_3$  contained iron (Daneshvar et al., 2020). The iron containing microalgae can be used as a precursor to produce Fe-modified biochar.

Accordingly, the main aim of this study is to investigate the adsorption of diclofenac and ciprofloxacin from water onto Fe modified microalgal biochar. The upcoming chapter, chapter 2, will guide the readers through past literature about pharmaceuticals in water bodies and their emerging concerns, the theory of adsorption including all the equations used in this study and literature on modified biochar. Chapter 3 describes the conceptual framework and states aims and objectives of this work. Chapter 4 describes the methods used to prepare adsorbent material (biochar), its characteristics and adsorption performance in detail. Chapter 5 presents the results obtained in this study and discusses it based on past literature. Finally, chapter 6 provides the conclusion of this thesis and future recommendations, respectively.

## 2 Literature review

Pharmaceuticals represent a broad range of chemicals used for medicinal purposes for humans and animals. Despite their medical importance, they have become contaminants of emerging concern in water. Pharmaceuticals are detected in every environmental matrix and their concentration varies from a few ng/L to hundreds of µg/L (Patel et al., 2019). Wastewater disposal is the main contributor for the environment contamination with pharmaceuticals. The presence of pharmaceuticals in wastewater has been traced back to their consumption-excretion and production (Yang et al., 2017; Patel et al., 2019). In wastewater effluents, pharmaceuticals are present as original parent molecules and their metabolites (Yang et al., 2017; Patel et al., 2019). Furthermore, different physicochemical processes and microbial activity can form various transformation products of pharmaceuticals in water. The pharmaceutical and their transformation products have different ecotoxic potentials, thus raising concerns over environmental and human health security (Maculewicz et al., 2021).

Diclofenac and ciprofloxacin are amongst the frequently encountered pharmaceuticals in wastewater and environmental waters (De Andrade et al., 2018; Sousa et al., 2018; Patel et al., 2019). Diclofenac (DIC) is a common non-steroidal anti-inflammatory drug used for humans and veterinary purpose (Patel et al., 2019). It was proposed as a priority pollutant under European Water Framework Directive (2000/60/EC) and was included in the watchlist of substances by directive 2013/39/EU (Patel et al., 2019). Ciprofloxacin (CIP), on the other hand, is a globally used broad-spectrum antibiotic (Ebert et al., 2011).

The concentration levels of diclofenac and ciprofloxacin varies greatly in depending of the source of water (Vieno et al., 2014; Yang et al., 2017; Patel et al., 2019). The wastewaters have highest concentration of pharmaceuticals followed by surface water, ground water and drinking water. Amongst different types of wastewaters, industrial wastewater effluent (especially from drug manufacturing plants) and hospital wastewater effluents have the highest concentration of pharmaceuticals. For example hospital wastewater in Passo Fundo, Brazil, contained diclofenac and ciprofloxacin at a concentration of  $19.82 \pm 0.054$  mg/L and  $2.14 \pm 0.125$  mg/L, respectively (Vieira et al., 2021). Eventually, the wastewater is disposed

into the environmental water bodies either with or without treatment. Here, conventional wastewater treatment plants have limited removal efficiency for diclofenac and ciprofloxacin because they are poorly biodegradable (Vieno et al., 2014; Sodhi et al., 2021). Also, the existing conventional wastewater treatment plants (activated sludge processes) were designed for the removal of nutrients, suspended solids, and organic matter (Yang et al., 2017; Patel et al., 2019). So, eventually in either case, diclofenac and ciprofloxacin end up in the environmental waters.

The concentration of diclofenac and ciprofloxacin in environmental water bodies are usually low, between few ng/L to several hundreds of  $\mu\text{g/L}$ . These variations are due to different consumption patterns and efficiency of wastewater treatment plants (Patel et al., 2019). Also, discharge of untreated or poorly treated wastewater will contaminate surrounding water to a much higher degree. For example, in India, wastewater effluent from a wastewater treatment plant, which received wastewater from 90 pharmaceutical producing industries, had many types of antibiotics and the ciprofloxacin concentration was up to 14 mg/L (Fick et al., 2009). The wastewater was discharged into nearby aquatic bodies and the two lakes receiving the effluent had up to 6.5 mg/L ciprofloxacin along with varying concentrations of other pharmaceuticals. There are many degradation pathways for pharmaceuticals in the environment, such as sorption, biodegradation, photolysis, and hydrolysis, which help in the natural attenuation of pharmaceuticals (Patel et al., 2019). However, the continuous discharge of wastewater have made pharmaceuticals pseudo-persistent which raised concerns over chronic effects of trace level contamination (Yang et al., 2017).

The chronic exposure to environmentally relevant concentration levels ( $<500\text{ ng/L}$ ) of diclofenac can already cause ecotoxicity to different aquatic organisms (Vieno et al., 2014). For example, chronic exposure (28 days) to 5  $\mu\text{g/L}$  diclofenac damaged kidney and gills of rainbow trout (Schwaiger et al., 2004). Furthermore, after 28 days, the diclofenac had also accumulated in their liver, kidney, and gills. Moreover, transformation and degradation products of pharmaceuticals can still have toxic effects on aquatic organisms (Maculewicz et al., 2021). In this regard, biotransformation products of diclofenac, diclofenac methyl ester, was found to be more toxic and had higher bioaccumulation potential compared to the original compound (Fu et al., 2020).

On the other hand, antibiotics are produced for a specific purpose but their continuous disposal in environment can be toxic for non-target microbes. For example, median effective concentration (EC50) of ciprofloxacin on biomass yield and growth rate of cyanobacteria (*Anabaena flos-aquae*) and sea weed (*Lemna minor*) can be as low as 10.2 µg/L and 62.5 µg/L, respectively (Ebert et al., 2011). According to another study, chronic exposure to ciprofloxacin was toxic to the bacterial part of periphyton communities and the 10% of maximal effective concentration (EC10) and no observed effect concentration (NOEC) of ciprofloxacin on the inhibition of carbon uptake and utilization were 46.1 nmol/L (15 µg/L) and 26 nmol/L (8.6 µg/L), respectively (Johansson et al., 2014). Thus, pollution of water with ciprofloxacin could alter the microbiological distribution. Additionally, water bodies contaminated with antibiotic can develop antibiotic resistant bacteria (Sodhi et al., 2021) which raises the concerns over development of antibiotic resistant pathogen in the environment.

Therefore, removal of pharmaceutical compounds from wastewater before discharge is extremely important for environmental and public health safety. It is a well-established idea that augmentation of conventional wastewater treatment processes with advanced technologies such as oxidation and adsorption or hybrid water treatment method such as membrane bioreactors are necessary to remove pharmaceuticals (Vieno et al., 2014; Patel et al., 2019; Sodhi et al., 2021). Amongst these advanced technologies, adsorption has received a lot of interest from researchers because it is a low-cost technology and easy to operate.

## 2.1 Adsorption: Theory

Adsorption is a phenomenon that occurs in the interfacial region between two immiscible phases where at least one phase is continuous, for example, gas-solid, liquid-solid, liquid-liquid, and gas-liquid (Dąbrowski, 2001). During adsorption, molecules, ions, and particles are concentrated or adsorbed onto the interfacial region between these two bulk phases (Sing et al., 1985; Rouquerol et al., 2014a). In the case of water treatment, adsorption is studied at the solid-liquid interface. The terms often used in adsorption processes are presented in Figure 1 (Worch, 2012).

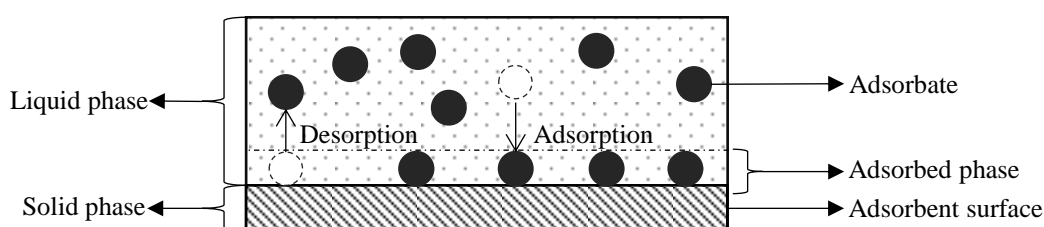


Figure 1 Basic terms used in Adsorption.

According to Figure 1, the black spheres represent pollutant molecules, ions or particles in the liquid phase which are adsorbed on the interface of the solid phase due to some affinity or interaction. The solid phase is referred to as adsorbent and the species that have been adsorbed are called adsorbates. Also, the adsorbate molecules before adsorption are called adsorptive (Sing et al., 1985; Rouquerol et al., 2014a). For reversible adsorption processes, the detachment of adsorbates from the adsorbent surface back to the liquid bulk is known as desorption. On the contrary, if adsorbate molecules are concentrated within the bulk of the solid phase, then term absorption is used (Dąbrowski, 2001). When adsorption and absorption processes occur simultaneously and becomes indistinguishable from each other, then the combined process is termed as sorption (Dąbrowski, 2001).

The sites on the adsorbent surface that have the potential to interact with adsorbate molecules are known as energy active adsorption sites. The interaction of adsorbate and adsorbent arises due to a match in the spatial and electronic configuration between these two species. Here, the adsorption sites have available space/suitable dimensions for adsorbate molecules, and they have electronic compatibility. Also, based on adsorbate-adsorbent interaction, the

adsorption processes are classified into two groups: physisorption and chemisorption (Sing et al., 1985; Worch, 2012; Rouquerol et al., 2014a).

Physisorption is a general non-specific phenomenon (Rouquerol et al., 2014a) where molecules are adsorbed via weak interactions such as van der Waals forces, dipole interactions and hydrophobic interactions (Piccin et al., 2017). Chemisorption is analogous to chemical reaction (Rouquerol et al., 2014a) where transfer of electrons occur to form chemical bonds between adsorbate and adsorbent (Piccin et al., 2017). The classification of adsorption processes into chemisorption and physisorption based on enthalpy has been specified before (Worch, 2012), where, enthalpy less than or equal to 50 kJ/mol is considered as physisorption and enthalpy greater than 50 kJ/mol is known as chemisorption. However, the enthalpy values used for the classification of adsorption are not always exact (Piccin et al., 2017). According to Rouquerol *et al.* (2014), physisorption has lower energy consumption, always exothermic and the enthalpy changes are like that of condensation of adsorptive molecules. On the other hand, chemisorption can be either exothermic or endothermic with enthalpy changes comparable to chemical bond formation. Due to chemical bonding between adsorbate molecules and adsorbent surface, chemisorption forms an irreversible monolayer of adsorbate on the adsorbent surface, and desorption can alter the molecular structure of adsorbate. In the case of physisorption, multilayer build-up is possible which is reversible and desorption doesn't alter the molecular structure of adsorbate. (Rouquerol et al., 2014a).

### 2.1.1 Dynamic equilibrium

The process of adsorption onto the surface of porous adsorbent is divided into 4 distinct stages or steps (Worch, 2012). They are:

- i) **Bulk transport:** Transport of adsorbates molecule or ions in the bulk of water towards the hydrodynamic boundary layer surrounding the adsorbent surface.
- ii) **External diffusion or film diffusion:** Diffusion/transfer of adsorbate molecules or ions through the hydrodynamic boundary layer to the adsorbent surface.
- iii) **Internal diffusion or Intraparticle diffusion:** Diffusion of adsorbate molecules or ions through the porous network within adsorbent particles and into the pores.



- iv) **Adsorption:** Adsorption of the adsorbate molecules or ions onto the surface of the adsorbent by physical or chemical interaction.

Amongst these four steps, bulk diffusion and adsorption are relatively fast steps whereas external diffusion and internal diffusion are slower processes. In the case of reversible adsorption systems, desorption occurs simultaneously with the adsorption. In the early stages, the adsorption rate is fast due to the vacant adsorbent surface. As time progresses, the surfaces start to fill up. So, the desorption rate increases while the adsorption rate decreases. Eventually, a state of equilibrium is achieved where the adsorption rate is equal to the desorption rate. At this state, the adsorbate concentration in the liquid phase and solid phase will become virtually constant and are termed as equilibrium concentration ( $C_e$ ) and equilibrium adsorption capacity ( $q_e$ ), respectively.

#### 2.1.2 Basis of separation

There are three main bases of separation for the adsorptive removal of pollutants. They are as follows (Do, 1998):

1. **Steric separation:** It occurs due to the pore structures and 3D geometry of the adsorbate. Here, only the adsorbate molecules that can traverse the pore network of the adsorbent are separated and molecules that are too large might not be effectively removed as they are sterically hindered from reaching adsorption sites.
2. **Equilibrium separation:** In this case, the adsorbate that can form stronger/ stable interaction with the adsorbent is separated preferentially, from a multicomponent solution.
3. **Kinetic separation:** Here, the adsorbate molecules or ions that have higher diffusivity are separated preferentially because they will occupy the adsorption sites quickly making them unavailable for slowly diffusing molecules or ions.

According to Yang and Xing (2010), adsorption capacity and adsorption affinity are two integral parts of describing an adsorption process. The available space on adsorbent surface describes the adsorption capacity whereas the forces of attraction between adsorbate and adsorbent define the adsorption affinity. Consequently, understanding physicochemical

characteristics of adsorbate and adsorbent can help to describe an adsorption process. Likewise, designing an efficient biochar should consider the steric compatibility as well as adsorbate-adsorbent affinity.

### 2.1.3 Adsorbent properties

Generally, an adsorbent is required to have high adsorption capacity, selectivity, or removal efficiency of the target compound. Other desirable properties of a good adsorbent materials, include physicochemical stability during practical application, low cost, widely available, and reusable (Piccin et al., 2017). Nevertheless, the two key properties that govern adsorbent quality and affect adsorption process are specific surface area and surface functional groups.

#### *Specific Surface area*

Specific surface area is defined as the surface area of a gram of adsorbent and is expressed as  $\text{m}^2/\text{g}$ . Adsorption is an interfacial phenomenon, so, specific surface area determines the potential space available for adsorption of an adsorbate or the potential adsorption capacity (Yang et al., 2010). Therefore, an adsorbent with a high specific surface area is preferred (Kwon et al., 2020). Specific surface area is affected by porosity, particle size, shape, and surface smoothness (Rouquerol et al., 2014a). The specific surface area increases with increasing porosity and decreasing particle size and surface smoothness. Moreover, pore size and 3D geometry can affect the selectivity of the adsorbent through steric separation (Do, 1998).

According to IUPAC (International Union for Pure And Applied Chemistry), pore size is the internal width of the pore. Pores are classified based on pore sizes as follows (Sing et al., 1985):

1. micropores: pores with internal width  $< 2 \text{ nm}$
2. mesopores: pores with internal width  $2 - 50 \text{ nm}$
3. macropores: pores with internal width  $> 50 \text{ nm}$

Due to molecular dimension of micropores, they usually participate in adsorption of organic pollutants through pore filling, whereas mesopores and macropores can form multi-layer

adsorption. Also, the majority of micropore volumes are occupied after adsorption of organic molecules while only fraction of mesopore and macropore are utilised. Therefore, a desirable adsorbent contains a high micropore volume and well-developed pore networks that makes micropores accessible for adsorption of pollutants (Dąbrowski, 2001).

### ***Surface functional groups***

Functional groups are a group of chemicals in a molecule that have distinct chemical properties. The surface functional groups affect affinity, electronic compatibility and interaction between adsorbate molecules and adsorbent surface (Yang et al., 2010; Patel et al., 2019; Cheng et al., 2021). Therefore, they are another key property of adsorbent that determines its adsorption potential for a given adsorbate molecules or ions. Biochar can have different oxygen and nitrogen containing functional groups which interact with pharmaceutical molecules (Cheng et al., 2021). Commonly encountered functional groups are tabulated in Table 1.

Table 1. Examples of different types of functional groups. (Patel et al., 2019)

<b>Functional group</b>	<b>Molecular formula</b>
<b>Carboxyl group</b>	R-COOH
<b>Carbonyl group</b>	R-COR'
<b>Hydroxyl group</b>	R-OH
<b>Phenyl group</b>	R-C <sub>6</sub> H <sub>5</sub>
<b>Amine group</b>	R-NR'R''

\*Here, R, R' and R'' refers to aliphatic carbon, aromatic carbon or hydrogen.

Recognizing available functional groups and the chemical composition of biochar's surface can help predict possible interactions during adsorption. For example, hydroxyl groups can form hydrogen bonds, aromatic/graphitic carbon can form  $\pi$ - $\pi$  electron donor acceptor interactions, polar functional groups can participate in dipole-dipole interactions, acidic and basic functional groups can participate in neutralization reactions (Patel et al., 2019; Cheng et al., 2021). On the other hand, the lack of polar functional groups in adsorbent makes it hydrophobic which can adsorb non-polar pollutants through hydrophobic interactions (Patel et al., 2019; Cheng et al., 2021). Furthermore, different chemical reactions can take place where adsorbate molecules or ions are chemisorbed onto the surface of biochar (Patel et al., 2019; Cheng et al., 2021). Apart from organic functional groups mentioned in Table 1,

different metals and inorganic substances can intercalate within biochar structures which affect the biochar's surface chemistry (Patel et al., 2019; Cheng et al., 2021).

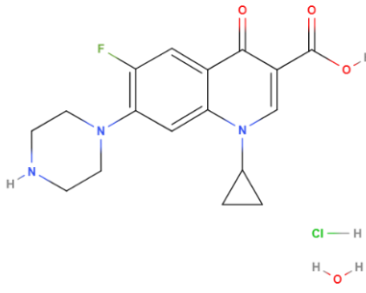
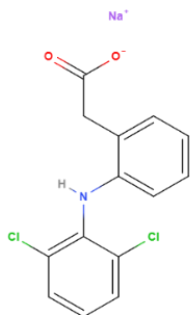
The functional groups also affect the surface charge of biochar when placed in an aqueous solution and thus affecting electrostatic interaction between adsorbate molecules or ions and the adsorbent surface. The solution pH at which the adsorbent's surface charge becomes zero is called zero-point charge pH ( $\text{pH}_{\text{zpc}}$ ) of the adsorbent. The relationship between, solution pH,  $\text{pH}_{\text{zpc}}$  of biochar and surface charge is as follows (Patel et al., 2019):

1.  $\text{pH} > \text{pH}_{\text{zpc}}$ , surface is negatively charged.
2.  $\text{pH} = \text{pH}_{\text{zpc}}$ , surface is neutral
3.  $\text{pH} < \text{pH}_{\text{zpc}}$ , surface is positively charged.

#### 2.1.4 Pharmaceutical properties

Apart from adsorbent properties, adsorption process also depends on the adsorbate's physiochemical properties. The properties of ciprofloxacin and diclofenac are presented in Table 2. The molecular structures of pharmaceuticals were drawn with help of an online webapp, MolView (<https://molview.org/>). According to the molecular structure, both ciprofloxacin and diclofenac are organic molecules rich in functional groups. Ciprofloxacin consists of carbonyl, carboxylic, and fluoride whereas diclofenac possesses amine, chloride, and carboxylic acid groups. Such polar functional groups could interact with oxygen containing functional groups of biochar, through dipole-dipole interactions and hydrogen bonds (Krasucka et al., 2021; Singh et al., 2021). Further, the carboxylic acid groups in pharmaceuticals can interact with alkaline biochar and adsorb through Lewis acid-base interaction (Shirani et al., 2020). Additionally, both types of molecules contain aromatic carbon rings with electron withdrawing group such as fluorine and chlorine. Therefore, the electron deficient aromatic groups of the pharmaceutical can interact with graphitic carbon of biochar through  $\pi$ - $\pi$  electron donor acceptor interaction (Krasucka et al., 2021; Patel et al., 2021).

Table 2. Chemical properties of ciprofloxacin and diclofenac (CHEMSRC, 2020).

Descriptor	Ciprofloxacin hydrochloride hydrate	Diclofenac (Sodium salt)
Molecular structure		
Molecular formula	C <sub>17</sub> H <sub>19</sub> ClFN <sub>3</sub> O <sub>3</sub>	C <sub>14</sub> H <sub>10</sub> Cl <sub>2</sub> NNaO <sub>2</sub>
CAS number	86393-32-0	15307-79-6
Molecular weight [g/mol]	385.82	318.13
Melting point [°C]	318-320	288-290
pK <sub>a</sub>	6.09, 8.64	4.15
Log K <sub>ow</sub>	2.72	3.10

Apart from interaction of functional groups, adsorption process also depends on the solution pH. The charge on a pharmaceutical molecule in water is determined by the solution pH and the ionization constant, pK<sub>a</sub>, value of the compound (Dordio et al., 2015). Ciprofloxacin has two pK<sub>a</sub> values at 6.09 and 8.64 (Carabineiro et al., 2012). Below pH 6.09, ciprofloxacin has positive charge, at pH between 6.09 and 8.64 it is amphoteric and at pH above 8.64 it is negatively charged (Carabineiro et al., 2012). Similarly, pK<sub>a</sub> value of diclofenac is 4.15 (Maged et al., 2021). Therefore, below pH 4.15, diclofenac is protonated and has neutral (Maged et al., 2021). At higher pH, it is deprotonated and is negatively charged (Maged et al., 2021). At a given working pH, adsorption is favoured when biochar and pharmaceuticals have complementary charges (Carabineiro et al., 2012; Keerthanan et al., 2020) or either one should be neutral charged to avoid electrostatic repulsion.

A measure of hydrophobicity of pharmaceuticals is given by its octanol-water partition coefficient (*K*<sub>ow</sub>) value (Dordio et al., 2015). Table 2 gives the logarithm of octanol-water partition coefficient, log *K*<sub>ow</sub> of studied pharmaceuticals. Since both pharmaceuticals have log *K*<sub>ow</sub> higher than 1, they preferentially dissolve in octanol than water and are hydrophobic. Thus, these pharmaceuticals can be separated from their aqueous solutions via hydrophobic interactions.

## 2.2 Adsorption batch studies

Adsorption batch studies are conducted to determine the adsorption performance of an adsorbent on a laboratory scale and may be used in a small-scale treatment plant. The adsorption performance of an adsorbent is affected by working conditions (pH and temperature), adsorbate-adsorbent affinity, characteristics of the adsorbent, and operation parameters (Piccin et al., 2017). In this regard, two key components that determine the adsorption performance are adsorption capacity and removal efficiency.

Adsorption capacity gives an idea of solid-phase concentration as it is the amount of adsorbate adsorbed onto a unit mass of an adsorbent. It is expressed as “mg/g” and denoted by “ $q_e$ ”. The general expression for the determination of adsorption capacity, in a batch process, is shown in equation (1) (Piccin et al., 2017).

$$q_e = \left( \frac{V}{m_{\text{ads}}} \right) * (C_i - C_e) \quad (1)$$

where,  $V$  [L] is the volume of the aqueous phase,  $m_{\text{ads}}$  [g] is the mass of adsorbent,  $C_i$  [mg/L] is the initial concentration of adsorbate and,  $C_e$  [mg/L] is the equilibrium concentration of adsorbate.

The removal efficiency ( $R.E.\%$ ) gives an idea about liquid phase concentration after adsorption (if no transformation products are formed). It is calculated from equation (2).

$$R.E. \% = \left( \frac{C_i - C_e}{C_i} \right) * 100\% \quad (2)$$

At a constant working condition (pH and temperature), the operating parameters such as contact time, adsorbate concentration and adsorbent dosage are optimized to obtain the maximum adsorption performance.

### 2.2.1 Adsorption isotherms

Adsorption isotherm is a graph, where adsorption capacity is plotted as a function of equilibrium concentration. During isotherm experiments working condition such as, pH and Temperature are kept constant (Foo et al., 2010). Isotherm curve are often fitted with empirical models. Together with physicochemical properties of adsorbate and adsorbent, best fitted isotherm model is used to describe probable adsorption mechanism and adsorption capacity (Foo et al., 2010; Piccin et al., 2017). Empirical models used in this study are described in this section.

#### ***Langmuir isotherm model***

Langmuir isotherm model was developed by Langmuir and used to describe the adsorption of gas onto solids (Langmuir, 1917). However, it is now widely used to describe adsorption in slurry systems. According to this model, the adsorbent has distinct adsorption sites with equal affinity for adsorbate. Each site accommodates one adsorbate molecule and after adsorption, they pose no lateral interaction and steric hindrances to neighbouring adsorption sites. Hence, this model describes adsorption where adsorbate molecules and ions form a homogenous monolayer over the adsorbent surface (Foo et al., 2010; Al-Ghouti et al., 2020). It is expressed by equation (3).

$$q_e = \left( \frac{C_e * K_L * q_m}{1 + (C_e * K_L)} \right) \quad (3)$$

where,  $K_L$  [L/mg] is the Langmuir constant and  $q_m$  [mg/g] is the maximum adsorption capacity.

#### ***Freundlich isotherm model***

It was an empirical model derived for adsorption onto adsorbents with heterogeneous surface energies by Freundlich (Freundlich, 1924). Unlike the Langmuir isotherm model, this model describes adsorption onto surface with heterogeneous affinity for adsorbate. Thus, it is not limited to monolayer adsorption. This model is still widely applied in case of heterogeneous adsorption systems, such as the adsorption of organic compounds onto activated carbon. The

Freundlich isotherm model is mathematically expressed as shown in equation (4) (Foo et al., 2010; Al-Ghouti et al., 2020).

$$q_e = K_F * C_e^{\frac{1}{n}} \quad (4)$$

where,  $K_F$  [(mg/g) (L/mg)<sup>1/n</sup>] is the Freundlich constant and  $1/n$  is a dimensionless Freundlich adsorption intensity parameter. Depending on the value of  $1/n$ , the adsorption process can be described as follows: When (a)  $0 < 1/n < 1$  then adsorption is favorable; (b)  $1/n = 1$ , then adsorption is irreversible and (c)  $1/n > 1$  adsorption is unfavorable (Al-Ghouti et al., 2020).

### ***Sips isotherm model***

Sips isotherm model is a three-parameter model (Sips, 1948) which has also been used to describe heterogeneous adsorption systems such as organic compounds on activated carbon (Foo et al., 2010; Al-Ghouti et al., 2020). The mathematical model of Sips is shown in equation (5) (Santhosh et al., 2020).

$$q_e = \frac{q_m * (K_S * C_e)^{n_s}}{1 + (K_S * C_e)^{n_s}} \quad (5)$$

where,  $K_S$  [L/mg] is the Sips equilibrium constant, [L/mg] and  $n_s$  is the Sips exponential factor. Sips isotherm model is a combination of Freundlich and Langmuir isotherm model. At infinite dilution ( $C_e \ll 1$ ), Sips model acts like Freundlich isotherm model. Also, Sips model limits the adsorption capacity at higher concentrations, unlike Freundlich isotherm. When the Sips exponential factor ( $n_s$ ) is unity and the equilibrium concentration ( $C_e$ ) is high it becomes Langmuir model (Al-Ghouti and Da'ana, 2020).

### **2.2.2 Adsorption kinetics**

Adsorption kinetics deals with the rate of adsorption, mass transfer mechanism and maximum adsorption capacity. It is, therefore, important to study kinetics when evaluating the practical application of an adsorbent material. Similar to isothermal studies, kinetic studies utilise kinetic curves where adsorption capacity is plotted as a function of time. Then,



empirical models are fitted to the kinetic curve and based on the best-fitted model, probable the mass transfer mechanism and the rate-limiting step can be determined. Additionally, the model provides kinetic parameters that can help to design and operate a full-scale adsorption processes (Wang and Guo, 2020).

Adsorption kinetic models consists of two sub-groups, they are, adsorption diffusion models and adsorption reaction models. The adsorption diffusion models are further divided to describe three diffusion phases: external diffusion, internal diffusion, and adsorption at active sites. Many complicated diffusional models exist however, they are limited by their complex and difficult use. So, more general empirical models with satisfactory mathematical complexity are often implemented to describe the kinetic behaviour by diffusion, such as the Webber and Morris model. Adsorption reaction kinetics models are empirical models that are developed for the whole duration of the adsorption process and they are based on adsorbate-adsorbent interactions (Qiu et al., 2009; Wang and Guo, 2020).

The adsorption kinetics models, applied in this study and described below.

#### ***Pseudo-first order (PFO) model***

The pseudo-first order equation was first proposed by Lagergren, in 1898, to describe kinetics of adsorption processes in solid-liquid interface (Lagergren, 1898). According to the equation, the adsorption rate is directly related to the remaining adsorption capacity, as given by equation (6):

$$\frac{dq}{dt} = k_1 * (q_e - q_t) \quad (6)$$

where,  $dq_t/dt$  is the adsorption rate [mg/g/min],  $k_1$  [1/min] is the PFO rate constant,  $q_e$  [mg/g] and  $q_t$  [mg/g] are the equilibrium adsorption capacity and adsorption capacity at time, “ $t$ ” mins, respectively. Equation (6) was integrated and rearranged to obtain the non-linear PFO kinetic model as expressed in equation (7) (Wang et al., 2020):

$$q_t = q_e * (1 - e^{-k_1*t}) \quad (7)$$

### ***Pseudo-second order (PSO) model***

Ho and McKay, first used the pseudo-second order equation to describe the kinetics of the chemisorption of dyes onto peat (Ho et al., 1998). According to the equation, the adsorption rate is directly related to the square of residual adsorption capacity as expressed in equation (8):

$$\frac{dq}{dt} = k_2 * (q_e - q_t)^2 \quad (8)$$

where,  $k_2$  [g/mg/min] is the PSO order rate constant. The equation (8) was integrated and rearranged to obtain the non-linear PSO kinetic model, as expressed in equation (9) (Wang et al., 2020):

$$q_t = \frac{(k_2 * q_e^2) * t}{1 + k_2 * q_e * t} \quad (9)$$

### ***Elovich model***

The Elovich model was first used to describe adsorption in a gas-solid adsorption system (Elovich et al., 1962). It is based on a kinetic equation of chemisorption where the adsorption rate decreases exponentially with amount of gas adsorbed (Qiu et al., 2009). This adsorption model assumes that the activation energy is directly related to the contact time and the surface of the adsorbent is heterogenous (Wang et al., 2020). It has been applied to describe the adsorption of metal ions and organic pollutants by solid adsorbents (Qiu et al., 2009; Wang et al., 2020). The Elovich model is shown in the equation (10):

$$q_t = \left(\frac{1}{\beta}\right) * \ln(1 + (\alpha * \beta * t)) \quad (10)$$

where,  $\alpha$  is the initial adsorption rate [mg/g/min] and  $\beta$  desorption rate constant [g/mg]. (Wang et al., 2020)

### ***Intraparticle diffusion model***

An intraparticle diffusion model was formulated by Weber and Morris in 1963 where adsorption capacity was a function of the square root of contact time which is known as the Weber-Morris Intraparticle diffusion model (Weber et al., 1963). Due to its simplicity and

convenient use, it has been widely applied (Wang et al., 2020). The Weber-Morris intraparticle diffusion model is given by the equation (11):

$$q_t = (K_{ID} * t^{0.5}) \quad (11)$$

where,  $K_{ID}$  [ $\text{mg/g/min}^{0.5}$ ] is the intraparticle diffusion rate constant. If intraparticle diffusion is the rate determining step then, the plot of  $q_t$  as the function of  $t^{0.5}$  gives a straight line with zero intercept. Otherwise, external diffusion or a mixture of external and internal diffusion control adsorption kinetics (Qiu et al., 2009; Wang et al., 2020).

### 2.3 Continuous adsorption studies: Fixed bed

Different types of reactors have been used in continuous adsorption processes such as fixed-bed adsorption column, fluidized bed adsorption column, and continuously stirred tank reactors. Among these, the fixed bed adsorption columns have received much attention and are preferred industrially because they are cheap, simple to operate, and control. Thus, many research have been conducted for continuous adsorption of pharmaceuticals using fixed beds (Patel, 2019).

The adsorption kinetics and performance of a fixed bed is determined using a breakthrough curve. The breakthrough curve gives a dynamic concentration profile of effluent. In a fixed-bed column packed with an adsorbent material, adsorbate solution with initial concentration ( $C_i$ ) is passed through the column and effluent with concentration ( $C_t$ ) is obtained. According to the Mass Transfer Zone (MTZ) theory (Piccin et al., 2017; Patel, 2019), at the start, the mass transfer due to adsorption occurs near the influent. As the adsorbate solution moves forward, the adsorption occurs, and the treated effluent passes through the rest of the column. The region where adsorption occurs is also known as the Mass Transfer Zone. As the flow continues, the influent zone saturates, and MTZ shifts forward with the direction of the flow. The saturated adsorbent is in a state of dynamic equilibrium and does not participate in additional adsorption anymore. In the end, the mass transfer zone gradually saturates near the effluent and an increase in final concentration with respect to time is observed. Then, the plot of normalized effluent concentration ( $C_t/C_i$ ) and the operation time gives a characteristic S-shaped curve which is known as the breakthrough curve. Typical terms used to describe

the breakthrough curve are explained with help of an example of a breakthrough curve in Figure 2.

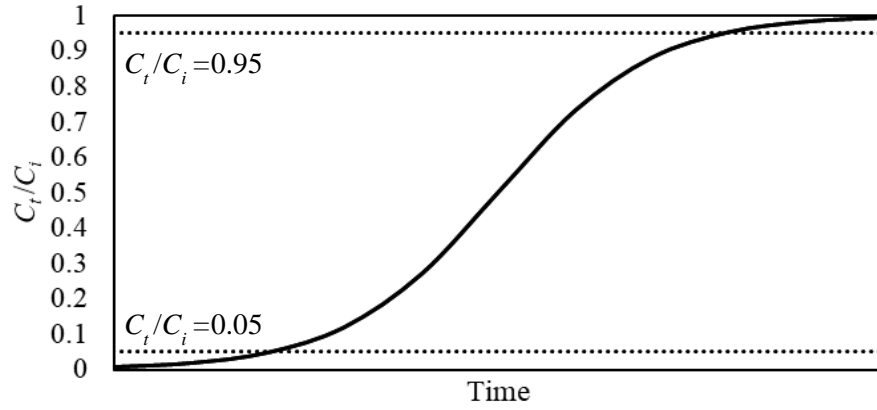


Figure 2. An exemplary breakthrough curve showing breakthrough and exhaustion points.

The breakthrough concentration and exhaustion concentration are the final effluent concentration which is 5% and 95% of the influent concentration, respectively. In Figure 2, dotted lines at  $C_t/C_i = 0.05$  and  $C_t/C_i = 0.95$  indicate breakthrough and exhaustion lines, respectively. Then, the intersection between the breakthrough curve and either of these lines indicate the breakthrough point or the exhaustion point. The slope of the breakthrough curve describes the adsorption kinetics of fixed bed columns. For practical application, a breakthrough curve with a steep slope is preferred as it is associated with high removal efficiency (Alberti et al., 2012; Piccin et al., 2017). Then, the area below breakthrough curve represents the fraction of total adsorbate in the effluent whereas, the area above breakthrough curve represents the fraction of total adsorbate adsorbed within the fixed bed (Piccin et al., 2017). The total amount of adsorbate in the fixed bed is known as the adsorption capacity of the fixed bed or the bed capacity. The bed capacity of a fixed bed is calculated using equation (12) (Piccin et al., 2017):

$$q_b = \frac{Q \cdot C_i \cdot \int_0^t \left(1 - \frac{C_t}{C_i}\right) dt}{1000 \cdot m_{\text{ads}}} \quad (12)$$

where,  $Q$  [mL/min] is the flow rate of adsorbate solution,  $C_i$  [mg/L] is the initial adsorbate concentration,  $C_t$  [mg/L] is the final adsorbate concentration at time  $t$ . Also, depending on the value of “ $t$ ” the amount of adsorbate onto solid phase at any length of operating time can

be calculated. Accordingly, removal efficiency ( $R.E.\%$ ) of the fixed-bed is calculated from equation (13):

$$R.E.\% = \frac{\int_0^t \left(1 - \frac{C_t}{C_i}\right) dt}{t} * 100\% \quad (13)$$

Other column parameters such as total volume of effluent treated ( $V_{\text{eff}}$ ) and concentration of the effluent ( $C_{\text{eff}}$ ) is calculated using equations (14) and (15), respectively.

$$V_{\text{eff}} = Q * t \quad (14)$$

$$C_{\text{eff}} = \frac{M_{\text{tot}} - q_e * m_{\text{ads}}}{V_{\text{eff}}} * 1000 \quad (15)$$

where,  $M_{\text{tot}}$  is the total amount of adsorbate [mg] present in the total volume of solution that flowed through the column during its at time “t” and it is calculated using equation (16).

$$M_{\text{tot}} = \frac{C_i * Q * t}{1000} \quad (16)$$

Apart from these column parameters, breakthrough curves are fitted with adsorption kinetic models to describe adsorption behavior and for upscaling purpose. Here in this study, Bohart-Adams and fractal-like Bohart-Adams model were fitted to breakthrough curves.

### 2.3.1 Bohart-Adams model

Bohart-Adams model was first proposed by Bohart and Adam, in 1920, to describe the adsorption of chlorine onto activated charcoal (Bohart et al., 1920). According to this model, the equilibrium is not established instantaneously and the adsorption rate is proportional to the liquid-phase adsorbate concentration and the remaining adsorption capacity (Hu et al., 2019). Nowadays, a simplified Bohart-Adams model is used which is given by equation (17) (Bohart et al., 1920):

$$\frac{C_t}{C_i} = \frac{1}{1 + \exp\left(K_{BA} * C_i * \left(\frac{N_0 * Z}{u * C_i} - t\right)\right)} \quad (17)$$

where,  $C_t$  [mg/L] is the effluent concentration at time “t” min,  $C_i$  [mg/L] is the influent concentration,  $K_{BA}$  [L/mg/min] is Bohart Adam rate constant,  $t$  [min] is operating time,  $N_0$  [mg/L] is the bed capacity,  $Z$  [cm] is the bed height, and  $u$  [cm/min] is the superficial velocity.

Also, when the volumetric flow rate of solution,  $Q$  [mL/min], and the inner cross-sectional area of the fixed bed,  $A$  [cm<sup>2</sup>], are known the superficial velocity ( $u$ ) can be calculated with equation (18).

$$u = Q/A \quad (18)$$

### 2.3.2 Fractal-like Bohart-Adams model

Bohart-Adams model has limited performance when it came to asymmetrical breakthrough curves (without the characteristic S-shape) (Chu, 2020) which could happen when adsorption rate drops more rapidly as operation time progresses. The main reason for such drop in adsorption rate could be because (1) the rate determining step is intraparticle diffusion; (2) adsorbent is heterogenous where its components have different activity; and (e) interference from coexisting ions (Hu et al., 2020). Therefore, Hu *et al.* (2019) proposed a fractal-like Bohart-Adams model for practical application and heterogenous adsorption system which is shown in equation (19):

$$\frac{C_t}{C_i} = \frac{1}{1 + \exp\left(K_{BA0} * C_i * t^{-h} \left(\frac{N_0 * Z}{u * C_i} - t\right)\right)} \quad (19)$$

where,  $K_{BA0}$  [L mg<sup>-1</sup> min<sup>-(1-h)</sup>] and  $h$  are the fractal-like Bohart-Adams rate constant and the homogeneity factor, respectively. The value of  $h$  is between 0 and 1 and reflected degree of homogeneity. When  $h = 0$ , the adsorption system is homogenous, and the equation (19) reduces to the simplified Bohart-Adams model (equation 17) whereas, when  $h$  becomes close

to 1, adsorption system is heterogenous and the breakthrough curve is asymmetrical (Hu et al., 2020).

## 2.4 Modified biochar

The word biochar is formed of “bio” and “char”, which means charcoal derived from biomass (Ok et al., 2018). The International Biochar Initiative (IBI) has defined biochar as,

*“Biochar is a solid material obtained from the carbonisation thermochemical conversion of biomass in an oxygen limited environment.”* (IBI, 2018)

For the preparation of biochar, a widely applied thermochemical conversion process is pyrolysis, where pyrolysis temperatures can be 200-900 °C (Gurav et al., 2020; Keerthanan et al., 2020). Apart from biochar, the pyrolysis of biomass also yields secondary valuable product such as bio-oil and syngas. The main purpose of biochar was for soil amendment, but recently many applications of biochar are being explored, such as carbon capture and sequestration, global warming mitigation, energy storage, catalyst material, electrode material and water treatment (IBI, 2018; Dai et al., 2019; Singh et al., 2021). Biochar is a porous material and has many types of surface functional groups which can interact with pollutant molecules due to which it has received much attention from researchers for adsorption of emerging contaminants from water (Ok et al., 2018; Cheng et al., 2021).

Pristine biochar, however, has limited adsorption performance compared to activated carbon (Cheng et al., 2021; Singh et al., 2021). So, researchers have used different modification and engineering approaches to enhanced biochar adsorption capacity, affinity, and selectivity. The properties of modified biochar depend upon the origin of biomass, pyrolysis conditions and the modification method (Kwon et al., 2020; Krasucka et al., 2021).

### 2.4.1 Microalgae as precursor for biochar

The reason to select microalgal biomass as a precursor for biochar is because microalgae is a sustainable and renewable biomass. Microalgae have high photosynthetic capacity, tolerate high concentration of carbon dioxide and better in the conversion of photons to biomass than

higher plants. They have a fast growth rate (doubling rate < 1 day) and short life cycle (Sharma et al., 2021; Singh et al., 2021). Thus, microalgae are potentially better than higher plants for bio fixation of carbon dioxide and biomass yield. Further, nutrient-rich wastewater can be used for the cultivation of microalgae (Goswami et al., 2021) and wastewater treatment with microalgae can be intensified using photobioreactors with additional supply of carbon dioxide to achieve high removal rate for nutrients (Sharma et al., 2021). Depending on the technique, the harvested microalgae can be used to produce different valorized products such as animal feed, organoleptic additives, nutraceuticals, biofertilizers, biofuels, biochar, bio-oil, and syngas (Levasseur et al., 2020; Sharma et al., 2021). Integration of microalgal biorefineries with wastewater treatment can provide multitude of benefits regarding (1) wastewater remediation (2) nutrient recovery (3) valorization of waste material and (4) carbon sequestration (Goswami et al., 2021; Sharma et al., 2021). Thus, microalgal cultivation could promote circular bioeconomy and provide economic incentive to treat wastewater, especially in low-income countries, which can lead to overall lower pollution of environmental water. However, the concerns for emerging contaminants remain. In this regard, the microalgal biochar has gained attention as a low-cost and environmentally friendly adsorbent which can adsorb variety of inorganic and organic pollutants (Law et al., 2021).

Microalgal biochar is a product of pyrolysis of microalgal biomass (Yu et al., 2017). The physicochemical properties of adsorbent and adsorbate are important and affects performance for an adsorption process. Also, the feed stock composition and characteristics affect the physicochemical properties of biochar such as, specific surface area, surface functional groups, and particle size (Kwon et al., 2020). Microalgal biochar is characterised with a lower specific surface area than lignocellulosic biomass but has richer oxygen-containing and nitrogen-containing functional groups that can interact with organic pollutants, such as pharmaceuticals (Binda et al., 2020; Kwon et al., 2020). Furthermore, microalgal biochar has lower carbon content and contains different mineral elements such as Na, K, Ca, Mg and P as ash layer (Law et al., 2021). Binda et al. (2020) did a comparative study of biochar prepared from freshwater microalgal biomass (*Chlorella vulgaris* and *Spirulina sp.*), marine water microalgal biomass (*Nannochloropsis sp.*) and, walnut shells. The pyrolysis was done at a temperature of 350 °C with 1 h residence time in a nitrogen atmosphere. Microalgal biochar had nitrogen and phosphorus content along with



abundant oxygen-containing functional groups and produced a higher bio-oil yield than the walnut shell. Also, marine water microalgal biochar was richer in mineral or ash content and displayed a rough surface, whereas freshwater microalgae had lower ash content and a smoother surface.

#### 2.4.2 Effect of pyrolysis condition

Biochar can be obtained from different types of thermochemical processes, such as slow pyrolysis or conventional pyrolysis, fast pyrolysis, gasification, microwave-assisted pyrolysis and hydrothermal carbonization (Yu et al., 2017; Ok et al., 2018). However, biochar production from slow pyrolysis is considered the best process because it provides a high yield for biochar (Yu et al., 2017). The schematic of a tube furnace used to make biochar via slow pyrolysis is shown in Figure 3.

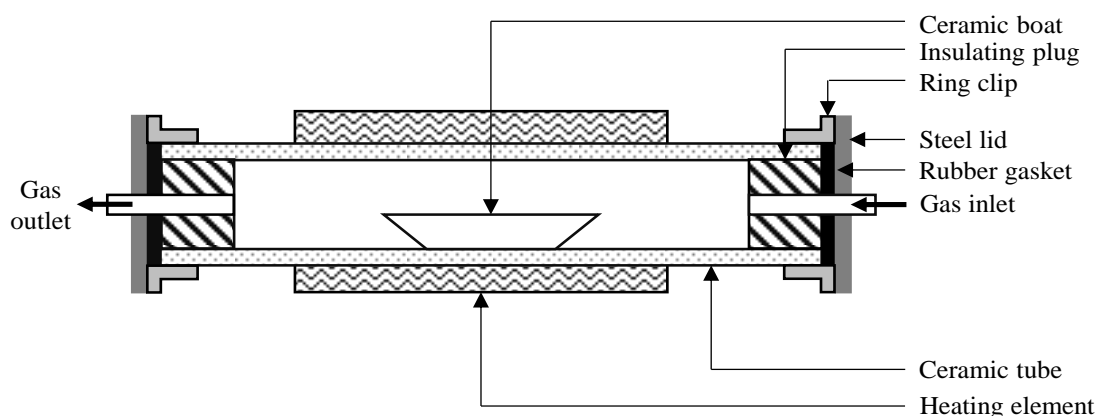


Figure 3. Schematic of the tubular furnace used for preparation of biochar.

As shown in Figure 3, the tubular furnace consists of a long ceramic tube placed inside a tubular heating element. The feedstock is placed in the ceramic boat and loaded into the furnace. Then, a marked rod is used to ensure that the feedstock is in the middle of the tube. Before the operation, both ends of the tube are fitted with insulating plugs to prevent heat loss. Also, to ensure the system is airtight, rubber gaskets and steel lids are used. Then, a shielding gas is passed through the tube via the gas inlet to maintain an oxygen-limited environment. During operation, the formed syngas and vapours are evacuated by the constant outflow of the shielding gas. The operating parameters for the pyrolysis using the tube furnace are the pyrolysis temperature, heating rate, residence time, and shielding gas

flow rate. Generally, in a slow pyrolysis process, heating rate is less than 10 °C/min, pyrolysis temperature is between 300-800 °C and residence time is more than or equal to 1 h (Bach et al., 2017; Ok et al., 2018).

The operating parameters affects yield as well as physicochemical properties of biochar. A key parameter that affect the biochar yield and characteristics is the pyrolysis temperature (Krasucka et al., 2021). Increasing pyrolysis temperature generally decreases biochar yield (Krasucka et al., 2021). Özçimen and Ersoy-Meriçboyu (2008) conducted statistical analysis to study the effect of pyrolysis conditions such as pyrolysis temperature, shielding gas flow rate and heating rate on the yield of char. It was observed that at a constant residence time, the biochar yield decreased significantly with increasing temperature followed by shielding gas flow rate, and heating rate. The optimal condition for maximum biochar yield was at pyrolysis temperature 450 °C and heating rate 5 °C/min under stable nitrogen atmosphere (Özçimen et al., 2008). Depending on pyrolysis temperature, there are three stages of mass loss during pyrolysis of microalgae (Binda et al., 2020). Up to 200 °C mass is lost due to loss of moisture content. Then, between 200-600 °C, mass is lost due to the active decomposition of organic matter (carbohydrates, proteins and lipids) to produce different pyrolysis products such as syngas, bio-oil and bio-char (Bach et al., 2017). Finally, above 600 °C mass is lost due to release of carbon dioxide, carbon monoxide and other volatiles, until a stable final mass is obtained which contains fixed carbon and ash (or minerals) (Binda et al., 2020; Singh et al., 2021).

Generally, increasing pyrolysis temperature increases specific surface area and porosity of biochar (Krasucka et al., 2021; Singh et al., 2021). Bordoloi *et al.* (2016) performed slow pyrolysis of microalgae *Scenedesmus dimorphus* to evaluate characteristics of bio-oil and other pyrolysis products at 300, 400, 500 and 600 °C. They found that increasing pyrolysis temperature till 500 °C increased specific surface area (from 1.72 m<sup>2</sup>/g to 123 m<sup>2</sup>/g). However, when pyrolysis temperature was further increased (till 600 °C) the specific surface area decreased to 89 m<sup>2</sup>/g. This decline in the specific surface area of the biochar at high temperatures was due to the melting of ash layers at high temperatures which filled up the pores. Therefore, the increasing temperature might not always be beneficial when producing porous biochar (Bordoloi et al., 2016).

Pyrolysis temperature also affects graphitization degree, surface functional groups, polarity, fixed carbon content, ash content, pH, and stability of biochar (Krasucka et al., 2021). H/C molar ratio of biochar is often used to estimate the number of hydrogen bonded to each carbon atom and indicates the graphitization degree or aromaticity of biochar (Ronsse et al., 2013). Also, the H/C molar ratio is inversely related to the fixed carbon content. Hence, lower H/C ratio can be associated to higher recalcitrance or stability of biochar (Ronsse et al., 2013). Ronsse *et al.* (2013) conducted experiments to determine the effects of biomass, pyrolysis temperature and residence time on biochar characteristics. Feedstock for pyrolysis was pinewood, green waste, wheat straw and dried algae. It was observed that increasing pyrolysis temperature increased its fixed carbon content, aromaticity, ash content. Also, the biochar's ash content is directly related to its pH (Ronsse et al., 2013).

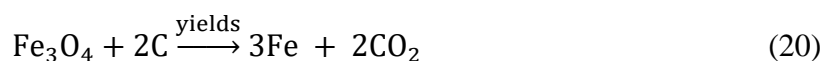
On the other hand, O/C and (O+N)/C molar ratios help approximate the abundance of oxygen-containing functional groups (for example, carboxyl, phenolic, and lactone) on the biochar's surface and the polarity of biochar (Krasucka et al., 2021). Presence of oxygen containing functional groups on biochar makes it polar and hydrophilic and affect pH of biochar. Increasing pyrolysis temperature enriches carbon and mineral content in biochar and oxygen, hydrogen and nitrogen content are volatilized through decarboxylation, dehydration, demethylation, and deamination reactions (Leng et al., 2019; Liu et al., 2021). Thus, at high temperature (700-800 °C), biochar is more graphitic, less polar, hydrophobic, and alkaline. For example: Patel *et al.* (2021) synthesized biochar from banana peel by slow pyrolysis at 450, 550, 650 and 750 °C. Similar to the findings of Ronsse et al. (2013), it was observed that increasing temperature increased carbon content, ash content, and alkalinity. In addition, it also decreased oxygen, hydrogen, and nitrogen percentage while specific surface area and pore volumes increased (Patel et al., 2021). Overall, pyrolysis at high temperature generated porous, alkaline, and carbonaceous residue.

### 2.4.3 Synthesis of iron modified biochar/ Fe-biochar composites.

As mentioned earlier, pristine biochar has limited adsorption potential and are often modified to enhance its adsorption performance. The metal salt/metal oxide modification is one of the widely used modification routes followed by acid-base modification and ball milling (Cheng et al., 2021). Previously applied methods of production of Fe modified biochar are carbothermal reduction, ball milling, hydrothermal carbonisation, and coprecipitation (Li et al., 2021b).

Impregnation and pyrolysis methods are simple where biomass is pre-impregnated with iron salts and subsequently pyrolyzed to make Fe modified biochar. The ball milling method produces Fe biochar composites via ball milling pristine biochar and desired iron species ( $\text{Fe}^0$ ,  $\text{Fe}_2\text{O}_3$  or  $\text{Fe}_3\text{O}_4$ ) together. In hydrothermal carbonisation, wet biomass is pyrolyzed at low temperatures (180-260 °C) and high-pressure conditions to make biochar (Ok et al., 2018). Under the precipitation method, there are two ways of biochar synthesis: (1) magnetic nanoparticles are coprecipitated from ferrous and ferric salts in alkaline condition into the biochar matrix and (2) zero valent iron (ZVI) is precipitated into the biochar matrix via reduction of iron salts a strong reductant such as  $\text{NaBH}_4$  (Li et al., 2021b). Precipitation methods are known to have problems with the agglomeration of nanoparticles and blockage of pores resulting in poor performance (Li et al., 2021b). The ball milling process is simple and efficient but has limited applicability because it can make non-homogenous product and is energy intensive for large scale production (Kumar et al., 2020).

The amount of iron salt and pyrolysis conditions determine the characteristics of biochar and type of iron species in the biochar. Hoch et al (2008) synthesized carbon supported nanoscale ZVI through pyrolysis of carbon black with iron salts (iron nitrate, iron acetate, iron oxalate, and iron citrate). The pyrolysis temperature was changed from 200 °C to 800 °C with 100 °C increment. At lower temperatures (300-500 °C) iron salts degraded to form magnetite ( $\text{Fe}_3\text{O}_4$ ). As the temperature was increased from 500 °C to 600 °C, magnetite was replaced by ZVI. At higher temperature (>600 °C) crystalline iron was formed. The study also suggested that carbothermal reduction reaction of iron was responsible for the formation of ZVI, which is shown by equation 20 (Hoch et al., 2008):



Luo *et al.* (2019) prepared magnetic biocarbon by pyrolysis of iron-rich microorganism, *Phanerochaete chrysosporium*, which is a type of white rot fungi. The fungus was cultivated in presence of ammonium ferro citrate, and the iron-rich fungi was harvested to acquire iron containing biomass. The iron-containing fungal biomass was pyrolyzed at 400 °C to obtain iron containing carbonaceous residue. Subsequently, the residue was treated with KOH and re-pyrolyzed at 700 °C with 2 h residence time which yielded porous biocarbon with very high specific surface area (1986 m<sup>2</sup>/g). The iron contained in the biocarbon was at zero valent state (Fe<sup>0</sup>). The material was used for adsorption of diclofenac and showed a high adsorption capacity (up to 361.25 mg/g).

Min *et al.* (2020) produced FeCl<sub>3</sub> impregnated biochar via one-step synthesis and used it for the removal of nitrate and phosphate from water. Dried and crushed cornstalk samples were impregnated with different concentrations (1%, 5% and 10%) of FeCl<sub>3</sub> solution and subsequently pyrolyzed at 550 °C to obtain Fe-loaded biochar. The increase in iron content during impregnation resulted in decrease in porosity and surface area, due to blocking of pores by excess iron oxides. The study showed an important effect of the adsorbate nature and adsorbent parameters on the adsorption performance. The nitrate favourably adsorbed by biochar with lower iron content whereas phosphate had high binding potential with ferric ions and was better removed when iron content was higher.

Zhao *et al.* (2020) produced Fe<sup>0</sup>/Fe<sub>3</sub>C/C composite and used it for adsorption and degradation of oxytetracycline and chloramphenicol and compared it with zero valent iron and biochar. Corn straw biochar was impregnated with ferric nitrate and thermally treated up to 800 °C for 2 h in nitrogen atmosphere to obtain Fe<sub>3</sub>C loaded biochar. The material produced had better performance for the removal of oxytetracycline and chloramphenicol than zerovalent iron and biochar. The pharmaceuticals were removed through adsorption and degradation. The Fe<sup>0</sup>/Fe<sub>3</sub>C/C composite contained core-shell structures with iron core surrounded by graphitic carbon shell. The graphitic carbon shell allowed free passage of electrons for redox reactions while preserving of iron core from passivation and from leaching. In case of ZVI, passive layer of iron oxide was formed which inhibited its performance and showed significant leaching. Also, in their previous study, XRD analysis

was performed for similar composite and zerovalent iron at different pH (Zhao et al., 2019). It was found that zero valent iron dissolved in acidic conditions (pH 2-4) and formed passive hydroxide layer in alkaline conditions (pH 14). But the composite was stable in both acidic and alkaline conditions.

Liu *et al.* (2021) produced Zn/Fe-modified biochar via impregnation method. The powdered corn stalk was impregnated with either  $\text{ZnCl}_2$  or  $\text{FeCl}_3$  solution. The impregnated feedstock was pyrolyzed at different temperatures (400, 600, and 800 °C) with 4-h residence time and nitrogen flow rate 100 mL/min. Subsequently, the biochar was washed with HCl and deionized water. The presence of Fe altered pyrolysis route. For biochar produced at 400 °C, Fe reduced aromatization but increased decarboxylation. Then, at 800 °C, Fe inhibited dehydration and caused enrichment of carbon. It was suggested that formation of iron carbide ( $\text{Fe}_3\text{C}$ ) could cause enrichment of carbon. Also, at 800 °C, the presence of iron increased surface defects in biochar which increased its specific surface area ( $356 \text{ m}^2/\text{g}$ ) compared to unmodified biochar ( $231 \text{ m}^2/\text{g}$ ) (Liu et al., 2021). Additionally, at all the studied pyrolysis temperature,  $\text{FeCl}_3$  modified biochar had higher adsorption performance for nitrobenzene compared to the pristine biochar.

Presence of iron in biomass also affects the distribution of pyrolysis products. Xia et al. (2019) synthesized Fe-containing biochar by impregnating demineralized Chinese chest nut with  $\text{Fe}(\text{NO}_3)_3$  and subsequently pyrolyzing it at varying pyrolysis temperature under 200 mL/min  $\text{N}_2$  flow for 30 minutes. It was observed that presence of iron in biomass increased gas and solid yield but decreased the liquid yield compared to pyrolysis of biomass without iron. Additionally, increasing temperature decreased solid yield and liquid yield while it increased the gas yield. On the other hand, presence of iron and increase in temperature had combined role in activation of biochar. At low temperatures (400-600 °C), redox reaction between carbon matrix and iron caused formation of micropores. At higher temperature (600 °C) iron oxides reacted with carbon to form mesoporous biochar containing iron carbide and zero-valent iron. At temperature of 700-800 °C, iron carbide continues to react with carbon matrix to form graphitic mesoporous char (Xia et al., 2019).

Wurzer and Mašek (2021) pyrolyzed mixture of iron rich waste (ochre) and lignocellulosic biomass (soft wood pellets and wheat straw pellets) at 550 °C, under 800 mL/min N<sub>2</sub> flow for 45 mins. Subsequently, physical activation was conducted by increasing the temperature to 800 °C under 550 mL/min CO<sub>2</sub> flow with residence time 60 mins. It was observed that pyrolysis of mixture of ochre and lignocellulosic biomass increased gas yield which could be combusted for lowering energy demands of the pyrolysis process. Moreover, the physical activation with CO<sub>2</sub> impeded formation of zero-valent iron and rather formed magnetite and maghemite in the biochar. The physically activated biochar was used for the removal of caffeine and fluconazole from water and it showed superior adsorption performance than pristine biochar.

### 3 General aims and objectives

The presence of iron and pyrolysis temperature were found to be key variables that affect physicochemical properties of biochar. However, modification of microalgal biomass with iron has not been reported before. So, the main aim of this thesis is to study the adsorption of diclofenac and ciprofloxacin onto Fe modified biochar. The conceptual framework of this thesis is given by Figure 4.

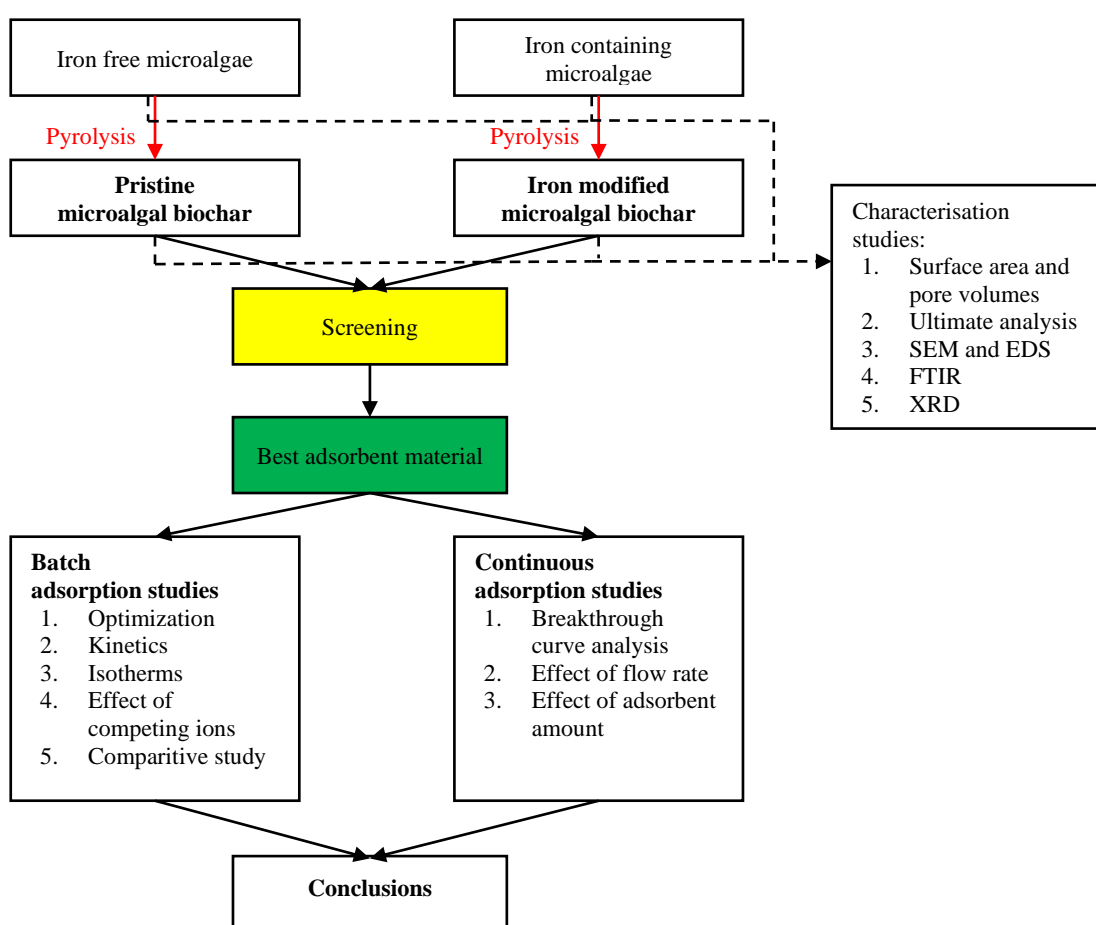


Figure 4 Conceptual Framework for adsorption studies using microalgal biochar.

The adsorption performance of biochar is dependent upon its intrinsic properties as well as experimental conditions. Therefore, prior to adsorption experiments, screening tests were performed where different microalgal biochar were prepared via different routes and the best biochar was selected based on their adsorption performance. During preliminary experiments (results not shown), unwashed biochar showed some adsorption capacity



therefore effect of washing was also investigated during screening tests. After the screening tests, batch studies were performed to study the effect of different variables on the adsorption performance of the biochar and to compare the adsorption performance with a commercial activated carbon. The continuous adsorption studies were performed to understand the kinetics and bed capacities of synthesized biochar by varying working conditions.

The specific objectives of this work are as follows:

1. To synthesize biochar from microalgae, harvested with  $\text{FeCl}_3$  and centrifugation.
2. To perform screening tests for determination of optimum pyrolysis temperature and washing requirement during synthesis of biochar for maximum adsorption performance.
3. To perform batch tests for the optimization of operating parameters such as contact time, initial concentration of pharmaceutical and adsorbent dosage for adsorption.
4. To study the effect of iron on properties of biochar such as specific surface area, pore volumes, elemental composition, and functional groups.
5. To study the effect of competing ions on adsorption efficiency of pharmaceuticals.
6. To understand adsorption mechanism through batch adsorption isotherm and kinetics studies.
7. To compare the adsorption capacities of synthesized biochar with commercial activated carbon.
8. To evaluate applicability of the best adsorbent material in fixed-beds through continuous adsorption studies.

## 4 Methodology

This section describes all the experimental procedures applied in this study. First, this chapter explains prerequisites before adsorption performance tests such as materials/chemicals required and preparation of biochar, solutions, and standard curves. Then, it describes batch studies and column studies which helped to evaluate the adsorption performance of biochar. The batch adsorption tests consist of five stages: screening tests, interactions study, adsorption kinetic study, adsorption isotherm study and study for the effect of competing ions. Screening tests helped to select the best biochar preparation conditions and optimizing batch adsorption parameters. After that, adsorption kinetic study and isotherm study helped to estimate the speed of adsorption and adsorption capacity, respectively. The column adsorption studies helped to determine the adsorption performance of biochar when used in an adsorption column. Finally, this section describes the applied characterization studies which helped to determine the adsorbent properties such as specific surface area, pore volumes, morphologies, and surface chemistry of samples.

### 4.1 Materials and chemicals

Diclofenac sodium (reagent grade), ciprofloxacin hydrochloride (secondary standard grade) and commercial granulated activated carbon (C-AC, product number: 242268) were obtained from Sigma Aldrich. Dried microalgae, *Scenedesmus quadricauda* was acquired from a previous microalgal experiment (Daneshvar et al., 2020). The culture of freshwater microalga, *S. quadricauda* was purchased from Culture Collection of Algae and Protozoa (Scotland, UK) and cultivated in dairy wastewater under continuous light, for 12 days (Daneshvar et al., 2020). Then, the microalgae harvested by centrifugation was named as MA and the microalgae harvested by  $\text{FeCl}_3$  coagulation was named as Fe-MA. For coagulation, microalgae were harvested with 400 mg/L  $\text{FeCl}_3$  coagulant dosage, pH 7.5, and contact time was 15 min. After harvesting, the microalgae were dried and stored.

## 4.2 Biochar preparation

All the types of biochar used in this study were prepared with Carbolite™ tube furnace. For all the biochar preparation, 1.5 g dry feedstock was weighed and pyrolyzed at a desired temperature with 1 h residence time of, 5 °C/ min heating rate of and 0.2 L/min sweeping gas (N<sub>2</sub>) flow rate. After the pyrolysis, the solid residue or biochar was left to cool at room temperature, under the flow of N<sub>2</sub> gas. Biochar was then washed after pyrolysis unless stated otherwise. The washing was done in 50 mL centrifuge tubes. Biochar samples (180 mg) was poured into different centrifuge tubes and filled with DI water till 50 mL mark. The tubes were then closed and agitated at 270 rpm for 20 min. After that it was centrifuged at 4000 rpm and supernatant was collected to measure the pH. The precipitate was washed multiple times until the pH of the supernatant was stable. Finally, the precipitate was dried overnight in an oven at 100 °C and stored before use.

## 4.3 Preparation of solutions and standard curves

Before experiments, required volumes of adsorbate solutions were prepared. Generally, required amount (mg) of selected pharmaceutical was weighed and mixed with de-ionized (DI) water in 300 mL beaker for a few minutes to ensure complete mixing. The solution was then transferred to a volumetric flask of required volume and DI water was filled to the volume mark. The flask was shaken for few minutes and the solutions were stored in dark brown bottles until required.

Before preparing the standard curve, UV-vis (Ultraviolet – visible light) absorbance values for 10 mg/L ciprofloxacin and diclofenac were determined by scanning the respective pharmaceutical solution with electromagnetic wave from wavelength 200 nm to 800 nm. The peak absorption wavelengths for ciprofloxacin and diclofenac were found to be 273 nm and 276 nm, respectively. Then, serial dilutions of pharmaceutical solutions were prepared at determined concentrations. After that, absorbance for each solution was measured at their maximum absorbance wavelength ( $\lambda_m$ ). Representative concentrations were plotted against their respective absorbance values and the linear section of the plot was fitted with a straight line which is known as standard curve. The fitted curve equation was then used to determine concentration of unknown solutions based on their absorbance values.

#### 4.4 Batch tests

The five stages in batch tests are screening tests, optimization, adsorption kinetic study, adsorption isotherm study and study for the effect of competing ions. General steps taken for all the batch tests in this study are as follows:

1. A known amount of biochar ( $m_{ads}$ ) was weighed and added into a polypropylene tube (15 mL).
2. A desired volume of adsorbate solution was added ( $V$ ) to the tubes.
3. Then, the tube was closed and shaken at 150 rpm during pre-determined time ( $t$ ).
4. After shaking, the slurry was filtered using a 0.45  $\mu\text{m}$  syringe filter. For each test tube a separate syringe and syringe filter was used to avoid inaccuracies due to mixing of results.
5. The concentration of adsorbate in filtrates was measured by a UV-Vis spectrophotometer (Model: Cary 5000 UV-Vis-NIR, Agilent Technologies).
6. The initial and final mass concentrations (mg/L) of adsorbates were calculated using the standard curve equation.
7. Adsorption capacities and removal efficiencies were determined using equation 1 and 2, respectively.

During the shaking, it was ensured that slurry of biochar and adsorbate solution was well mixed by periodic monitoring. All the experiments were conducted at the room temperature, natural initial pH (5-6) and in triplicates, unless stated otherwise.

#### 4.4.1 Screening tests

Screening tests were initially conducted to compare the adsorption performance of different synthesized biochar samples to select the best biochar sample. The biochar samples and their names, based on preparation conditions, are provided in the screening test design presented in Figure 5.

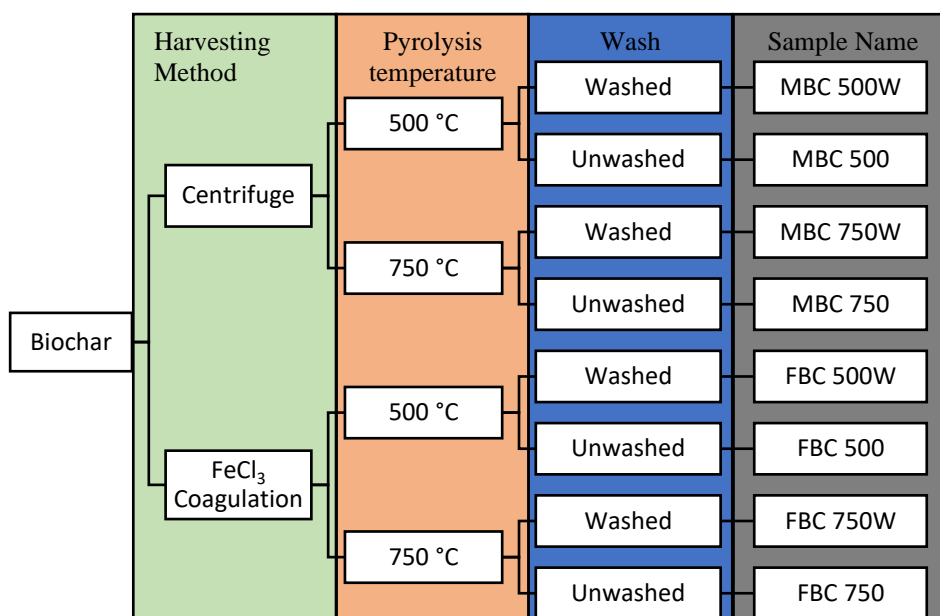


Figure 5. The scheme of screening test.

From Figure 5, altogether eight biochar samples were prepared for diclofenac and ciprofloxacin adsorption experiments. The microalgae harvested with only centrifugation provided pristine biochar whereas microalgae harvested with FeCl<sub>3</sub> coagulation method provided Fe-modified biochar. Then, pyrolysis temperature was set to either 500 or 750 °C for each microalgal feedstock. After pyrolysis, each biochar was then grouped into two subgroups. One was washed for several times with de-ionized water till the pH of wash water was stable, while other was not washed and used as such. Screening was done separately for each pharmaceutical by batch procedure with  $C_i = 10$  mg/L,  $V = 10$  mL, and  $t = 180$  min.

#### 4.4.2 Optimization study

Prior to further batch studies, operating parameters such as adsorbate concentration, adsorbent dosage and contact time were optimized in the optimization studies. The optimal values were determined based on the maximum removal efficiency and adsorption capacity. The different values for each variable are shown in Table 3.

Table 3 Variables used for interaction study and their values.

Variables	Values		
Contact time, $t$ [mins]	20	100	180
Concentration, $C_i$ [mg/L]	10	30	50
Adsorbent dosage [g/L]	0.4	0.7	1

Also, the during the experiments volume of solution ( $V$ ) was 10 mL. The experiments were conducted at room temperature and at natural pH of the solution. A full-factorial design was prepared for the given variables based on their levels. Therefore, for each pharmaceutical, all together twenty-seven tests were performed. Then, MATLAB was used to plot the 3D surfaces between any two variables while keeping the third variable constant. Altogether, 18 plots were prepared to show the removal efficiency and adsorption capacity of each pharmaceutical. This study provided optimal dose, adsorbate concentration and contact time for isotherm and kinetic studies.

#### 4.4.3 Kinetic study

The optimal adsorbent dosage and adsorbate concentration from the optimization tests were 0.7 g/L and 50 mg/L, respectively. Accordingly, batch kinetic experiments were performed with  $m_{\text{ads}} = 7$  mg,  $V = 10$  mL, and  $C_i = 50$  mg/L at varying contact times (maximum contact time was 300 min). Then, the adsorption capacity was plotted against contact time and fitted with non-linear kinetic models (Equation 7, 9, and 10) using the MATLAB curve fitting tool.

#### 4.4.4 Isotherm study

In the isotherm studies, adsorbate concentration was varied while adsorbent dosage and contact time were constant. For this purpose, the batch experiments were performed where,  $t = 180$  min,  $m_{\text{ads}} = 7$  mg,  $V = 10$  mL, and  $C_i = 1$  to 100 mg/L. Then, the adsorption capacity was plotted against the equilibrium adsorbate concentration and fitted with non-linear isotherm models (Equation 3, 4 and 5) using the MATLAB curve fitting tool.

For comparison of different adsorbent, adsorption isotherm experiments were conducted with MBC 750W, FBC 750W and C-AC where,  $t = 180$  min,  $m_{\text{ads}} = 3.5$  mg,  $V = 5$  mL, and  $C_i = 1$  to 100 mg/L. The experimental data was fitted with Langmuir isotherm model to obtain maximum Langmuir adsorption capacities.

#### 4.4.5 Effect of competing ions

In real wastewater, presence of inorganic cations and anions can interfere and compete with adsorption of organic pollutants, significantly affecting adsorption performance (Shirani et al., 2020; Patel et al., 2021). So, effects of different competing ions were studied using NaCl,  $\text{Na}_2\text{CO}_3$ ,  $\text{Na}_2\text{SO}_4$ ,  $\text{NaNO}_3$ , KCl,  $\text{CaCl}_2 \cdot \text{H}_2\text{O}$ , and  $\text{MgCl}_2 \cdot 6\text{H}_2\text{O}$ . Pharmaceutical solutions were spiked with a known amount of salt to make 1 mM and 2 mM salt concentrations. Then, batch adsorption studies were performed with  $C_i = 10$  mg/L,  $V = 10$  mL, and  $m_{\text{ads}} = 7$  mg to check the effect of ions on adsorption performance.

#### 4.5 Continuous adsorption studies

Omnifit<sup>®</sup> labware glass chromatography EZ columns were used for preparing adsorption columns for continuous adsorption studies. A peristaltic pump was used to maintain a constant flow of adsorbate solution through the column. The arrangement of column apparatus is shown in Figure 6.

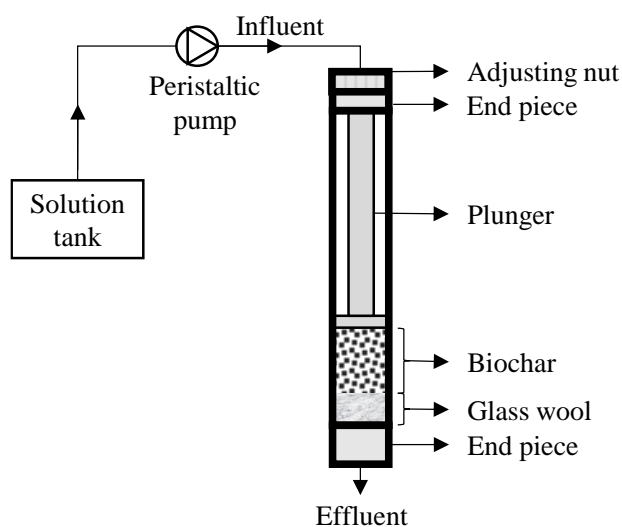


Figure 6. Schematic representation of the apparatus used for fixed-bed adsorption experiments.

Figure 6 shows the schematic arrangement of the column apparatus. First, the glass column was held vertically using a clamp stand and the bottom endpiece was screwed into the column. Then, about 1 mm of glass wool layer was packed inside the column over the bottom end piece to prevent clogging of bottom end frits by biochar. After that, the required amount of FBC 750W ( $m_{ads}$ ) was poured into the column, followed by some DI water to form the adsorbent bed. Then, the top end piece was screwed into the column and the attached plunger was pushed to the level of the adsorbent bed using the adjusting nut. After the setup, the top end piece was connected to a solution tank by a silicon tube. Then, a peristaltic pump was fitted along the silicon tube to maintain a constant flow of solution through the column.

Before the operation, the solution tank was filled with DI water to rinse the adsorbent bed. During the rinsing step, the biochar column became compact, so, the plunger was screwed into the column to fill up the void left behind due to the compaction of biochar. Thus, a fixed bed adsorption column was established, and the bed height ( $Z$ ) was measured using vernier callipers. The volumetric flow rate ( $Q$ ) was adjusted per requirement and verified by measuring the time taken to fill a 5 mL volumetric flask. Then, the solution tank was emptied, and the air was pumped into the column to remove residual DI water.



The column performance for each pharmaceutical was studied at different volumetric flow rates (f1: 1 mL/min and f2: 2 mL/min) and adsorbent amounts (m50 and m100 mg). The experimental runs, name and operating parameters are shown in Table 4.

Table 4. Experimental runs and the operating parameters for fixed bed adsorption study.

Run	Experiment name	$m_{ads}$ [mg]	$Q$ [mL/min]
1	m50_f1	50	1
2	m50_f2	50	2
3	m100_f1	100	1
4	m100_f2	100	2

For each column experiment, the solution tank was filled with an adsorbate solution ( $C_i=10$  mg/L) and the pump was turned on. As the solution moved through the column, the effluent was collected from the bottom of the column at different time intervals, and their concentration was measured using a UV-vis spectrophotometer. Simultaneously, breakthrough curve was plotted. The column operation was stopped when the breakthrough curve reached exhaustion point or when it attained plateau. To evaluate column performance, the bed capacity and removal efficiency of the column were calculated using equation (12) and (13), respectively. Also, breakthrough curve was plotted with MATLAB and fitted with non-linear Bohart-Adams and fractal-like Bohart-Adams model (Equation (17) and (19)) using the MATLAB's inbuilt curve fitting tool. To compare performance of model, its ability to predict bed capacity was compared with experimental bed capacity. However, model bed capacity was expressed as mass of adsorbate per volume of bed or mg/L. The model bed capacities were expressed as mass of adsorbate per mass of adsorbent using equation (21).

$$q_b = N_{0*} \frac{V_b}{m_{ads}} \quad (21)$$

Where,  $V_b$  is the bed volume. The manufacturer of Omnifit<sup>®</sup> column used in this study provided with an equation to calculate bed volume from bed height which is given by equation (22).

$$V_b = 0.3421 * Z \quad (22)$$

#### 4.6 Biochar characterization

Characterisation studies were used to determine physicochemical properties of biochar. Due to large number of samples before screening, only the samples tabulated in Table 5 were characterised.

Table 5. The labels and description of samples used in characterisation studies.

<b>Label</b>	<b>Description</b>
<b>MA</b>	Microalgae harvested with centrifugation
<b>Fe-MA</b>	Microalgae harvested with FeCl <sub>3</sub>
<b>MBC 750W</b>	Washed pristine microalgal biochar pyrolyzed at 750 °C
<b>FBC 750W</b>	Washed Fe-doped microalgal biochar pyrolyzed at 750 °C
<b>FBC 750W+DIC</b>	FBC 750W after adsorption of diclofenac
<b>FBC 750W+CIP</b>	FBC 750W after adsorption of ciprofloxacin

The specific surface area, pore volume and pore characteristics were determined by nitrogen adsorption-desorption experiments using Micromeritics TriStar II plus BET analyser (USA). Before the analysis, microalgal samples were heat treated at 50 °C for 24 h under nitrogen flow whereas biochar samples were heat treated at 200 °C for 24 h under nitrogen flow for outgassing. The analyser provided Brunauer, Emmett and Teller (BET) surface area and pore volumes. Also, t-method was used to determine micropore volume. Finally, adsorption and desorption isotherms of samples were compared with standard adsorption-desorption isotherms provided by IUPAC (Rouquerol et al., 2014a) to determine pore characteristics. Scanning electron microscopy (SEM, JEOL JSM 7900F Schottky FE-SEM) was used to observe surface microstructures and the integrated Energy Dispersive X-ray Spectroscopy (EDS) was used to determine surface elemental distribution. The carbon, hydrogen, and nitrogen content in the microalgae and biochar samples (before adsorption) was determined by ultimate analysis via Leco CHNS628 elemental analyzer. Fourier Transformed Infra-Red (FTIR) spectroscopy was applied to determine surface functional groups. The measurements were conducted between wavenumber 400 to 4000 cm<sup>-1</sup> with an increment rate of 1 cm<sup>-1</sup>. Transmittance peaks were noted and compared with reference database to existing chemical bonds. X-Ray Diffractometer (XRD) was used to determine crystalline phases in biochar with Cu K $\alpha$  radiation a step-size of  $2\theta = 0.02^\circ$ . The peak intensities at different  $2\theta$  were noted and compared with reference database to determine existing crystalline phases.

## 5 Results and Discussions

This chapter presents and discusses the results of adsorbent characterization studies, batch adsorption studies, and fixed-bed column studies. The characterization studies were performed to determine adsorbent properties, and surface characteristics whereas adsorption studies were conducted to understand the adsorption mechanisms, and to evaluate the adsorption performance.

### 5.1 Characterization

The characterization studies were conducted to determine adsorbent properties such as specific surface area, pore volume, surface morphology, elemental composition, surface functional groups and prevalent Fe-species. Also, characterization of adsorbent after adsorption provided changes in the adsorbent properties and clues towards possible adsorption mechanism.

#### 5.1.1 Specific surface area and pore characteristics

Specific surface area and pore volumes of the studied samples were analyzed using a BET analyzer. Table 6 present the BET surface area (sBET) and pore volume of studied samples.

Table 6. Specific surface area and pore volumes of microalgal biomasses and biochar samples.

Sample	sBET [m <sup>2</sup> /g]	Total pore volume [cm <sup>3</sup> /g]	Micropore volume [cm <sup>3</sup> /g]
<b>MA</b>	2.65	0.0129	-
<b>Fe-MA</b>	1.76	0.0076	-
<b>MBC 750W</b>	35.66	0.0622	0.0033
<b>FBC 750W</b>	201.15	0.2563	0.0257
<b>FBC 750W + DIC</b>	162.43	0.2425	0.0113
<b>FBC 750W + CIP</b>	176.79	0.2638	0.0181

According to Table 6, specific surface area of raw feedstocks, MA, and Fe-MA, were much lower than the biochar samples. After pyrolysis, the specific surface area of MA and Fe-MA

increased from 2.65 m<sup>2</sup>/g and 1.76 m<sup>2</sup>/g to 35.66 m<sup>2</sup>/g and 201.15 m<sup>2</sup>/g, respectively. Generally, pristine microalgal biochar has low specific surface area but the specific surface area of MBC 750W is slightly higher than reported in a previous review (Singh et al., 2021). Also, biochar from FeCl<sub>3</sub> coagulated microalgae (FBC 750W) had more than five times specific surface area compared to the pristine microalgal biochar (MBC 750W). The effect of iron on increasing of specific surface area and pore volumes were reported in previous studies (Xia et al., 2019; Liu et al., 2021; Zeng et al., 2021). However, compared to activated carbon, carbon xerogel and carbon nanotubes (Carabineiro et al., 2012) and lignocellulosic biochar prepared at similar temperature (Patel et al., 2021), FBC 750W had lower specific surface area and pore volumes. Moreover, the micropore volumes were only small fraction of total pore volumes (about 5% and 10% for MBC 750W and FBC 750W). Nevertheless, the specific surface area and the micropore volume of FBC 750W decreased after the adsorption of ciprofloxacin and diclofenac which could be due to changes in pore structures or filling up of micropores. Next, the pore characteristics were determined by comparing adsorption and desorption data of N<sub>2</sub> at different relative pressures with the IUPAC recommended standard adsorption-desorption curves. Graphical representations of N<sub>2</sub> adsorption-desorption cycle at different relative pressure using MA, Fe-MA, MBC 750W and FBC 750W is presented in Figure 7 (a-d).

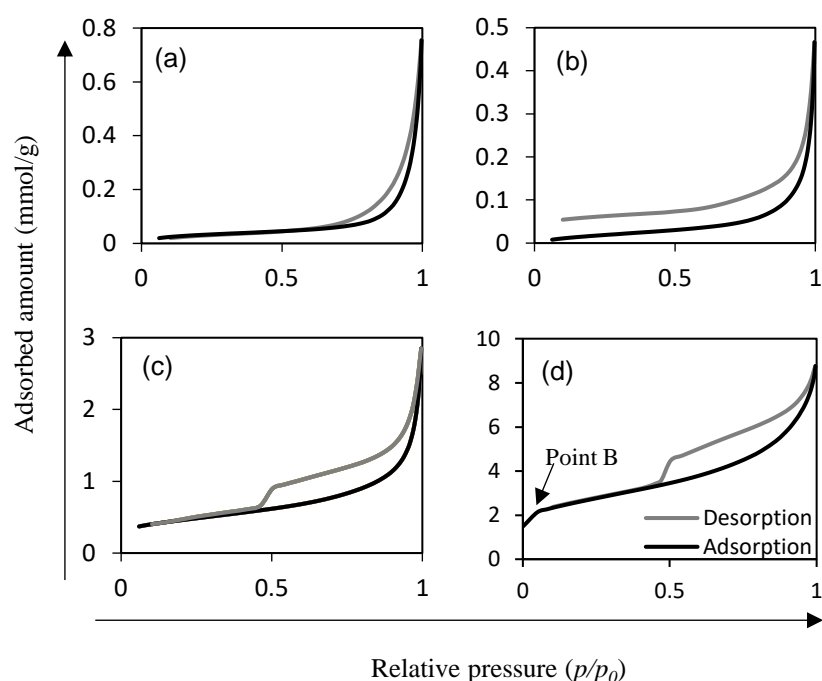


Figure 7. Adsorption-desorption of N<sub>2</sub> at different relative pressures by (a) MA, (b) Fe-MA, (c) MBC 750W, and (d) FBC 750W.

According to Figure 7 (a-b), the samples, MA and Fe-MA, have Type III curves with limited adsorption at low relative pressure and sudden unrestricted multilayer adsorption at high relative pressure (Rouquerol et al., 2014a). These types of curves are displayed by non-porous or macro-porous material that has weak interactivity with the adsorbate. The hysteresis in Figure 7 (a) matches with H1 type hysteresis, which is a narrow loop with nearly vertical and parallel adsorption and desorption branches (Rouquerol et al., 2014b). This type of hysteresis is displayed by agglomerates or compacts of uniformly arranged fairly spherical particles forming narrow pore size distribution (Sing et al., 1985). So, the raw feedstock was a mass of non-porous or macroporous material formed of agglomerated microalgal cells. Then in Figure 7 (b), the hysteresis did not close, and it could be due to swelling of non-rigid porous structures or irreversible adsorption (Sing et al., 1985). Thus, in the case of Fe-MA, the agglomerate structures and pore structures might have been destroyed or deformed during the adsorption and desorption using nitrogen.

Figure 7 (c-d) shows the adsorption-desorption curve for MBC 750W and FBC 750W which is described by Type IIb isotherm (Rouquerol et al., 2014a). This type of isotherm is obtained for non-porous or macro-porous adsorbents. Based on Type IIb isotherm, unrestricted multilayer adsorption takes place which is similar to Type III isotherm. However, unlike the Type III isotherm, the formation of multilayer starts earlier. The curve for FBC 750W (Figure 7 (d)) showed a distinct inflection point (Point B) at low relative pressure which indicated saturation of monolayer and initiation of multilayer adsorption. In the case of both MBC 750W and FBC 750W, H3 hysteresis is observed which is typical for the aggregates of plate-like particles (Rouquerol et al., 2014b) forming slit-shaped pores (Sing et al., 1985).

### 5.1.2 Surface morphology

The scanning electron microscopy showed the surface morphology of raw microalgae and their respective biochar (before and after adsorption). The SEM images of microalgae harvested with centrifugation and  $\text{FeCl}_3$  coagulation-precipitation are depicted in Figure 8 (a-d).

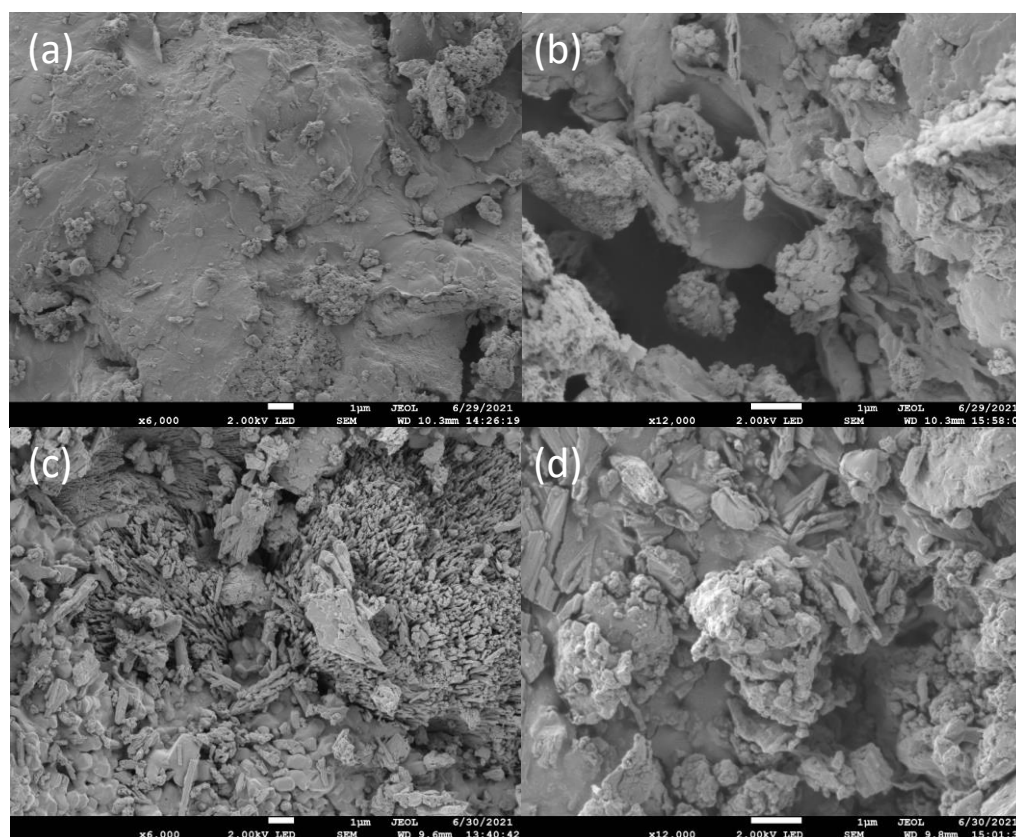


Figure 8. SEM micrographs of MA at magnification (a) 6000 $\times$  and (b) 12000 $\times$ ; and Fe-MA at magnification (c) 6000 $\times$  and (d) 12000 $\times$ .

According to Figure 8 (a), the raw microalgae had smooth surfaces covered with irregular sized particles. The zoomed image of MA (Figure 8 (b)) shows crevices and irregularities present in the raw microalgal surface. Figure 8 (c) shows the surface morphology of Fe-MA which, unlike MA, was covered with crystalline structures. The magnified image of Fe-MA (Figure 8 (d)) shows similar morphology to MA. During coagulation, different multivalent ions from wastewater aid in flocculation (Daneshvar et al., 2020), which could have crystallized during the drying process. Hence, different types of salt crystals are formed over

the surface of Fe-MA. Overall, the SEM images showed that the raw biomasses are aggregates of particles of different sizes.

The micrograph of MBC 750W and FBC 750W are presented Figure 9 (a-d).

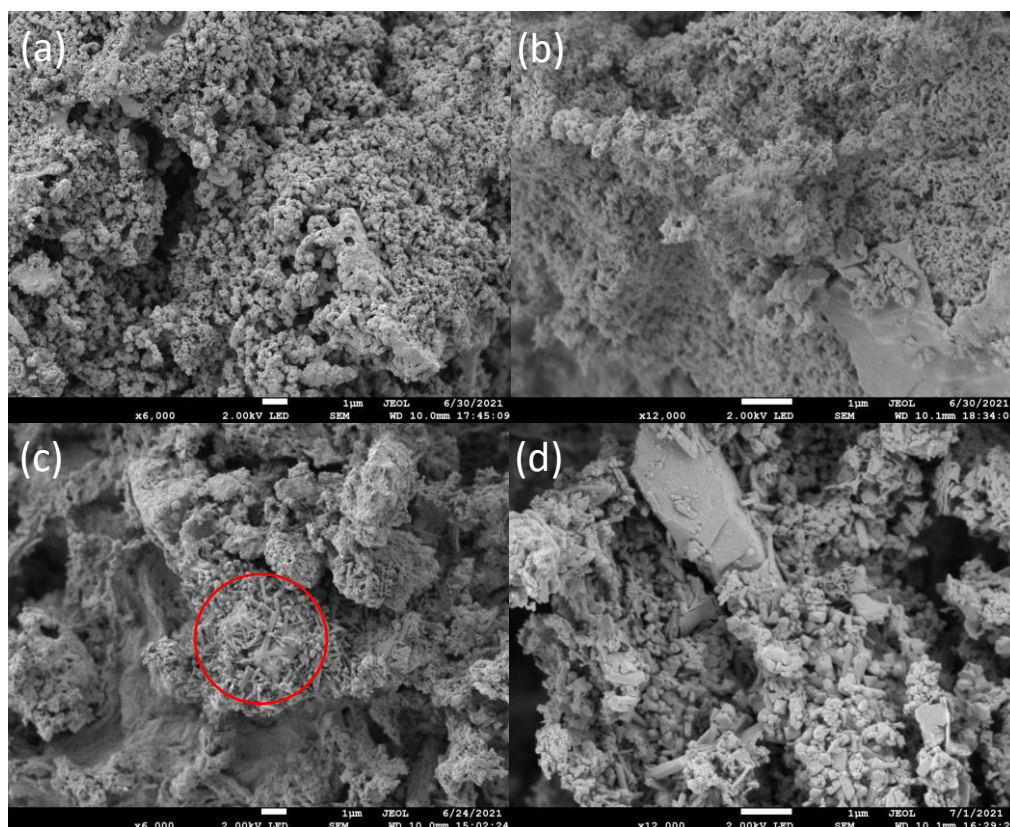


Figure 9. SEM micrographs of MBC 750W at magnification (a) 6000 $\times$  and (b) 12000 $\times$ ; and FBC 750W at magnification (c) 6000 $\times$  and (d) 12000 $\times$

As can be seen from Figure 9 (a-b), the raw microalgal biochar had a highly irregular and spongy texture. On the other hand, the FBC 750W had a highly heterogeneous surface with distinct crystalline and non-crystalline zones. Figure 9 (c) shows a crystalline region (circled in red) on the surface of FBC 750W. The magnified image in Figure 9 (d) shows that small crystalline structures widely covered the biochar surface. The crystalline structures present in FBC 750W could be unwashed remnants during the washing step of biochar preparation.

The micrographs of FBC 750W after adsorption are shown in Figure 10 (a-d).



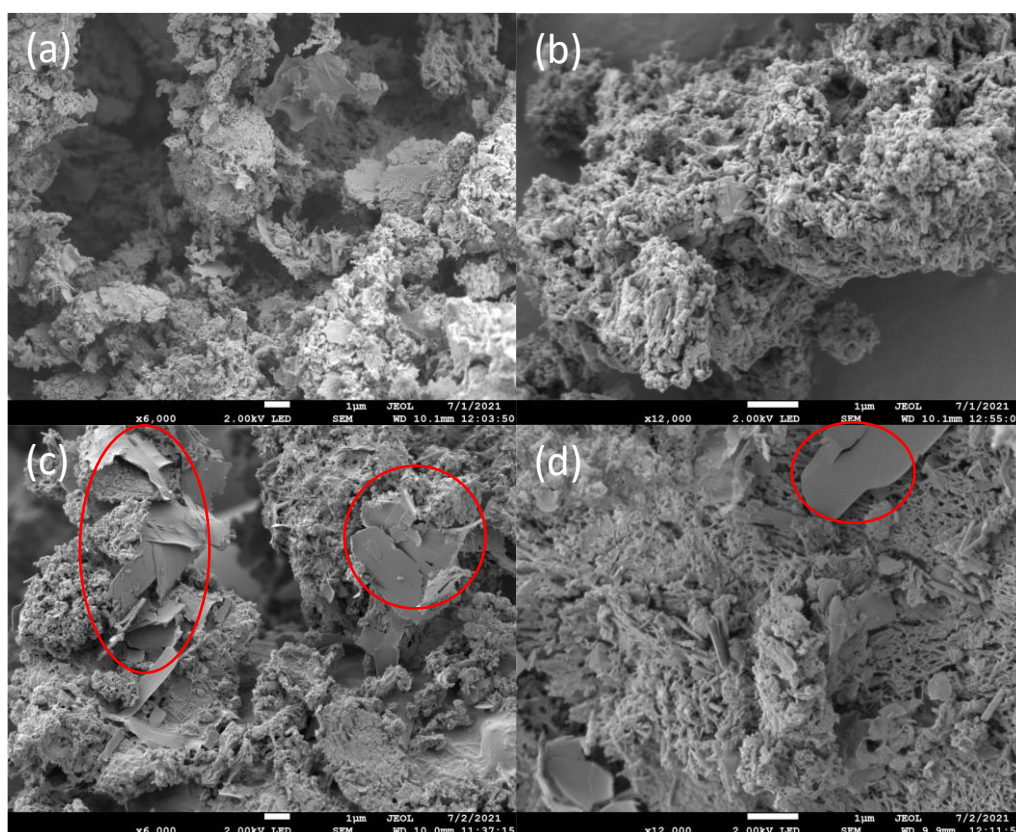


Figure 10. SEM micrographs of FBC 750W after adsorption with diclofenac at magnification (a) 6000 $\times$  and (b) 12000 $\times$ ; and after adsorption with ciprofloxacin at magnification (c) 6000 $\times$  and (d) 12000 $\times$ .

After adsorption with diclofenac or ciprofloxacin, the surface of FBC 750W remained irregular and heterogenous but showed some distinct changes for each case. According to Figure 10 (a), after adsorption with diclofenac, the large crystalline structures had disappeared and only some small rod-like crystals were observed (red circle in Figure 10 (a)) on the biochar surface. Also, Figure 10 (b) shows that well-defined crystalline structures were largely absent. Therefore, crystals might have had dissolved away during the adsorption process. Then, from Figure 10 (c-d), after adsorption with ciprofloxacin, flaky ribbon-like structures (circled in red) had appeared. Nevertheless, small crystalline structures were still well spread over biochar surfaces (Figure 10 (d)).



### 5.1.3 Elemental composition

The ultimate analysis showed the carbon, hydrogen, and nitrogen percentage from studied samples. The results of ultimate analyses and H/C molar ratio are shown in Table 7.

Table 7. Ultimate analysis of microalgal biomass and biochar.

<b>Biochar sample</b>	<b>C%</b>	<b>H%</b>	<b>N%</b>	<b>H/C</b>
<b>MA</b>	33.48	5.31	5.64	1.92
<b>Fe-MA</b>	24.63	3.21	3.59	1.56
<b>MBC 750W</b>	31.71	1.27	3.77	0.48
<b>FBC 750W</b>	28.63	1.48	1.03	0.60

The elemental composition of carbon, hydrogen, and nitrogen content of raw microalgal biomasses, MA and Fe-MA were comparable to that of the literature (Binda et al., 2020). After pyrolysis, the carbon percentage did not change much but the hydrogen and nitrogen content decreased. This is because, during pyrolysis, reactions such as dehydration, demethylation, and deamination release volatiles such as H<sub>2</sub>O, CH<sub>4</sub>, NH<sub>3</sub>, NO<sub>x</sub> (Leng et al., 2019; Liu et al., 2021). The nitrogen content of MBC 750W and FBC 750W can be in form of amines or nitrogen-containing heterocyclic compounds (Ho et al., 2019). The nitrogen content of FBC 750W was lower than that of MBC 750W. So, the presence of iron could have volatilized nitrogenous species.

Both biochar samples, MBC 750W and FBC 750W, have lower H/C molar ratio than their respective biomass which indicates graphitization and recalcitrance, after pyrolysis. However, the H/C molar ratio of biochar synthesized in this study is higher than previously reported in the literature (Ronsse et al., 2013). Additionally, FBC 750W had a higher H/C ratio than MBC 750W indicating lower the graphitization degree. Similar effect of iron during slow pyrolysis of corn straw at 800 °C with residence time 4 h was also reported by Liu et al. (2021). However, in another study (Xia et al., 2019), it was observed that presence of iron salt (FeNO<sub>3</sub>) caused enrichment of carbon with higher graphitization degree. The graphitic carbon can interact via  $\pi$ - $\pi$  electron donor-acceptor interaction with aromatic rings of diclofenac and ciprofloxacin (Shirani et al., 2020; Patel et al., 2021).

EDS results provided distribution of elements on biochar surface. The bar graph of the elemental composition (except C, O and N) is shown in Figure 11.

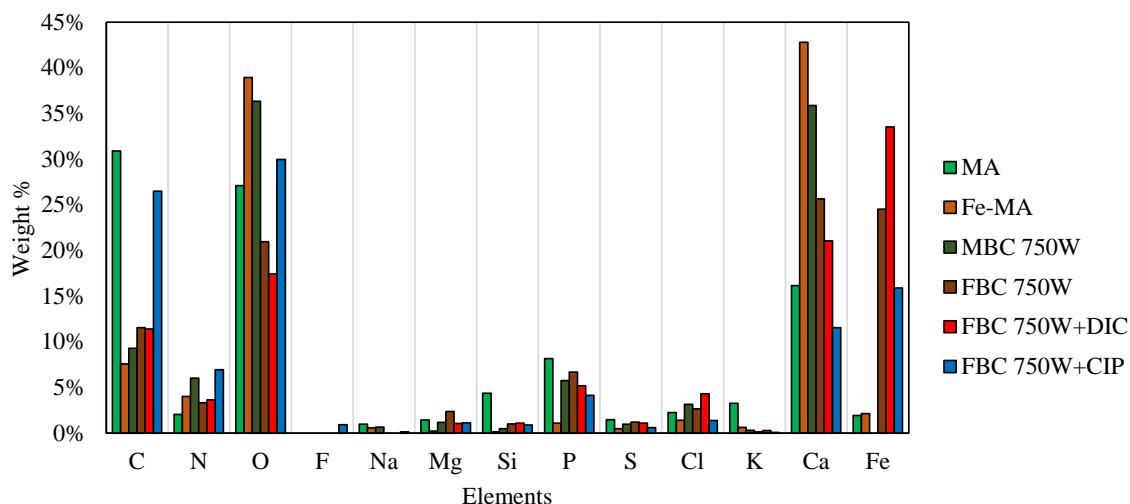


Figure 11. Surface elemental composition of raw microalgae, MBC 750W and FBC 750W (before and after adsorption) based on weight percentage.

According to Figure 11, the prominent elements on all the samples were C, N, O, P, Cl and Ca. Both MA and Fe-MA contained high levels of Ca, P, and Cl and low levels of Na, Mg, Si, S, K, and Fe. The Fe content in MA might have occurred due to contamination, as its biochar MBC 750W did not contain any iron. The Ca content of Fe-MA was higher than in MA because the coagulation process used for harvesting forms flocs of microalgae and cations in dairy wastewater (Daneshvar et al., 2020). Similarly, the phosphorus content could also have originated from the dairy wastewater. Also, in a previous study, the sampling region of EDS affected the elemental composition (Wang et al., 2017). So, the heterogeneous distribution of crystal on the Fe-MA surface (Figure 8 (c-d)) could have affected the result of elemental composition and caused analytical errors. So, for this study, the EDS results might be useful for qualitative analysis and only a rough approximation of elemental composition.

MBC 750W had similar elemental distribution like MA. However, MBC 750W did not contain Fe and had lower amount of K and Si. The major components were still Ca and P as these elements form calcium phosphate and hydroxy calcium phosphate (Law et al., 2021) of the ash layer. Also, the washing step was not efficient in the removal of these compounds.

Additionally, phosphorus can also incorporate into the carbon matrix of biochar during pyrolysis (Binda et al., 2020). FBC 750W (before and after adsorption) showed a remarkable difference from MBC 750W, as it contained iron in about  $25\% \pm 5\%$  weight. In a previous study, biochar prepared at  $900\text{ }^{\circ}\text{C}$  from sludge coagulated with  $\text{FeCl}_3$  had similar iron content and the pyrolysis enriched the iron contained in sludge (Zhu et al., 2019). Comparing the elemental composition of FBC 750W before and after adsorption with ciprofloxacin showed presence of fluorine which was absent before adsorption. Thus, it confirms ciprofloxacin adsorption onto FBC 750W. Since, the biochar samples already contained chlorine, identification of chlorine could not be used for verification of adsorption for diclofenac.

#### 5.1.4 Surface functional groups

The FTIR spectroscopy was used to determine surface functional groups of the studied samples. The FTIR spectra of microalgal biomass with (Fe-MA) iron and without (MA) iron are shown in Figure 12.

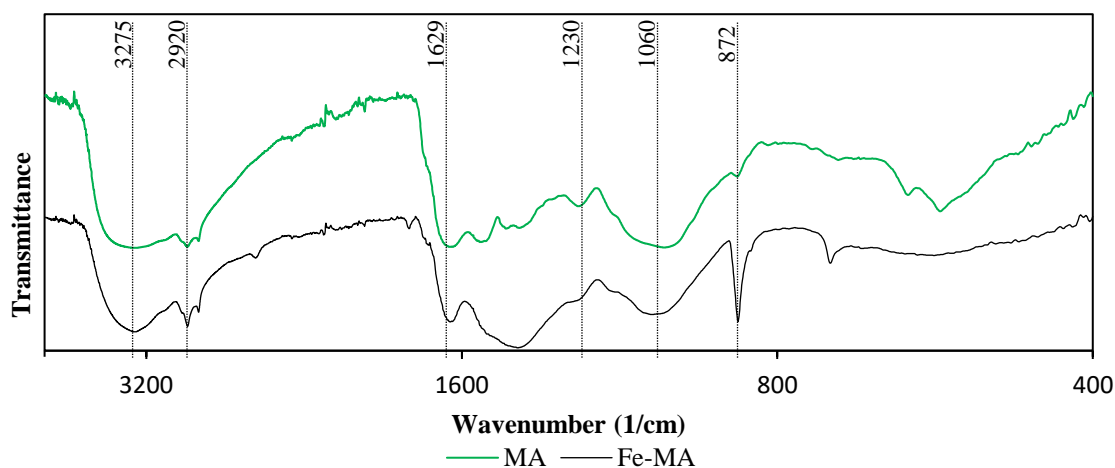


Figure 12. FTIR spectrum of microalgal biomass samples: MA and Fe-MA.

From Figure 12, the FTIR spectra of both microalgal biomasses were similar except in the fingerprint region (wavenumber  $< 1500\text{ cm}^{-1}$ ). In the figure, vertical dotted lines represent common peaks between the two different microalgal samples. Starting from the left, the strong broad peak around  $3275\text{ cm}^{-1}$  correspond to stretching of hydroxyl groups ( $-\text{OH}$ ) in a condensed phase and primary amides (Peter, 2011). The peak at  $2920\text{ cm}^{-1}$  accompanied by another small distinct peak at  $2847\text{ cm}^{-1}$  indicate the methylene  $\text{C}-\text{H}$  stretching bands

(Peter, 2011). The peak around  $1629\text{ cm}^{-1}$  represents aromatic conjugated C=O, C=N, and C=C bonds as well as deformation of –OH bond of water (Peter, 2011; Choi et al., 2020). Peaks at  $1230\text{ cm}^{-1}$  and  $1060\text{ cm}^{-1}$  represent aromatic and C–O stretching, respectively (Choi et al., 2020). Since elemental composition showed presence of phosphorus, the peak at  $1060\text{ cm}^{-1}$  could also represent dibasic phosphates (Peter, 2011; Binda et al., 2020). The peak at  $875\text{ cm}^{-1}$  corresponds to carbonate groups (Choi et al., 2020). Moreover, for MA, other peaks at  $1520\text{ cm}^{-1}$ ,  $1446\text{ cm}^{-1}$ ,  $1401\text{ cm}^{-1}$ , and  $601/559\text{ cm}^{-1}$  represent –CNH stretching in a secondary amide,  $\text{CH}_2/\text{CH}_3$  groups, inorganic nitrate, and NH/NH<sub>2</sub> bonds from amides of proteins, respectively (Peter, 2011; Choi et al., 2020). In Fe-MA samples, the intense broad band at  $1400\text{ cm}^{-1}$  represents functional groups such as carbonates, nitrates, and ammonium of inorganic salts (Peter, 2011), which could have coagulated together with microalgae. A small peak in  $710\text{ cm}^{-1}$  could represent NH group of secondary amines (Peter, 2011). Overall, raw microalgal samples had diverse organic and inorganic functional groups.

The changes in surface functional groups after pyrolysis can be seen from the FTIR spectra of microalgal biochar samples which is presented in Figure 13.

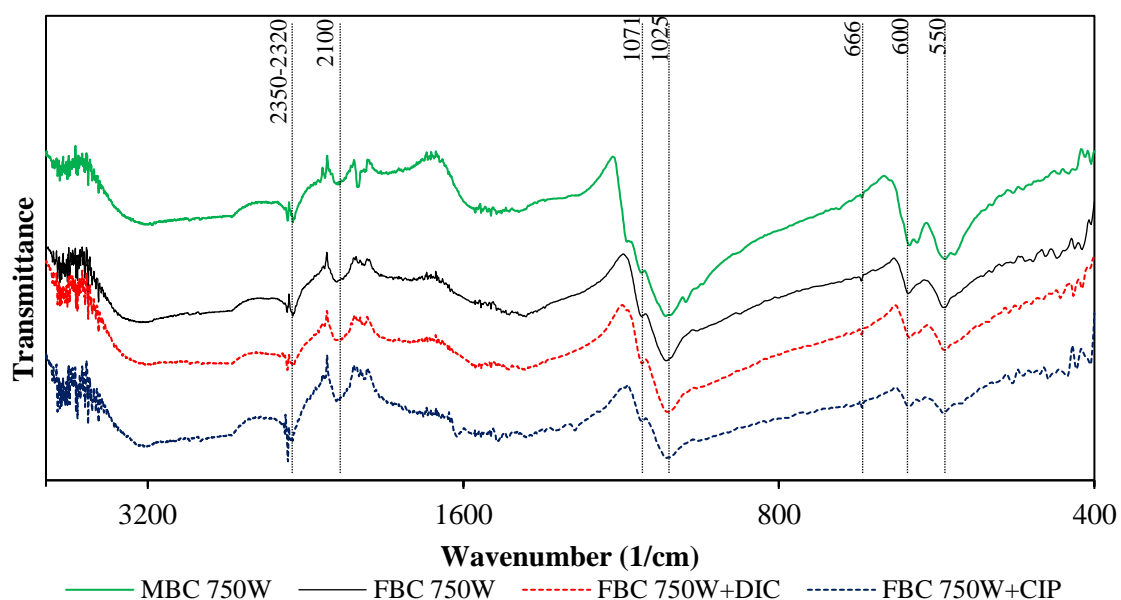


Figure 13. FTIR spectrum of microalgal biochar samples, MBC 750 W and FBC 750W (before and after adsorption).

According to Figure 13, all biochar samples had similar FTIR spectra. However, the spectra were different from that of microalgae. First, the peaks representing the hydroxyl group and

methylene from alkyl groups disappeared, indicating dehydration and demethylation after pyrolysis (Patel et al., 2021). Then, multiple medium intensity peaks in the region between  $1600\text{ cm}^{-1}$  and  $1370\text{ cm}^{-1}$  for all the biochar samples could represent aromatic groups (Peter, 2011). The peak transmittances at  $2320\text{ cm}^{-1}$  -  $2330\text{ cm}^{-1}$  and  $2100\text{ cm}^{-1}$  could represent PH stretches,  $\text{C}\equiv\text{C}$  bond or cumulated double bonds such as  $-\text{N}=\text{C}=\text{O}$  (Peter, 2011). In addition, the shoulder peak between  $1000\text{ cm}^{-1}$  and  $1300\text{ cm}^{-1}$  ( $1071\text{ cm}^{-1}$ ) could represent the presence of inorganic phosphates (Peter, 2011). The peak intensity at  $1025\text{ cm}^{-1}$  represents ether group  $\text{C}-\text{O}-\text{C}$  (Patel et al., 2021). Finally, peaks at  $666\text{ cm}^{-1}$ ,  $620\text{ cm}^{-1}$  and  $555\text{ cm}^{-1}$  could be due to metal oxides (Peter, 2011) and aromatic  $-\text{CH}$  out of phase deformation (Patel et al., 2021).

For FBC 750W + CIP, the peak at  $1251\text{ cm}^{-1}$  can represent aryl ring  $\text{C}-\text{F}$  stretch from ciprofloxacin molecule (Peter, 2011). The spikes near  $1620\text{ cm}^{-1}$  fall under the double bond region and represent  $\text{C}=\text{O}$ ,  $\text{C}=\text{C}$  or  $\text{C}=\text{N}$  stretching. Also, the presence of peaks between  $1620\text{ cm}^{-1}$  and  $1420\text{ cm}^{-1}$  indicates the presence of aromatic and heteroaromatic rings (Peter, 2011). These types of bonds are prevalent in a ciprofloxacin molecule as well as expected in biochar. Moreover, pure ciprofloxacin has a characteristic peak (for  $\text{C}=\text{C}$ ) at approximately  $1620\text{ cm}^{-1}$  (Ashiq, Sarkar, et al., 2019). These pieces of evidence indicate that ciprofloxacin possibly adsorbed onto FBC 750W. On the other hand, distinct peaks after adsorption of diclofenac were not observed probably because the amount of diclofenac adsorbed was insufficient to visualize the changes in the FTIR spectra.

#### 5.1.5 X-Ray diffraction

XRD was used to determine crystalline phase of iron in microalgal biomass and microalgal biochar. The XRD result of microalgal biomasses are present in Figure 14.

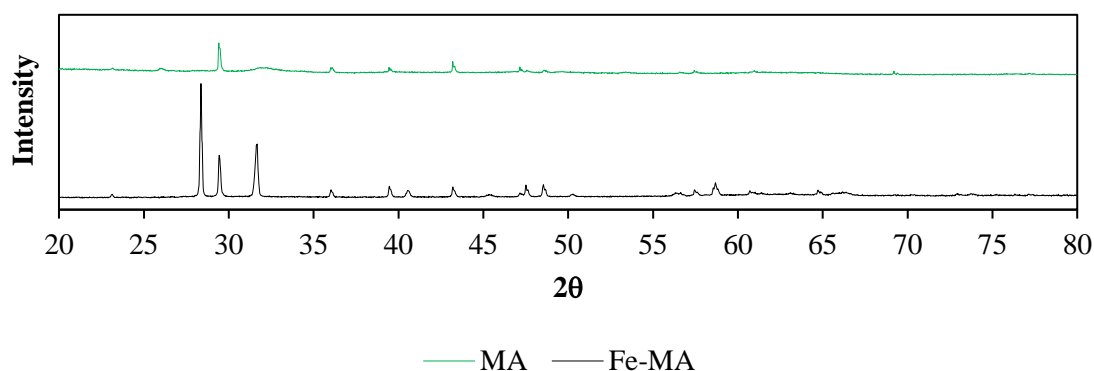


Figure 14. XRD spectra of microalgal biomasses MA and Fe-MA.

According to Figure 14, XRD patterns of both microalgal biomasses (MA and Fe-MA) do not indicate the presence of iron species. So, the iron might be in non-crystalline phases. Moreover, sharp peaks indicate the presence of other crystalline phases that could represent crystals seen in the SEM images (Figure 8). These crystals could be calcium carbonate, calcium phosphate, or silica (Choi et al., 2020).

The XRD result of biochar samples are presented in Figure 15.

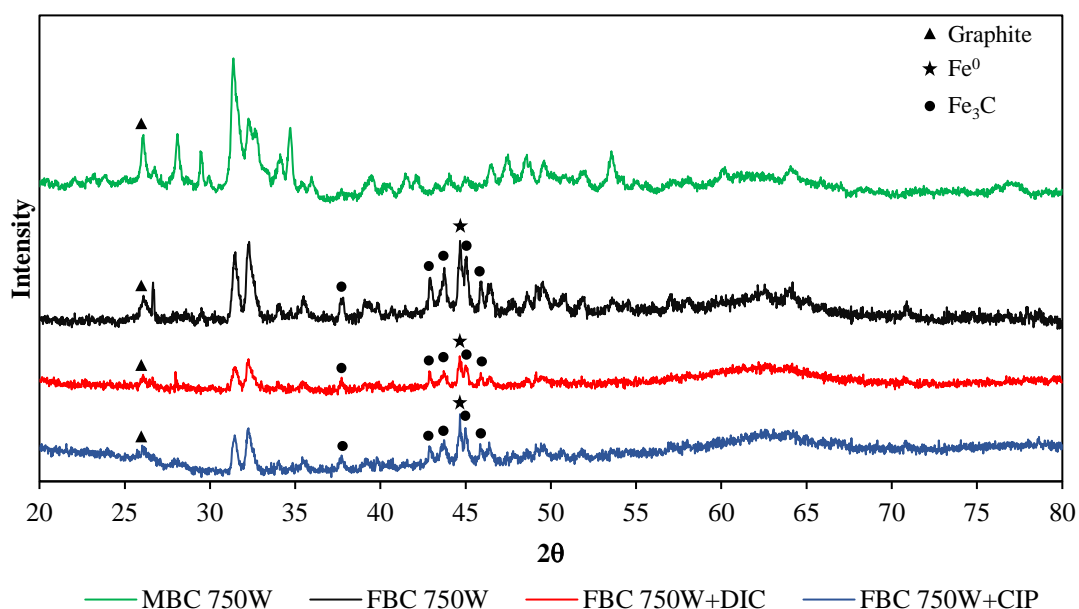


Figure 15. XRD spectra of microalgal biochar samples: MBC 750W and FBC 750W (before and after adsorption).

From Figure 15, many peaks detected in microalgal biochar samples indicate the presence of different crystalline structures. Overall, all biochar showed peak intensities at  $2\theta = 26.1^\circ$  which represents graphitic carbon (Zhao et al., 2019; Lei et al., 2021). Then, in case of FBC 750W (before and after adsorption) peaks  $2\theta = 37.72^\circ$ ,  $42.91^\circ$ ,  $43.71^\circ$ ,  $45.01^\circ$ , and  $45.87^\circ$  represents iron carbide,  $\text{Fe}_3\text{C}$  (Zhao et al., 2019, 2020; Lei et al., 2021) while peak at  $2\theta = 44.67^\circ$  represents zero-valent iron ( $\text{Fe}^0$ ) (Zhao et al., 2019, 2020).

After adsorption, the overall peak intensities diminished indicating loss of crystallinity after adsorption. Also, from SEM images, crystalline structures decreased after adsorption (Figure 9 (c-d) and 10 (a-d)). However, the peaks associated with  $\text{Fe}^0$  and  $\text{Fe}_3\text{C}$  remained stable. In previous studies by Zhao et al. (2019, 2020), stable  $\text{C}/\text{Fe}_3\text{C}/\text{Fe}^0$  composite was formed when biochar and iron salts were thermally treated at  $800^\circ\text{C}$ . Also, Zhao et al (2020) reported that the XRD peak referring to  $\text{Fe}^0$  vanished after 30 min of reaction with oxytetracycline, and a peak representing iron oxide appeared. However, peaks representing  $\text{Fe}^0/\text{Fe}_3\text{C}$  composite did not shift, even after 1440 min of reaction. Thus, pyrolysis of microalgal biomass harvested by coagulation with  $\text{FeCl}_3$  at  $750^\circ\text{C}$  could possess stable  $\text{C}/\text{Fe}_3\text{C}/\text{Fe}^0$  composite characteristics.

Overall, pyrolysis of microalgal biochar, harvested with iron, at  $750^\circ\text{C}$  produced porous biochar containing graphitic carbon, rich oxygen and nitrogen containing functional groups, iron carbide, zero-valent iron, and minerals. Additionally, presence of zero-valent iron and iron carbide could aid in removal of pharmaceuticals via redox reactions (Zhao et al., 2020; Li et al., 2021a).

## 5.2 Batch tests

Batch tests were conducted to identify the best adsorbent material and adsorption conditions. Also, isotherms, kinetics and effects of competing ions were studied under batch tests.

### 5.2.1 Screening test

The screening test was done to select best biochar material based on removal efficiency and adsorption capacity. The results of adsorption performance of iron containing and iron free microalgal biochar, prepared at 500 and 750 °C, for diclofenac and ciprofloxacin are shown in Figure 16 (a-b) and Figure 17 (a-b), respectively.

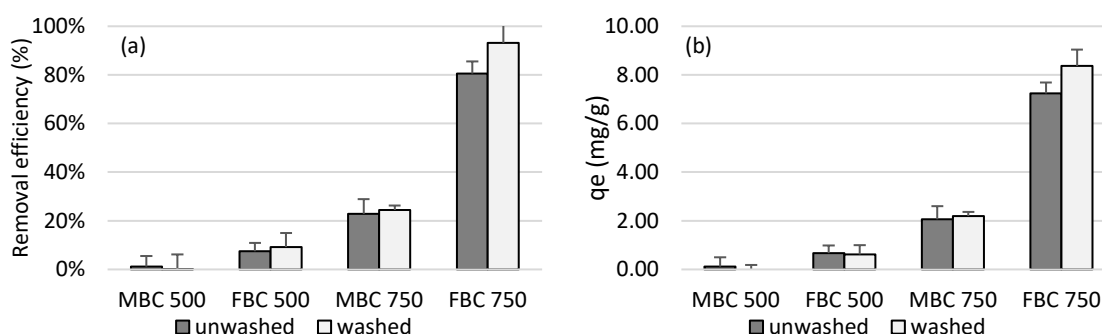


Figure 16. Removal efficiency (a) and adsorption capacity (b) of diclofenac by prepared biochar samples [adsorbent dosage 1 g/L, adsorbate concentration 10 mg/L and 180 min contact time].

According to Figure 16, the biochar made from microalgae harvested with  $\text{FeCl}_3$  had better adsorption performance than the microalgae harvested by centrifugation. Also, increasing pyrolysis temperature from 500 °C to 750 °C increased adsorption performance of microalgal biochar. In addition, washing improved adsorption performance of biochar. For the adsorption of diclofenac, FBC 750W had the highest removal efficiency and adsorption capacity of 93% and 8.37 mg/g, respectively.



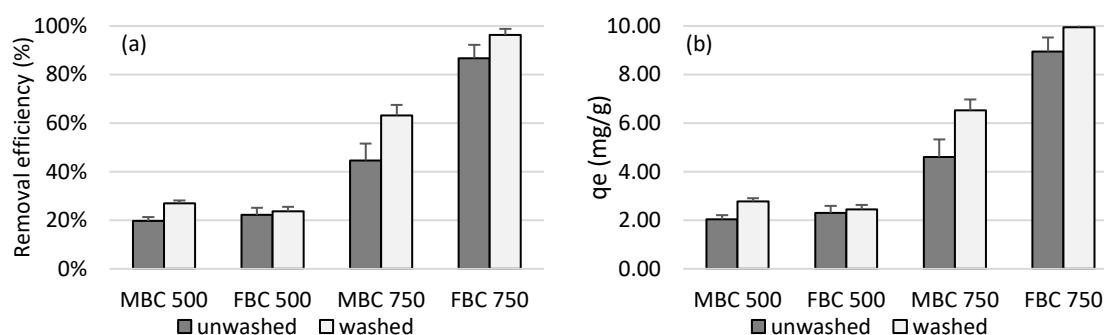


Figure 17. Removal efficiency (a) and adsorption capacity (b) of ciprofloxacin by prepared biochar samples [adsorbent dosage 1 g/L, adsorbate concentration 10 mg/L and 180 min contact time].

According to Figure 17, screening test result for adsorption of ciprofloxacin showed similar result to that of adsorption of diclofenac, where iron content, higher temperature and washing process improved the adsorption performance. FBC 750W had highest removal efficiency and adsorption capacity of 96% and 9.94 mg/g, respectively. Overall, the adsorption performance of FBC 750W was highest for adsorption of both pharmaceuticals and was thus selected for further adsorption experiments.

### 5.2.2 Optimization studies

To determine the best values of adsorbent dosage, adsorbate concentration and contact time their interactive effects on the highest adsorption capacity and removal efficiency were studied. The 3D surfaces were plotted to using any two variables at a constant third variable.

#### *Adsorbent dosage*

The interactive effects of initial concentration and contact time on removal efficiency of ciprofloxacin and diclofenac at three adsorbent dosages are presented by surface plots in Figure 18 (I-II).

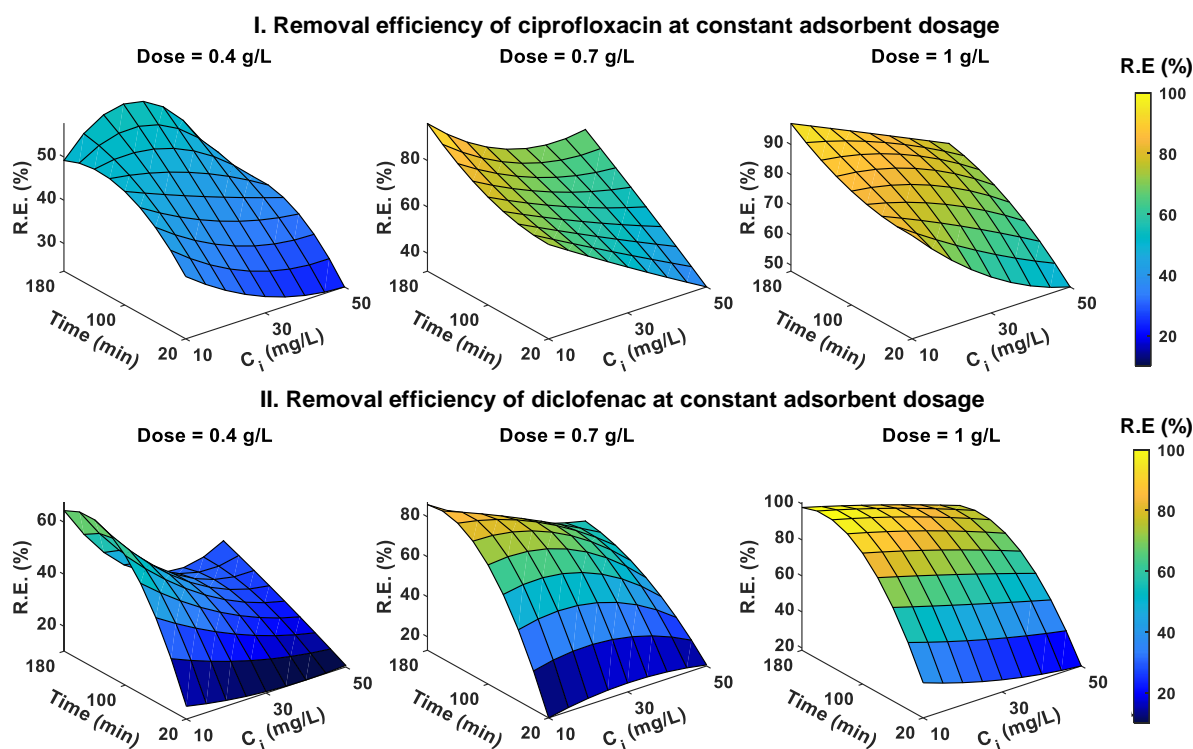


Figure 18. Interaction of adsorbate concentration and contact time at three adsorbent dosages on removal efficiency of I. Ciprofloxacin and II. Diclofenac.

According to Figure 18 (I-II), increasing adsorbent dosage improved removal efficiency for both pharmaceuticals, as indicated by respective colour codes. Then, initial adsorbate concentration and contact time had an antagonistic effect on the removal efficiency of both ciprofloxacin and diclofenac. Increasing initial adsorbate concentration tends to decrease removal efficiency whereas, increasing contact time tends to increase removal efficiency. Thus, maximum removal efficiency is achieved at lower initial concentration and higher contact time. Higher adsorbate concentration decreases removal efficiency because as the adsorbent becomes saturated, excess adsorbate will remain in the liquid phase. In case of the contact time, adequate time is required to achieve dynamic equilibrium and it is governed by diffusion and reaction kinetics (Worch, 2012). After achieving the dynamic equilibrium, the contact time will not have any effect on the removal efficiency, which will be indicated by a plateau. At a contact time of 20 min, removal efficiency is quite low for both ciprofloxacin and diclofenac. However, from 100 to 180 mins, the removal efficiency starts to stabilize which indicate dynamic equilibrium is in proximity. In case of ciprofloxacin, plateau was not achieved at any given adsorbent dosage. However, such plateau started to form in case of diclofenac at adsorbent dosage of 1 g/L.

The surface plots for interactive effects of initial concentration and contact time on adsorption capacities of ciprofloxacin and diclofenac at three adsorbent dosages are provided in Figure 19 (I-II).

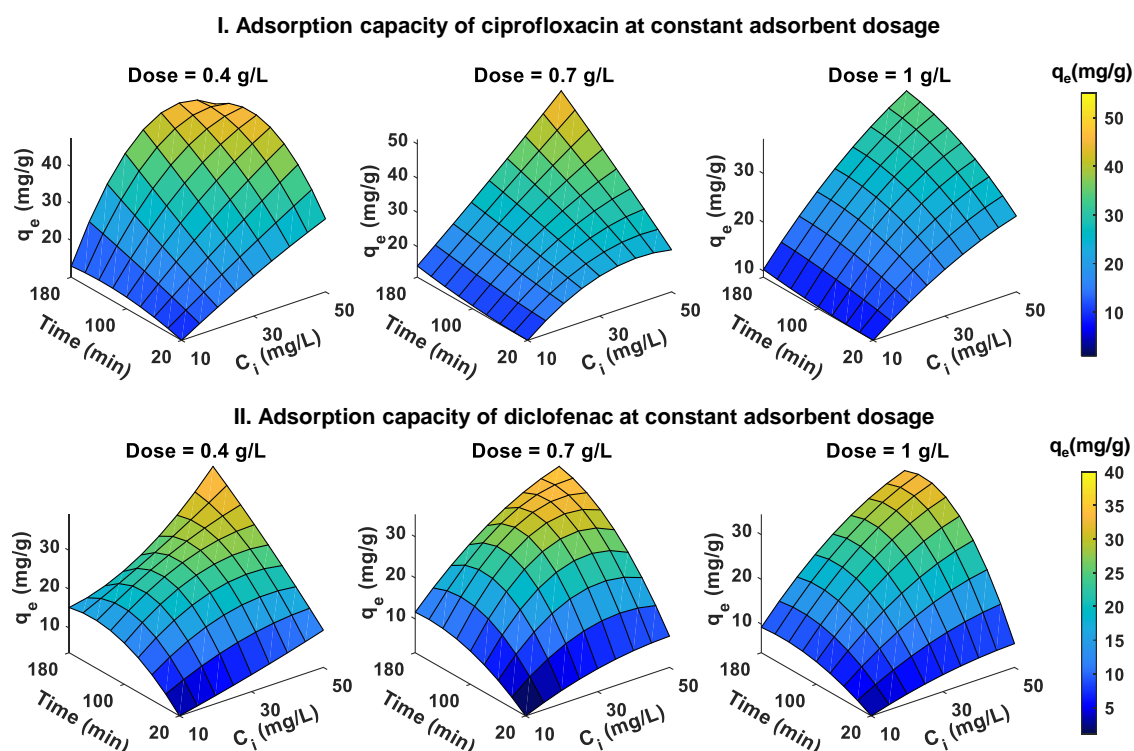


Figure 19. Interaction of adsorbate concentration and contact time at three adsorbent dosages on adsorption capacity of I. Ciprofloxacin and II. Diclofenac.

According to Figure 19 (I-II), initial adsorbate concentration and contact time had a synergistic effect on the adsorption capacity of both pharmaceuticals. Increasing adsorbate concentration increased adsorption capacity and maximum adsorption capacity is achieved at dynamic equilibrium. However, after achieving possible maximum adsorption capacity, increasing contact time and initial concentration will not further increase adsorption capacity and a plateau is formed. For all adsorbent dosages, maximum adsorption capacities were achieved at the initial adsorbate concentration of 50 mg/L and contact time of 180 min.

### Adsorbate concentration

The interactive effects of adsorbent dosage and contact time at three constant concentrations of adsorbate on the removal efficiency of ciprofloxacin and diclofenac are presented in Figure 20 (I-II).

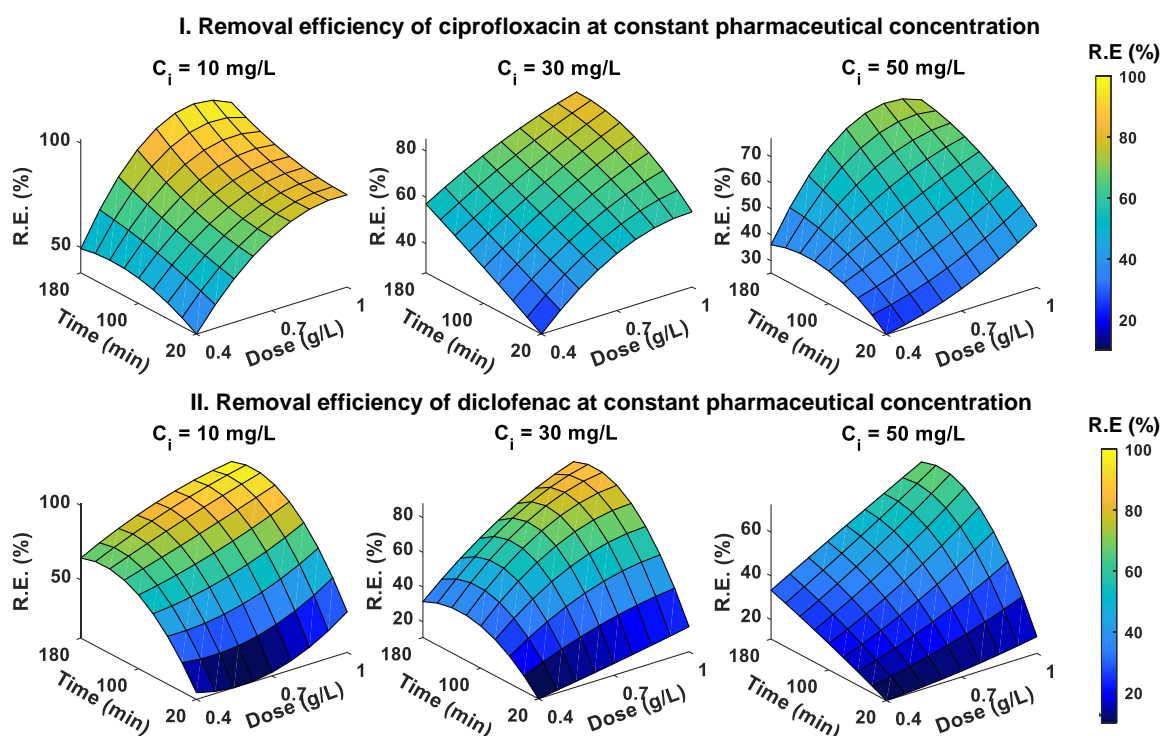


Figure 20. Interaction of contact time and adsorbate dosage at three adsorbate concentrations on removal efficiency of I. Ciprofloxacin and II. Diclofenac.

According to Figure 20 (I-II), increasing adsorbate concentration decreases the removal efficiency of both pharmaceuticals. The contact time and adsorbent dosage have a synergistic effect on the removal efficiency. At constant adsorbate concentration, increasing adsorbent dosage increases available adsorption sites, which increases the removal efficiency. Also, as mentioned earlier, adequate time is required for adsorption. So, at a contact time of 20 min, increasing adsorbent dosage did not significantly improve removal efficiency. However, at higher contact times (100 and 180 min), there was a significant synergy between adsorbent dosage and contact time.

Adsorption capacities for ciprofloxacin and diclofenac at different contact times and adsorbent dosage in response to three adsorbate concentrations are presented in Figure 21 (I-II).

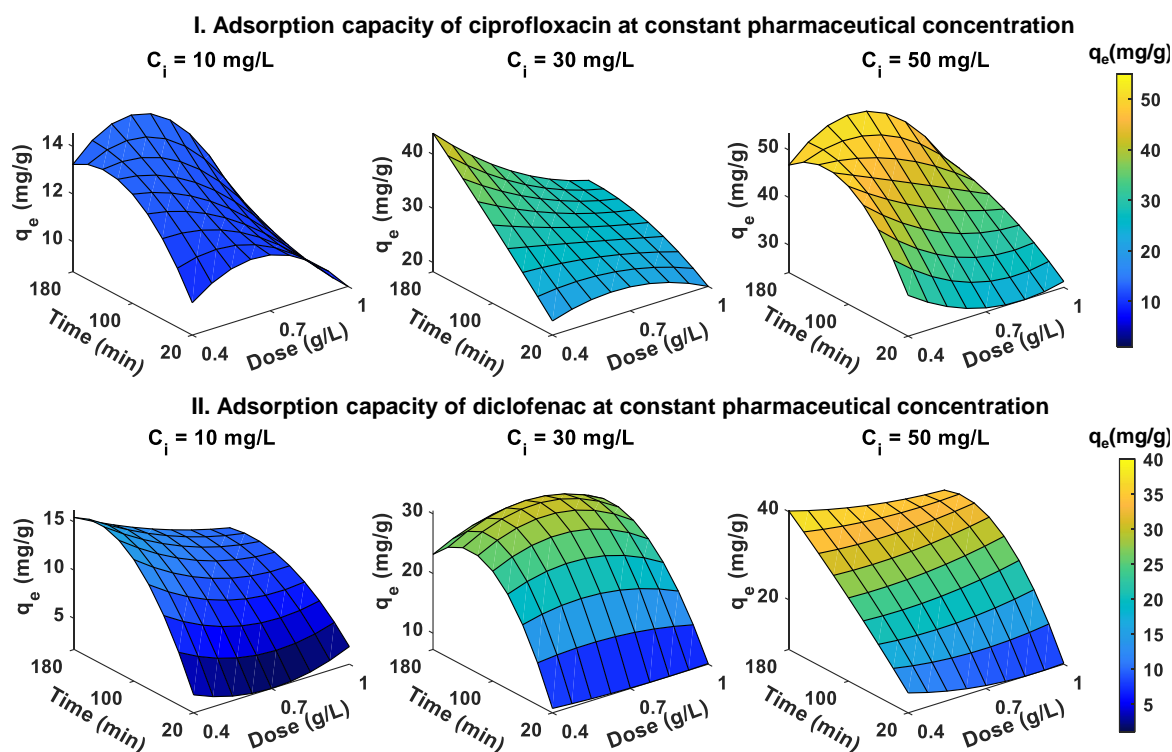


Figure 21. Interaction of contact time and adsorbate dosage at constant adsorbate concentration on adsorption capacity of I. Ciprofloxacin and II. Diclofenac.

According to Figure 21 (I-II), the increasing initial concentrations of both pharmaceuticals increased the adsorption capacity. Overall, increasing contact time increased adsorption capacity whereas, increasing adsorbent dosage did not affect the adsorption capacity. For a given concentration, there is a certain adsorbent dosage to achieve maximum adsorption capacity. When the adsorbent dosage becomes higher, the adsorption capacity will diminish because of excess adsorbent. For adsorption of ciprofloxacin, maximum adsorption capacities were achieved at adsorbent dosage of 0.7 g/L and contact time of 180 mins, at initial concentrations of 10 mg/L and 50 mg/L. However, for adsorption of diclofenac, adsorption capacities were affected more by the contact time than the adsorbent dosage.

### Contact time

The surface plots of the interaction of the initial adsorbate concentration and adsorbent dosage on removal efficiency of ciprofloxacin and diclofenac are provided in Figure 22 (I-II).

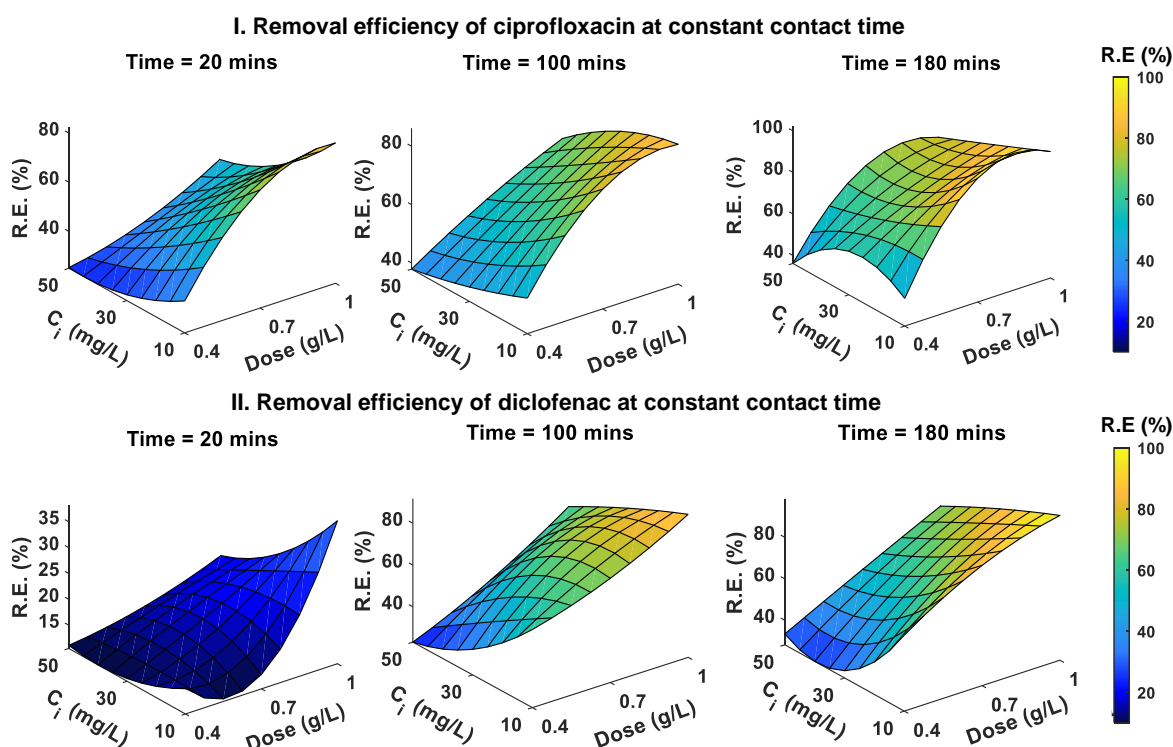


Figure 22. Interaction of initial adsorbate concentration and adsorbate dosage at three contact times on removal efficiency of I. Ciprofloxacin and II. Diclofenac.

According to Figure 22 (I-II), increasing the contact time increased removal efficiency. Then, the initial adsorbate concentration and adsorbent dosage had an antagonistic effect on removal efficiency. Increasing initial adsorbate concentration reduced removal efficiency whereas, increasing adsorbent dosage increased removal efficiency. Thus, the removal efficiency approached maximum at lower initial adsorbate concentration and higher adsorbent dosage.

The surface plots for the interaction of the initial adsorbate concentration and adsorbent dosage on adsorption capacity of ciprofloxacin and diclofenac are provided in Figure 23 (I-II).

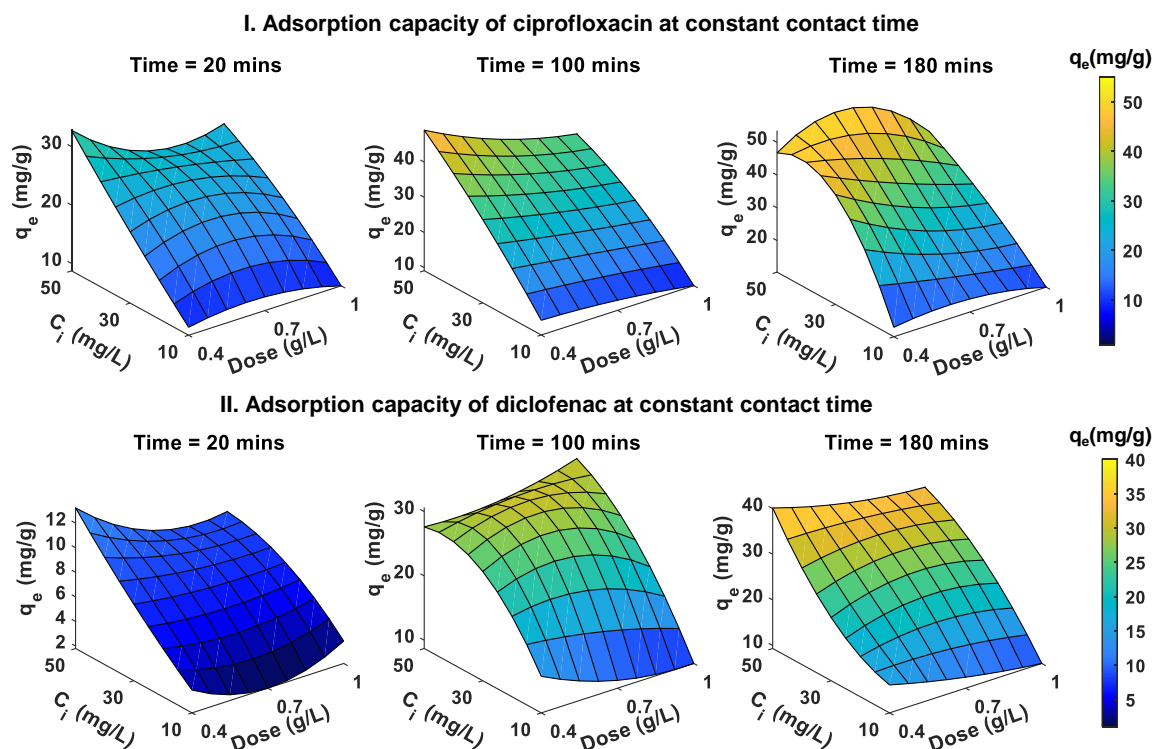


Figure 23. Interaction of initial adsorbate concentration and adsorbate dosage at constant contact time on adsorption capacity of I. Ciprofloxacin and II. Diclofenac.

Figure 23 (II) shows that increasing the contact time increases adsorption capacity. Then, the initial adsorbate concentration and adsorbent dosage also had an antagonistic effect on adsorption capacity. Here, increasing initial adsorbate concentration increased adsorption capacity in cases of both pharmaceuticals. On the contrary, increasing adsorbent dosage slightly reduced adsorption capacity.

In summary, the removal efficiency was directly related to the adsorbent dosage and contact times and inversely related to the initial adsorbate concentration. In case of adsorption capacity, it had an inverse relationship with the adsorbent dosage and a direct relationship with the initial adsorbate concentration and the contact time. Maximizing adsorption capacity and removal efficiency required an adequate contact time. Even though the contact time of 180 min showed maximum adsorption capacity and removal efficiency in all the optimization experiments, clear plateau structures were not seen. Therefore, kinetic experiments were conducted before isotherm experiments to determine the proper contact time to achieve dynamic equilibrium.

Then, adsorbent dosage and initial adsorbate concentration had an antagonistic effect on removal efficiency and adsorption capacity. Overall, the highest removal efficiency for ciprofloxacin (96%) and diclofenac (98%) was achieved at an adsorbent dosage of 1 g/L, the initial adsorbate concentration of 10 mg/L and contact time 180 mins. The highest adsorption capacity for ciprofloxacin (51.37 mg/g) was achieved at the adsorbent dosage of 0.7 g/L, the initial adsorbate concentration of 50 mg/L, and the contact time 180 mins. Similarly, the highest adsorption capacity for diclofenac (39.19 mg/g) was achieved at the adsorbent dosage of 0.4 g/L, the initial adsorbate concentration of 50 mg/L, and the contact time 180 mins. Overall, adsorption capacities were maximal when the initial adsorbate concentration was 50 mg/L. The optimal adsorbent dosage was 0.7 g/L for adsorption of ciprofloxacin clear optimal value for diclofenac was not observed. Therefore, the adsorbent dosage of 0.7 g/L and the initial adsorbate concentration of 50 mg/L were used as optimum values.

### 5.2.3 Adsorption Kinetics

Adsorption kinetics were performed to determine the effect of contact time on the adsorption capacity of studied pharmaceuticals onto FBC 750W and to determine the respective rate of adsorption. Accordingly, reaction kinetic modelling was applied to determine the nature of the adsorption. The result of reaction kinetic modelling for ciprofloxacin and diclofenac are presented in Figure 24 (a-b).

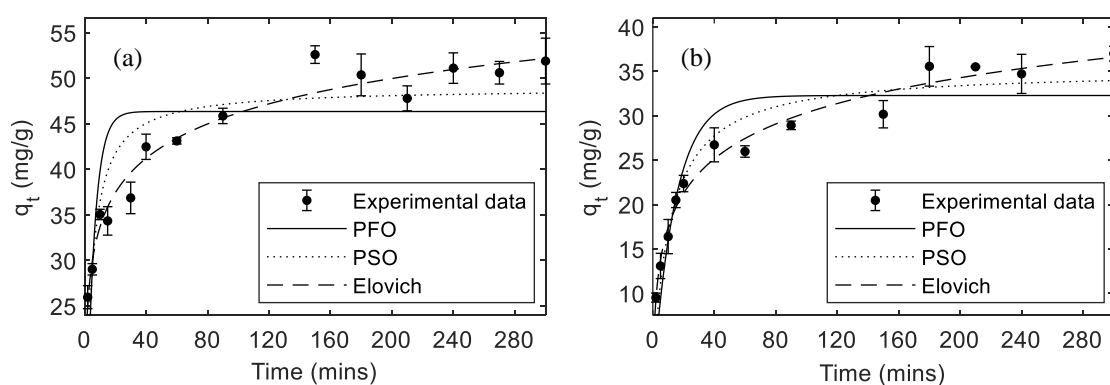


Figure 24. Adsorption kinetics of ciprofloxacin (a) and diclofenac (b) onto FBC 750W at adsorbate concentration 50 mg/L, adsorbent dosage 0.7 g/L and pH (CIP =  $7.03 \pm 0.36$ ; DIC =  $7.69 \pm 0.29$ ).



According to Figure 24 (a-b), adsorption of both pharmaceuticals was fast at the beginning of the reaction, given by the rapid rise in adsorption capacity in a short contact time of 30 min. After that, the rate of adsorption started to slow down and began to stabilize. In dynamic equilibrium, the adsorption rate is constant, which occurs after 150 min for ciprofloxacin and 180 min for diclofenac. The high rate of adsorption in the initial stage is due to vacant adsorption sites which allows rapid uptake of adsorbate molecules. As the adsorbent saturates, the number of viable adsorption sites decreases which reduces the adsorption rate (Ashiq, Adassooriya, et al., 2019). Consequently, the adsorption process slows down until the state of dynamic equilibrium is achieved. The experimental equilibrium adsorption capacities ( $q_e$ ) were 51.89 mg/g and 37.00 mg/g for ciprofloxacin and diclofenac, respectively, under optimized conditions. The model parameters for reaction kinetics models are provided in Table 8.

Table 8. Adsorption reaction kinetic model parameters and error function values for ciprofloxacin and diclofenac.

Kinetic Model		Ciprofloxacin	Diclofenac
<b>Pseudo-first order</b> $q_t = q_e * (1 - e^{-k_1 * t})$	$k_1$ [1/min]	0.194	0.068
	$q_e$ [mg/g]	46.35	32.19
	$R^2$	0.54	0.84
	RMSE	6.29	3.72
<b>Pseudo-second order</b> $q_t = \frac{(k_2 * q_e^2) * t}{1 + k_2 * q_e * t}$	$k_2$ [g/mg/min]	$5.93 \times 10^{-3}$	$2.67 \times 10^{-3}$
	$q_e$ [mg/g]	48.92	35.06
	$R^2$	0.79	0.93
	RMSE	4.25	2.47
<b>Elovich</b> $q_t = \left(\frac{1}{\beta}\right) * \ln(1 + (\alpha * \beta * t))$	$\alpha$ [mg /g/min]	262.67	11.71
	$\beta$ [g/mg]	0.184	0.176
	$R^2$	0.96	0.98
	RMSE	1.85	1.31

Based on RMSE (root mean squared error) and  $R^2$  values, the Elovich model provided the best fit which represents chemisorption onto a heterogeneous surface (Wang et al., 2020). Then, the high initial adsorption constant ( $\alpha$ ) and low desorption constant ( $\beta$ ) show that the adsorption of ciprofloxacin and diclofenac onto FBC 750W is favourable (Keerthanan et al., 2020). Additionally, for kinetic data of diclofenac, the pseudo-second order model fitted well and the model “ $q_e$ ” values were quite close to the experimental “ $q_e$ ” value. Moreover, the adsorption rate constants of fitted models show that adsorption for ciprofloxacin is faster than for diclofenac.

To determine the role of diffusion in adsorption and rate-controlling step Weber and Morris intraparticle diffusion model was fitted to the plot of  $q_t$  vs  $t^{0.5}$ . The result of fitting the intraparticle diffusion model is shown in Figure 25.

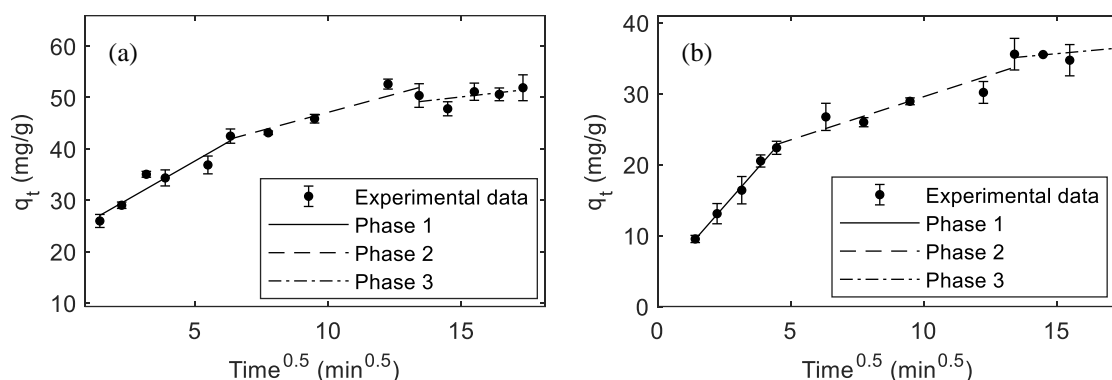


Figure 25. Weber and Morris intraparticle diffusion model for adsorption of ciprofloxacin (a) and diclofenac (b) onto FBC 750W at adsorbate concentration 50 mg/L and adsorbent dosage 0.7 g/L.

According to Figure 25, the plot of  $q_t$  vs  $t^{0.5}$  for adsorption of ciprofloxacin and diclofenac were fitted with 3 different straight lines, each representing phases 1, 2 and 3. Phase 1 is associated with external diffusion and pharmaceutical molecules are rapidly adsorbed onto external surface of FBC 750W (Zeng et al., 2018). It occurred during first 40 and 30 min for ciprofloxacin and diclofenac respectively. As the external surface became saturated, pharmaceutical molecules started to diffuse into the pores of the adsorbent which is described by phase 2 (Zeng et al., 2018; Luo et al., 2019). Pore diffusion has higher mass transfer restrictions compared to external diffusion (Luo et al., 2019). Therefore, the rate of adsorption drops, and the intra-particle diffusion dominates the adsorption rate, during phase 2. In this case, the phase 2 occurred after phase 1 and lasted for up to 150 and 180 min for ciprofloxacin and diclofenac, respectively. Finally, the phase 3 has slow rising slope where the adsorbent is mostly saturated and associated with adsorption equilibrium (Luo et al., 2019). Thus, adsorption of ciprofloxacin and diclofenac started to equilibrate after 150 and 180 min, respectively. It should be noted that since, none of the lines passed through origin, in each phases complex process and combination of intraparticle and external diffusion takes place (Qiu et al., 2009; Wang et al., 2020). Further, the model parameters for diffusion kinetics model are provided in Table 9.

Table 9. Adsorption diffusion kinetic model parameters and error function values for ciprofloxacin and diclofenac.

Kinetic Model			Ciprofloxacin	Diclofenac
<b>Weber and Morris Intraparticle diffusion model</b>  $q_t = (K_{ID} * t^{0.5})$	Phase 1	$k_{ID}$ [mg/g/min <sup>0.5</sup> ]	2.96	4.27
		$c$ [mg/g]	22.85	3.43
		$R^2$	0.91	0.99
		RMSE	1.93	0.45
	Phase 2	$k_{ID}$ [mg/g/min <sup>0.5</sup> ]	1.41	1.22
		$c$ [mg/g]	33.01	17.40
		$R^2$	0.89	0.88
		RMSE	1.73	1.69
	Phase 3	$k_{ID}$ [mg/g/min <sup>0.5</sup> ]	0.585	0.395
		$c$ [mg/g]	41.34	29.55
		$R^2$	0.34	0.40
		RMSE	1.44	0.98

In Table 9,  $k_{ID}$  gives the rate constants and “ $c$ ” values represent intercepts and are associated with the thickness of boundary layer for each phase (Afzal et al., 2018). For adsorption of both diclofenac and ciprofloxacin, in all the phases  $c \neq 0$ , indicating once again that the rate is determined by combination of surface diffusion and internal diffusion. The rate constants from intraparticle diffusion model decreases while the “ $c$ ” values increase from phase 1 to phase 3. Based on the rate constants at different phases, diclofenac is more rapidly adsorbed than ciprofloxacin during phase 1 but adsorption of ciprofloxacin becomes faster during phase 2 and 3. In addition, “ $c$ ” values are lower for all the phases of diclofenac adsorption compared to adsorption of ciprofloxacin. Therefore, in case of adsorption of ciprofloxacin, film diffusion played a major role as the effect of boundary layer was larger (Daneshvar et al., 2017; Afzal et al., 2018). Nevertheless, both external diffusion and intra-particle diffusion played important role in the adsorption of studied pharmaceuticals onto FBC 750W.

#### 5.2.4 Adsorption Isotherm

Isotherm studies for ciprofloxacin and diclofenac were conducted with an adsorbent dosage of 0.7 g/L, contact time of 180 min, and initial adsorbate concentrations of 1, 5, 10, 20, 30, 40, 60, 80, and 100 mg/L. The plots of  $C_e$  vs.  $q_e$  resulting adsorption isotherms of ciprofloxacin and diclofenac are provided in Figure 26.

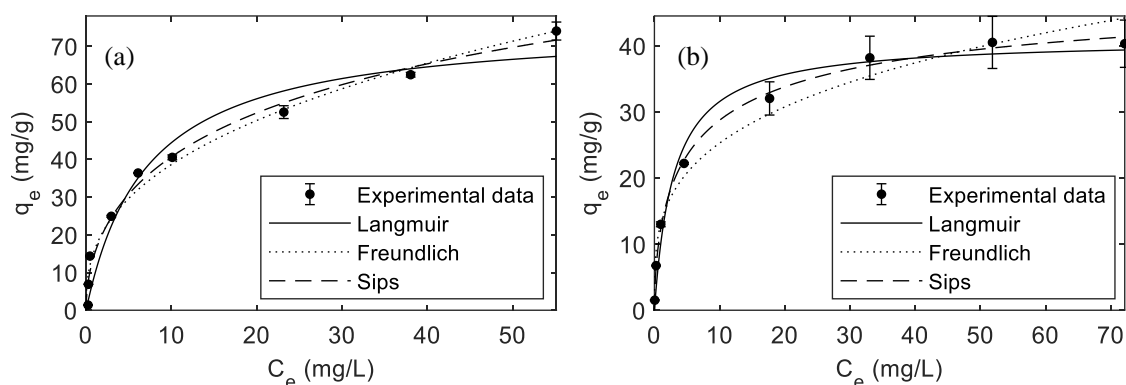


Figure 26. Adsorption isotherms of ciprofloxacin (a) and diclofenac (b) onto FBC 750W at adsorbent dosage 0.7 g/L and contact time 180 mins.

According to Figure 26, the steep slope reveals almost complete removal of ciprofloxacin and diclofenac at lower initial adsorbate concentration. As the initial adsorbate concentration increases, the adsorption capacity slows down because the adsorbent starts to saturate. For ciprofloxacin, the isotherm curve did not reach a plateau indicating a higher adsorption capacity might be possible for higher initial adsorbate concentration. However, for diclofenac, the maximum adsorption capacity seems to have been achieved.

The parameters and error function values of fitted isotherm models are provided in Table 10. All the models showed a good fit ( $R^2 > 0.95$ ) to the experimental data for adsorption of both ciprofloxacin and diclofenac. Maximum Langmuir adsorption capacity of FBC 750W for ciprofloxacin and diclofenac were found to be 75.97 mg/g and 40.99 mg/g, respectively. The predicted maximum adsorption capacities for diclofenac and ciprofloxacin were close to the experimental adsorption capacity (40.31 mg/g for diclofenac and 74.02 mg/g for ciprofloxacin).

Table 10. Isotherm model parameters and error function values for ciprofloxacin and diclofenac

<b>Isotherm Model</b>		<b>Ciprofloxacin</b>	<b>Diclofenac</b>
<b>Langmuir</b> $q_e = \left( \frac{C_e * K_L * q_m}{1 + (C_e * K_L)} \right)$	$K_L$ [L/mg]	0.141	0.334
	$q_m$ [mg/g]	75.97	40.99
	$R^2$	0.96	0.98
	RMSE	5.59	2.62
<b>Freundlich</b> $q_e = K_F * C_e^{\frac{1}{n}}$	$K_F$ [(mg/g) (L/mg) <sup>1/n</sup> ]	16.057	13.178
	1/n	0.38	0.28
	$R^2$	0.98	0.97
	RMSE	3.81	3.01
<b>Sips</b> $q_e = \frac{q_m * (K_S * C_e)^{n_s}}{1 + (K_S * C_e)^{n_s}}$	$K_S$ [L/mg]	0.015	0.151
	$q_m$ [mg/g]	150.89	51.19
	$n_s$	0.52	0.60
	$R^2$	0.98	0.99
	RMSE	3.61	1.08

Again, based on  $R^2$  and RMSE values, the Sips model was the best fit. However, the predicted maximum adsorption capacities from the Sips model were higher than the experimental value. The next best model that described the adsorption data of ciprofloxacin and diclofenac were the Freundlich isotherm model and Langmuir isotherm model, respectively. Thus, ciprofloxacin and diclofenac might be adsorbed onto heterogenous FBC 750W by forming multilayer and monolayer, respectively. The value of Freundlich adsorption intensity parameter, 1/n is between 0 and 1 ( $0 < 1/n < 1$ ) for adsorption of both ciprofloxacin and diclofenac, indicating favourable adsorption (Al-Ghouti et al., 2020).

#### 5.2.5 Comparison with commercial granular activated carbon

Biochar was introduced as an alternative to activated carbon. Therefore, the adsorption capacity of biochar synthesized in this study was compared with commercially available granular activated carbon under similar working conditions (temperature, adsorbent dosage, initial pH, contact time and initial adsorbate concentration). The adsorption isotherms of MBC 750W, FBC 750W and commercial activated carbon (C-AC) are presented in Figure 27.

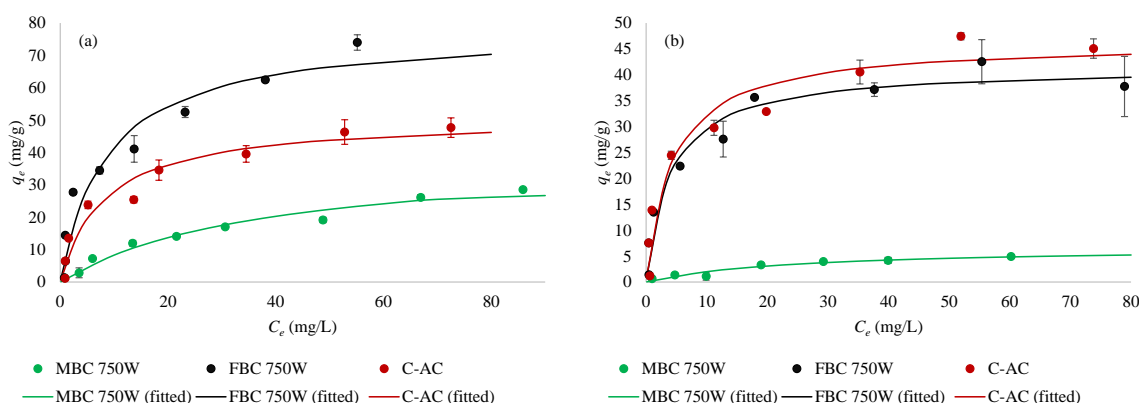
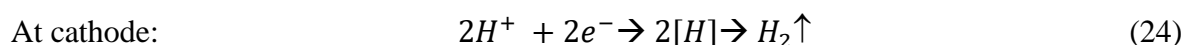
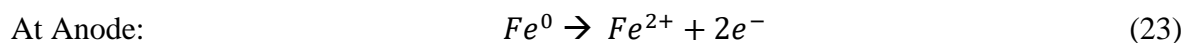


Figure 27 Adsorption isotherms of different adsorbents for ciprofloxacin (a) and diclofenac (b) at adsorbent dosage 0.7 g/L and contact time 180 mins.

According to the Figure 27, both C-AC and FBC 750W had higher adsorption capacity than MBC 750W. Further, the adsorption performance of FBC 750W was better than C-AC for ciprofloxacin at given working conditions. A main reason for this could be the very small specific surface area of MBC 750W ( $35.66 \text{ m}^2$ ) compared to FBC 750W ( $201.15 \text{ m}^2/\text{g}$ ) and C-AC ( $650 \text{ m}^2/\text{g}$ ) and underdeveloped pores (Table 6). The maximum Langmuir adsorption capacity for adsorption of ciprofloxacin was 39.08, 78.06 and 50.97 mg/g by MBC 750W, FBC 750W and C-AC, respectively. The adsorption by C-AC was slightly better in the case of diclofenac as for MBC 750W, FBC 750W and C-AC the maximum Langmuir adsorption capacities were found to be 6.77, 41.52 and 46.39 mg/g, respectively. The specific surface area of FBC 750W was lower than C-AC but still showed comparative or even better adsorption performance than C-AC. The adsorption process is governed by potential adsorption capacity and affinity for adsorbate molecules. Since the C-AC had higher specific surface area, it has higher space available for adsorption of pharmaceuticals. However, the result show that adsorption capacity of FBC 750W was higher or comparable to that of C-AC for ciprofloxacin and diclofenac, respectively. Thus, suggesting that FBC 750W could have higher density of sorption sites and larger affinity for the studied pharmaceuticals.

Previous studies have also suggested that the presence of iron could enhance removal of pharmaceutical (Wurzer et al., 2021). Additionally, the presence of zero-valent iron and iron carbide can further degrade the pharmaceuticals through redox reactions (Zhao et al., 2019, 2020; Meng et al., 2021; Li et al., 2021a). The  $\text{Fe}^0$ -carbon system could form electrolysis

cells where zero-valent iron could act as an anode and graphitic carbon act as a cathode (Li et al., 2021a). The cathode and anode reactions are provided by following equations:



At anode, the zero valent iron oxidises to ferrous ions whereas at cathode the hydrogen ion from water is reduced to atomic hydrogen. The hydrogen atoms could combine to form molecular hydrogen or the react unsaturated functional groups in organic pollutants. On the other hand, the hydroxyl ions in the system increases causing rise in pH. At neutral and alkaline conditions, ferric hydroxides are formed which can flocculate and precipitate with suspended substances present in water (Li et al., 2021a). Also, the rise in alkalinity forms ferric hydroxide layer over  $Fe^0$  surface to inactivate it. In another study, it was shown that, under anaerobic conditions,  $Fe_3C$  produced hydrogen atoms in water which dechlorinated trichloroethene through hydrogenolysis reaction (Meng et al., 2021). Also, in the study by Zhao et al. (2020) the  $Fe^0/Fe_3C/C$  composites were used for removal of oxytetracycline and chloramphenicol. The iron-based components activated dissolved oxygen in water to form free radicals such as singlet oxygen and hydroxyl radicals which oxidized the studied pharmaceuticals. Moreover, the iron was protected against inactivation due to the graphitic shell. So, it can be hypothesized that iron present in FBC 750W participated in degradation of studied pharmaceuticals. Therefore, future studies are required to verify the form, role, reaction mechanism, effect of pH and stability of iron in the removal of pharmaceuticals when using FBC 750W.

#### 5.2.6 Effect of competing ions

The removal efficiencies for ciprofloxacin and diclofenac by FBC 750W in presence of different salts, at 1 mM and 2 mM concentration, are shown presented in Figure 28 (a) and 28 (b), respectively.

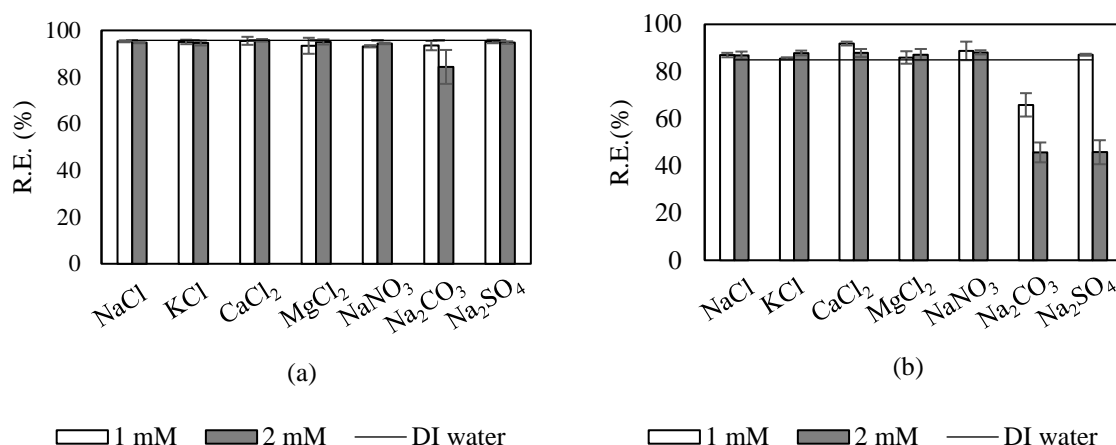


Figure 28. Effect of competing ions on removal efficiency of ciprofloxacin (a) and diclofenac (b) at adsorbent dosage 0.7 g/L, initial adsorbate concentration 10 mg/L and contact time 180 min.

According to Figure 28 (a), only sodium carbonate interfered with the removal efficiency of the ciprofloxacin onto FBC 750W. During experiments, the presence of 1 mM and 2 mM Na<sub>2</sub>CO<sub>3</sub> in ciprofloxacin solution slightly decreased the absorbance of UV-vis light even before adsorption due to increase in pH (10.48 for 1mM and 10.78 for 2mM). At this elevated pH, the absorbance of UV-vis light at 273 nm by ciprofloxacin was lesser than at pH 7. In a previous study by Patel et al (2021) presence of single valent cations did not interfere but divalent cations (Ca<sup>2+</sup> and Mg<sup>2+</sup>) had significantly decreased removal efficiency of ciprofloxacin by biochar, at 10 mM concentration. In the same study, the presence of anions (Cl<sup>-</sup> and SO<sub>4</sub><sup>2-</sup>) increased removal efficiency, however, the presence of HCO<sub>3</sub><sup>-</sup> decreased the removal efficiency of ciprofloxacin. Thus, in this study, concentrations of Ca<sup>2+</sup> and Mg<sup>2+</sup> were likely insufficient to have any observable effect on the removal efficiency.

In case of diclofenac (Figure 28 (b)), the removal efficiency was affected by both sodium carbonate and sodium sulphate. Also, increasing their concentration lowered the removal efficiency of diclofenac to a greater degree. Unlike the case of ciprofloxacin, change in pH due to addition of Na<sub>2</sub>CO<sub>3</sub> did not affect UV absorbance of diclofenac. Moreover, sodium chloride did not interfere with the diclofenac, therefore, it can be inferred that multi-charged anions such as carbonate and sulphate ions interfered with the adsorption of diclofenac. The reduction in adsorptive removal of diclofenac by biochar due to presence of anions with multiple negative charges was previously reported by Shirani et al. (2020), where



electrostatic repulsion between anions and diclofenac interfered with adsorption process. So, this result indirectly shows that electrostatic attraction plays a significant role in adsorption of diclofenac onto FBC 750W.

### 5.3 Continuous adsorption studies

The adsorption performance of fixed-bed columns, containing FBC 750W as adsorbent, was evaluated during the continuous adsorption studies. Altogether four experimental runs with different adsorbent amounts (50 and 100 mg) and flow rates (1 and 2 mL/min) for each pharmaceutical were conducted. The influent concentration was constant at 10 mg/L. For each experimental run, the breakthrough curves were plotted to observe the effects of flow rate and adsorbent amount on the dynamic breakthrough. Furthermore, column parameters such as bed height, effluent volume, total operation time were measured. Moreover, removal efficiency and bed capacity were calculated from the breakthrough curve. Additionally, breakthrough curves were fitted with two empirical models, the Bohart-Adams model and the Fractal-like Bohart-Adams model, to ascertain adsorption behaviour. The breakthrough curve and the fitted models for the adsorption of ciprofloxacin are represented in Figure 29.

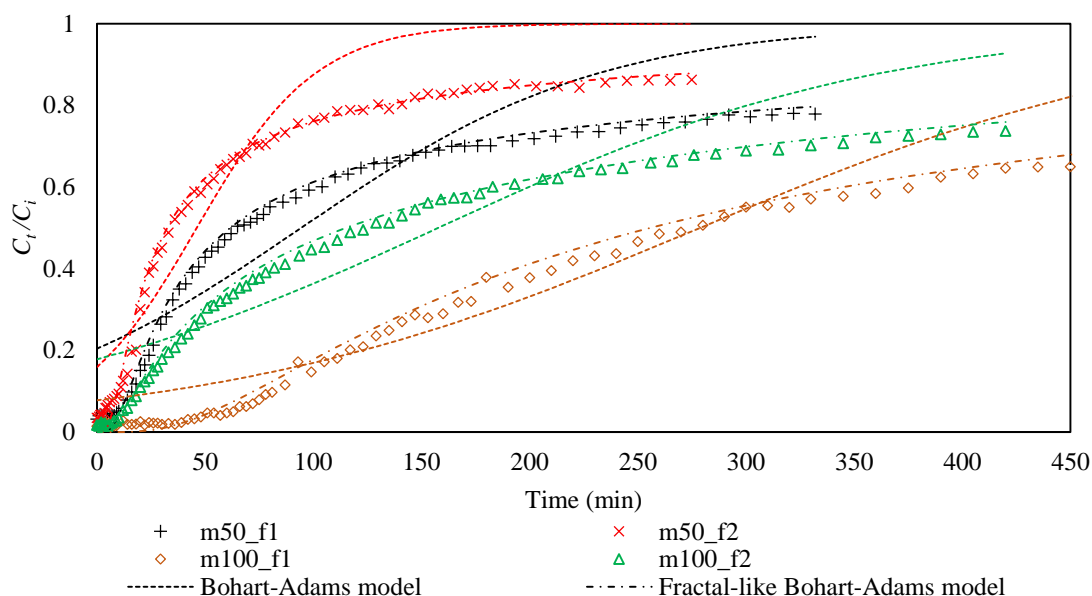


Figure 29. Breakthrough curves from fixed-bed adsorption study of ciprofloxacin at different amount of FBC 750W (50 and 100 mg) and flow rate (1 and 2 mL/min) at constant influent concentration (10 mg/L).

The effect of flow rate and adsorbent amount on the breakthrough curve can be seen from Figure 29. At a constant flowrate, increase in the adsorbent amount delayed breakthrough time and flattened the breakthrough curve. This pattern is due to positive correlation between adsorbent amount with bed height, contact time, and overall adsorption capacity (Alatalo et al., 2019; Lonappan et al., 2019). Increasing adsorbent amount increases bed height which allows longer contact time for interaction between adsorbate and adsorbent. Additionally, higher adsorbent amount has more surface available for adsorption. Therefore, increasing adsorbent amount delays breakthrough and exhaustion due to higher bed capacity.

For same adsorbent amount, increasing flow rate hastened breakthrough time and steepened the breakthrough curve. The flow rate is inversely related to thickness of hydrodynamic layer surrounding the adsorbent and contact time with adsorbent (Lonappan et al., 2019). At low flow rate, the hydrodynamic layer around the adsorbent is thicker but adsorbate has more time to efficiently interact with adsorbent. Thus, the breakthrough is achieved later. At high flow rate, the hydrodynamic layer around the adsorbent is thinner and mass transfer resistances are smaller (Lonappan et al., 2019). So, there is a faster adsorption rate at higher flow rate (Shirani et al., 2020). However, increasing flow rate diminishes contact time between adsorbate solution and adsorbent resulting in an inefficient interaction between adsorbate molecules and adsorbent surface, causing an early breakthrough. Similar results were reported in previous study where increasing flow rate decreased the breakthrough time (Alatalo et al., 2019; Shirani et al., 2020). Overall, the flowrate and the adsorbent amount had antagonistic interaction on breakthrough time, breakthrough curve steepness and exhaustion time.

Similar effects of the flow rate and the adsorbent amount were also seen in the fixed bed experiments for adsorption of diclofenac. The breakthrough curve and the fitted models for the adsorption of diclofenac are represented in Figure 30.

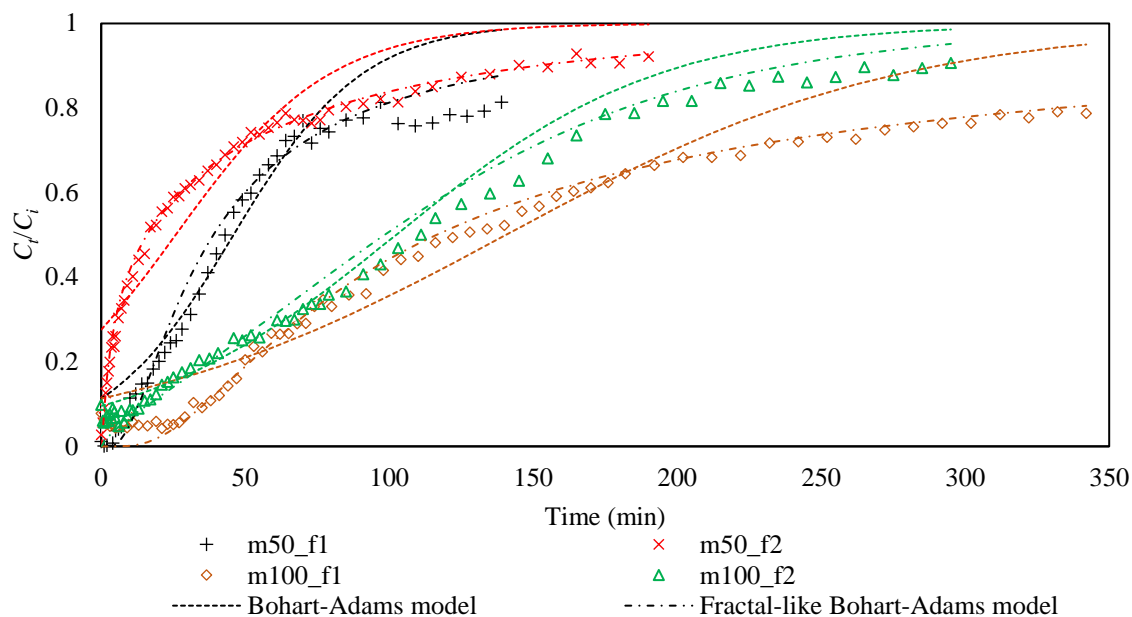


Figure 30. Breakthrough curves from fixed-bed adsorption study of diclofenac at different amount of FBC 750W (50 and 100 mg) and flow rate (1 and 2 mL/min) at constant influent concentration (10 mg/L).

According to Figure 30, increasing flow rate increased steepness of breakthrough curve, hastened breakthrough, and exhaustion points. Conversely, adsorbent amount lowered steepness of breakthrough and delayed breakthrough and exhaustion points. The parameters used for fixed-bed columns and the result for fixed-bed adsorption performance for each pharmaceutical are shown in Table 11.

Table 11. Fixed bed parameters for adsorption of ciprofloxacin and diclofenac onto FBC 750W.

Pharmaceutical	Ciprofloxacin				Diclofenac			
Run	1	2	3	4	1	2	3	4
Experiment name	m50_f1	m50_f2	m100_f1	m100_f2	m50_f1	m50_f2	m100_f1	m100_f2
$m_{ads}$ [mg]	50.4	50.37	100.75	101.20	50.21	50.92	99.50	102.10
$Q$ [mL/min]	1.01	2.04	1.00	2.02	1.01	2.12	1.03	1.98
$Z$ [cm]	0.27	0.29	0.52	0.52	0.22	0.24	0.37	0.39
Total time [min]	334	291	494	424	140	185	337	308
$V_{eff}$ [mL]	336	595	494	858	138	393	345	611
$C_i$ [mg/L]	8.48	10.42	8.88	10.78	9.74	9.82	10.46	10.46
$C_{eff}$ [mg/L]	5.22	7.58	3.66	5.98	5.82	7.43	5.46	6.34
$q_b$ [mg/g]	21.72	32.42	25.57	40.67	11.55	18.43	17.35	24.69
$R.E.$ [%]	38.64	28.13	60.47	44.94	42.21	23.62	49.14	43.03

According to Table 11, both flow rate and adsorbent amount affected adsorption performances of used fixed beds. Increasing the adsorbent amount in fixed beds increased bed height, total operating time, total treated volume, and adsorption capacity while the effluent concentration decreased. When the bed height increases, the residence time of adsorbate solution in the column also increases which allows for better interaction and intra-particle diffusion (Alatalo et al., 2019; Lonappan et al., 2019). Consequently, the removal efficiency and bed capacity are higher at higher adsorbent amount. Also, there is a lower effluent concentration, higher treated volume, and longer time for saturation.

As can be seen from Table 11, increasing the flow rate decreased total operating time, total treated volume, and removal efficiency while it increased the bed capacity and effluent concentration. Similar effects of flow rate were observed in a previous study (Shirani et al., 2020), except for the effect of flow rate on bed capacity. Increasing the flow rate increases the superficial velocity of the adsorbate solution due to which adsorbate molecules do not have adequate time to interact with the adsorbent (Du et al., 2018) and the full adsorption potential of the adsorbent is not realized. Thus, increasing flow rate decreases the bed capacity and removal efficiency. However, in this study, the inverse relation between flow rate and bed capacity was seen. In this study, the column operations were terminated prematurely because the breakthrough curves started to plateau before full saturation (Figure 29 and 30). Consequently, full adsorption capacity was not achieved and a proper comparison of adsorption capacity between different flow rates could not be made.

During the batch kinetics studies, it was found that intraparticle diffusion took part in adsorption process. So, the decrease in adsorption rate could be due to intraparticle diffusion (Hu et al., 2020). Due to lower mass transfer resistances in surface diffusion than intraparticle diffusion (Luo et al., 2019), rapid adsorption takes place onto the surface of FBC 750W. Therefore, a steep rise in adsorption occurs. As the surface becomes saturated intra particle diffusion becomes more dominant over the adsorption process. Since the intraparticle diffusion is slower, the rate of adsorption also decreases.

Nevertheless, in the case of adsorption of both pharmaceuticals, the maximum bed capacity (40.67 and 24.69 mg/g for CIP and DIC, respectively) was achieved when  $m_{ads} = 100$  mg

and  $Q = 2$  mL/min, and the highest removal efficiency (60.47% and 49.14% for CIP and DIC, respectively) was obtained when  $m_{\text{ads}} = 100$  mg and  $Q = 1$  mL/min for adsorption of both pharmaceutical.

The calculated parameters and error function values of the models fitted to breakthrough curves during column adsorption of ciprofloxacin are presented in Table 12.

Table 12. Result of fitting model to breakthrough curves of ciprofloxacin

Model	Parameters	Experimental Run			
		1	2	3	4
<b>Bohart-Adams model</b> $\frac{C_t}{C_i} = \frac{1}{1 + \exp\left(K_{\text{BA}} * C_i * \left(\frac{N_0 * Z}{u * C_i} - t\right)\right)}$	$K_{\text{BA}}$ [ $\times 10^{-3}$ L/mg/min]	1.70	3.50	1.00	0.90
	$q_b$ [mg/g]	17.18	20.75	26.39	36.53
	$R^2$	0.81	0.87	0.92	0.83
	RMSE	0.12	0.11	0.07	0.11
<b>Fractal like Bohart-Adams model</b> $\frac{C_t}{C_i} = \frac{1}{1 + \exp\left(K_{\text{BA0}} * C_i * t^{-h} \left(\frac{N_0 * Z}{u * C_i} - t\right)\right)}$	$K_{\text{BA0}}$ [ $\times 10^{-3}$ L/mg/min <sup>h</sup> ]	36.80	47.70	19.20	10.3
	$q_b$ [mg/g]	11.21	14.58	24.23	26.64
	h	0.71	0.73	0.62	0.56
	$R^2$	0.99	0.99	0.99	0.99
	RMSE	0.02	0.02	0.01	0.01

According to Table 12, fractal-like Bohart Adams model had higher  $R^2$  value and lower RMSE value, indicating good fit. Furthermore, graphical representation of the model followed closely to the actual breakthrough (Figure 29). However, the bed capacity calculated from the model was much lower than the experimental bed capacity. The “h” value from Fractal-like Bohart-Adams model indicates the adsorption system is heterogenous adsorption system (Hu et al., 2020). Also, the heterogeneity of the adsorption system was affected by increasing the adsorbate amount but was not significantly affected by the flow rate.

Conversely, the Bohart-Adams model had lower  $R^2$  and RMSE values. The Bohart-Adams model represents  $C_t/C_i$  as a symmetrical logistic function of time (S-shaped curve) but the breakthrough curves were asymmetrical. Thus, proper fitting Bohart-Adams models onto their respective breakthrough curves were not possible, as seen in Figure 29. However, the model was still able to predict bed capacity better than the fractal-like model. The results of

fitting Bohart-Adams and Fractal-like Bohart-Adams model to the breakthrough curves for adsorption of diclofenac are shown in Table 13.

Table 13. Result of fitting model to break though curves of diclofenac

Model	Parameters	Experimental Run			
		1	2	3	4
<b>Bohart-Adams model</b> $\frac{C_t}{C_i} = \frac{1}{1 + \exp\left(K_{BA} * C_i * \left(\frac{N_0 * Z}{u * C_i} - t\right)\right)}$	$K_{BA}$	4.60	3.80	1.40	2.10
	$[\times 10^{-3}]$				
	$q_b$ [mg/g]	9.73	11.35	17.11	23.45
	$R^2$	0.91	0.87	0.91	0.97
	RMSE	0.09	0.09	0.09	0.04
<b>Fractal like Bohart-Adams model</b> $\frac{C_t}{C_i} = \frac{1}{1 + \exp\left(K_{BA0} * C_i * t^{-h} \left(\frac{N_0 * Z}{u * C_i} - t\right)\right)}$	$K_{BA0}$	42.90	16.60	26.70	4.50
	$[\times 10^{-3}]$				
	$q_b$ [mg/g]	8.24	6.97	14.01	22.15
	$h$	0.62	0.46	0.65	0.20
	$R^2$	0.98	0.99	0.99	0.99
	RMSE	0.04	0.01	0.01	0.01

Similar results were obtained from fitting Bohart-Adams and Fractal-like Bohart-Adams model to the breakthrough curve for fixed-bed adsorption of diclofenac. As shown in Table 13, based on the  $R^2$  and RMSE values, fractal-like Bohart-Adams model showed best fit. Increasing flowrate and adsorbent amount decreased value of “h” and adsorption system became more homogenous. Also, like the adsorption of ciprofloxacin, classical Bohart-Adams model was better at predicting the bed capacity.

For practical application, removal efficiency, adsorption capacity as well as steepness of breakthrough curve matters (Alberti et al., 2012). Adsorption performance was best at minimum flow rate and maximum adsorbent amount. However, breakthrough occurred in already in first few minutes of operation and breakthrough curve started to plateau before reaching exhaustion. Consequently, the full adsorption potential of FBC 750W was not realised and removal efficiencies were not satisfactory in fixed-bed adsorption studies. Therefore, FBC 750W, as prepared, might not be suitable for fixed bed adsorption.

## 6 Conclusions

The main aim of this work was to synthesize biochar from iron-containing and iron-free microalgae and to study the adsorption of diclofenac and ciprofloxacin onto the synthesized biochar. This study showed that a potential adsorbent could be made from pyrolysis of microalgae harvested by a low-cost and rapid technique, coagulation of with  $\text{FeCl}_3$ . The Fe modified biochar prepared at 750 °C (FBC 750W) had improved adsorption performance compared to pristine microalgal biochar prepared at 750 °C (MBC 750W). Moreover, the adsorption capacity of FBC 750W was higher than and comparable to a commercial activated carbon for adsorption of ciprofloxacin and diclofenac, respectively. The main reason to select microalgal biochar was that microalgae are a sustainable and renewable source that biofixes carbon dioxide and can be cultivated in nutrient-rich wastewater (Goswami et al., 2021; Singh et al., 2021) and microalgal biochar has higher density of oxygen and nitrogen containing functional groups which interact with organic pollutants.

The effects of Fe during pyrolysis of the microalgal biomass were revealed during the characterization studies. Nitrogen adsorption-desorption experiments provided specific surface area, pore volumes and pore characteristics of microalgal biochar samples. Compared to MBC 750W, FBC 750W had more than five times larger specific surface area and four times more pore volumes. It was observed that both biochar samples were aggregates of platelike particles forming slit-shaped pores. Elemental analyses and FTIR analyses showed that biochar samples were enriched with carbon, aromatic groups, different oxygen-containing and nitrogen-containing functional groups, and minerals (such as calcium and phosphorus). XRD analysis showed that pyrolysis at 750 °C formed graphitic carbon in both MBC 750W and FBC 750W. Additionally, FBC 750W (both before and after adsorption) contained iron in the form of  $\text{Fe}^0$  and  $\text{Fe}_3\text{C}$  composites. Therefore, presence of iron in microalgal biomass formed porous modified biochar with higher specific surface and contained graphitic carbon, zero valent iron and iron carbide. The result was in agreement with previous studies where biomass/carbon was pyrolyzed with iron salts in inert atmosphere and at high temperature (Hoch et al., 2008; Zhao et al., 2020; Liu et al., 2021).

In this study, detailed investigation was conducted for adsorption of ciprofloxacin and diclofenac onto FBC 750W. After the adsorption of ciprofloxacin and diclofenac, the micropore volume of FBC 750W decreased. Additionally, the elemental composition of FBC 750W showed the presence of fluorine. Moreover, FTIR analysis revealed the presence of C-F bond after adsorption with ciprofloxacin. Thus, the adsorption of ciprofloxacin onto FBC 750W was verified. However, distinguishing peaks, related to diclofenac, were not observed in the FTIR spectra of FBC 750W after adsorption with diclofenac. Overall, the results from the characterization study provided adequate evidence indicating that the adsorption occurred between studied pharmaceuticals and FBC 750W.

The batch studies showed that FBC 750W has a good potential as an adsorbent material for pharmaceuticals. The maximum Langmuir adsorption capacities of FBC 750W for ciprofloxacin and diclofenac were 75.97 mg/g and 40.99 mg/g, respectively. Moreover, the adsorption isotherm of diclofenac and ciprofloxacin was described by Langmuir and Freundlich isotherm models, respectively. During adsorption, diclofenac formed a monolayer whereas the ciprofloxacin formed multilayer over the FBC 750W surface, as confirmed by the fitted isotherm models. Further, surface of FBC 750W had heterogeneous affinity for both diclofenac and ciprofloxacin and adsorption occurred via chemisorption, as indicated by the kinetics study. Moreover, adsorption occurred via combination of film diffusion and intraparticle diffusion. Comparative studies showed that adsorption capacities of FBC 750W for ciprofloxacin and diclofenac were 153.15% and 89.50%, respectively to that of commercially available granular activated carbon. Lastly, adsorption for ciprofloxacin was not hindered by competing ions whereas, for diclofenac, it was severely hindered by multi-charged anions.

Continuous adsorption studies using fixed-bed columns showed effects of different operating parameters such as flow rate and adsorbent amount on breakthrough behavior, adsorption capacity and removal efficiency. The highest adsorption capacity was achieved for ciprofloxacin (40.67 mg/g) and diclofenac (24.69 mg/g) at a flow rate of 2 mL/min and an adsorbent amount of 100 mg. However, exact comparison of adsorption capacities at different flow rates could not be made because adsorbent did not achieve same saturation levels at different flow rates. The breakthrough curves were fitted with column kinetics models, where the classical Bohart-Adams model was better at predicting bed capacity than



the Fractal-like Bohart-Adams model even though the latter had a higher correlation coefficient and lower RMSE. Nevertheless, the good fit from the Fractal-like Bohart-Adams model showed that the adsorption was heterogeneous. In all the experimental runs, the breakthrough curve occurred early and started to plateau before exhaustion. So, the maximum adsorption capacity of FBC 750W was not realized. Therefore, the synthesized FBC 750W might not be suitable for continuous adsorption systems using fixed beds.

Further studies are still required for determining the practical use of FBC 750W. The biochar was introduced as an economic alternative to the activated carbon (De Andrade et al., 2018). The adsorption capacity of FBC 750W was comparable to that of a commercial activated carbon. So, further studies could focus on the economic and environmental performance of FBC 750W and compare it to that of activated carbon. Additionally, the adsorption process can be economical when the adsorbate is regenerated and reused. Therefore, a low-cost, environmentally friendly, and efficient regeneration of spent biochar should be investigated (Cheng et al., 2021). Next, FBC 750W contained iron carbide and zerovalent iron which could degrade pharmaceuticals through redox reactions (Li et al., 2021b). Hence, the role of iron contained in FBC 750W for the degradation and reduction of pharmaceuticals could be investigated. The biochar is used for the treatment of water. So, stability of FBC 750W and associated toxicity regarding its use should be studied. More specifically, the generation of toxic secondary pollutant or leaching of toxic products from FBC 750W in water should be examined (Rizzo et al., 2020). Lastly, the adsorption performance of FBC 750W on different pollutants in real wastewater samples should be studied because real wastewater is complex matrix whose characteristics is not always constant.

## Reference

- Afzal, M. Z. et al. (2018) 'Enhancement of Ciprofloxacin Sorption on Chitosan/Biochar Hydrogel Beads', *Science of the Total Environment*, 639, pp. 560–569. doi: <https://doi.org/10.1016/j.scitotenv.2018.05.129>
- Al-Ghouti, M. A. and Da'ana, D. A. (2020) 'Guidelines for the Use and Interpretation of Adsorption Isotherm Models: A Review', *Journal of Hazardous Materials*, 393, p. 122383. doi: <https://doi.org/10.1016/j.jhazmat.2020.122383>
- Alatalo, S. M. et al. (2019) 'Mechanistic Insight into Efficient Removal of Tetracycline from Water by Fe/Graphene', *Chemical Engineering Journal*, 373, pp. 821–830. doi: <https://doi.org/10.1016/j.cej.2019.05.118>
- Alberti, G. et al. (2012) 'Beyond the Synthesis of Novel Solid Phases: Review on Modelling of Sorption Phenomena', *Coordination Chemistry Reviews*, 256, pp. 28–45. doi: <https://doi.org/10.1016/j.ccr.2011.08.022>
- De Andrade, J. R. et al. (2018) 'Adsorption of Pharmaceuticals from Water and Wastewater Using Nonconventional Low-Cost Materials: A Review', *Industrial and Engineering Chemistry Research*, 57(9), pp. 3103–3127. doi: <https://doi.org/10.1021/acs.iecr.7b05137>
- Ashiq, A., Adassooriya, N. M., et al. (2019) 'Municipal Solid Waste Biochar-Bentonite Composite for the Removal of Antibiotic Ciprofloxacin from Aqueous Media', *Journal of Environmental Management*, 236, pp. 428–435. doi: <https://doi.org/10.1016/j.jenvman.2019.02.006>
- Ashiq, A., Sarkar, B., et al. (2019) 'Sorption Process of Municipal Solid Waste Biochar-Montmorillonite Composite for Ciprofloxacin Removal in Aqueous Media', *Chemosphere*, 236, p. 124384. doi: <https://doi.org/10.1016/j.chemosphere.2019.124384>
- Bach, Q. V. and Chen, W. H. (2017) 'Pyrolysis Characteristics and Kinetics of Microalgae via Thermogravimetric Analysis (TGA): A State-of-the-Art Review', *Bioresource Technology*, 246, pp. 88–100. doi: <https://doi.org/10.1016/j.biortech.2017.06.087>
- Binda, G. et al. (2020) 'Comprehensive Comparison of Microalgae-Derived Biochar from Different Feedstocks: A Prospective Study for Future Environmental Applications', *Algal Research*, 52, p. 102103. doi: <https://doi.org/10.1016/j.algal.2020.102103>
- Bohart, G. S. and Adams, E. Q. (1920) 'Some Aspects of the Behavior of Charcoal with Respect to Chlorine', *Journal of the American Chemical Society*, 42(3), pp. 523–544. doi:

<https://doi.org/10.1021/ja01448a018>

Bordoloi, N. et al. (2016) 'Characterization of Bio-Oil and Its Sub-Fractions from Pyrolysis of *Scenedesmus dimorphus*', Renewable Energy, 98, pp. 245–253. doi: <https://doi.org/10.1016/j.renene.2016.03.081>

Carabineiro, S. A. C. et al. (2012) 'Comparison between Activated Carbon, Carbon Xerogel and Carbon Nanotubes for the Adsorption of the Antibiotic Ciprofloxacin', Catalysis Today, 186(1), pp. 29–34. doi: <https://doi.org/10.1016/j.cattod.2011.08.020>

CHEMSRC (2020) CAS Number Search - Chemsrcc. Available at: <https://www.chemsrc.com/en/> (Accessed: 11 November 2021).

Cheng, N. et al. (2021) 'Adsorption of Emerging Contaminants from Water and Wastewater by Modified Biochar: A Review', Environmental Pollution, 273, p. 116448. doi: <https://doi.org/10.1016/j.envpol.2021.116448>

Choi, Y. K. et al. (2020) 'Adsorption Behavior of Tetracycline onto *Spirulina* sp. (Microalgae)-Derived Biochars Produced at Different Temperatures', Science of the Total Environment, 710, p. 136282. doi: <https://doi.org/10.1016/j.scitotenv.2019.136282>

Chu, K. H. (2020) 'Exponential and Logistic Functions: the Two Faces of the Bohart-Adams Model', Journal of Hazardous Materials, 389, pp. 2–5. doi: <https://doi.org/10.1016/j.jhazmat.2020.122025>

Clara, M. et al. (2005) 'Removal of Selected Pharmaceuticals, Fragrances and Endocrine Disrupting Compounds in a Membrane Bioreactor and Conventional Wastewater Treatment Plants', Water Research, 39(19), pp. 4797–4807. doi: <https://doi.org/10.1016/j.watres.2005.09.015>

Crittenden, J. C. et al. (2012) MWH's Water treatment principles and design. 3rd edn. Hoboken, N.J: John Wiley and Sons Ltd.

Dąbrowski, A. (2001) 'Adsorption - From Theory to Practice', Advances in Colloid and Interface Science, 93, pp. 135–224. doi: [https://doi.org/10.1016/S0001-8686\(00\)00082-8](https://doi.org/10.1016/S0001-8686(00)00082-8)

Dai, Y. et al. (2019) 'The Adsorption, Regeneration and Engineering Applications of Biochar for Removal Organic Pollutants: A Review', Chemosphere, 223, pp. 12–27. doi: <https://doi.org/10.1016/j.chemosphere.2019.01.161>

Daneshvar, E. et al. (2017) 'A Comparative Study of Methylene Blue Biosorption using Different Modified Brown, Red and Green Macroalgae – Effect of Pretreatment', Chemical Engineering Journal, 307, pp. 435–446. doi: <https://doi.org/10.1016/j.cej.2016.08.093>

Daneshvar, E. et al. (2020) 'Performance Evaluation of Different Harvesting Methods and

- Cultivation Media on the Harvesting Efficiency of Microalga and Their Fatty Acids Profile', *Fuel*, 280, p. 118592. doi: <https://doi.org/10.1016/j.fuel.2020.118592>
- Daughton, C. G. and Ternes, T. A. (1999) 'Pharmaceuticals and Personal Care Products in the Environment: Agents of Subtle Change?', *Environmental Health Perspectives*, 107, pp. 907–938. doi: <https://doi.org/10.1289/ehp.99107s6907>
- Do, D. D. (1998) *Basis of Separation, Adsorption Analysis: Equilibria And Kinetics (With Cd Containing Computer Matlab Programs)*. London: Imperial College Press. Available at: <http://search.ebscohost.com.ezproxy.cc.lut.fi/login.aspx?direct=true&db=e000xww&AN=83649&site=ehost-live> (Accessed: 13 June 2021).
- Dordio, A. and Carvalho, A. J. P. (2015) 'Removal of Pharmaceuticals in Conventional Wastewater Treatment Plants', in Barrett L. M. (ed.) *Wastewater Treatment: Processes, Management Strategies and Environmental/Health Impacts*. Hauppauge, New York: Nova Science Publishers, Inc (Environmental Science, Engineering and Technology), pp. 1–31. Available at: <https://search.ebscohost.com/login.aspx?direct=true&db=e000xww&AN=1020634&site=ehost-live>.
- Du, Z., Zheng, T. and Wang, P. (2018) 'Experimental and Modelling Studies on Fixed Bed Adsorption for Cu(II) Removal from Aqueous Solution by Carboxyl Modified Jute Fiber', *Powder Technology*, 338, pp. 952–959. doi: <https://doi.org/10.1016/j.powtec.2018.06.015>
- Ebert, I. et al. (2011) 'Toxicity of the Fluoroquinolone Antibiotics Enrofloxacin and Ciprofloxacin to Photoautotrophic Aquatic Organisms', *Environmental Toxicology and Chemistry*, 30(12), pp. 2786–2792. doi: <https://doi.org/10.1002/etc.678>
- Elovich, S. Y. and Larionov, O. G. (1962) 'Theory of Adsorption from Nonelectrolyte Solutions on Solid Adsorbents', *Bulletin of the Academy of Sciences of the USSR, Division of chemical science*, 11(2), pp. 191–197. doi: <https://doi.org/10.1007/BF00908016>
- Fick, J. et al. (2009) 'Contamination of Surface, Ground, and Drinking Water From Pharmaceutical Production', *Environmental toxicology and chemistry / SETAC*, 28(12), pp. 2522–2527. doi: <https://doi.org/10.1897/09-073.1>
- Foo, K. Y. and Hameed, B. H. (2010) 'Insights into the Modeling of Adsorption Isotherm Systems', *Chemical Engineering Journal*, 156(1), pp. 2–10. doi: <https://doi.org/10.1016/j.cej.2009.09.013>
- Freundlich, H. (1924) 'Kolloidchemie und Biologie', *Die Naturwissenschaften*, 12(13), pp. 233–239. doi: <https://doi.org/10.1007/BF01505512>

- Fu, Q. et al. (2020) 'Biotransformation Changes Bioaccumulation and Toxicity of Diclofenac in Aquatic Organisms', *Environmental Science and Technology*, 54(7), pp. 4400–4408. doi: <https://doi.org/10.1021/acs.est.9b07127>
- Goswami, R. K. et al. (2021) 'Microalgae-Based Biorefineries for Sustainable Resource Recovery from Wastewater', *Journal of Water Process Engineering*, 40, p. 101747. doi: <https://doi.org/10.1016/j.jwpe.2020.101747>
- Gurav, R. et al. (2020) 'Treatment of Furazolidone Contaminated Water using Banana Pseudostem Biochar Engineered with Facile Synthesized Magnetic Nanocomposites', *Bioresource Technology*, 297, p. 122472. doi: <https://doi.org/10.1016/j.biortech.2019.122472>
- Ho, S. H. et al. (2019) 'N-doped Graphitic Biochars from C-phycocyanin Extracted Spirulina Residue for Catalytic Persulfate Activation Toward Nonradical Disinfection and Organic Oxidation', *Water Research*, 159, pp. 77–86. doi: <https://doi.org/10.1016/j.watres.2019.05.008>
- Ho, Y. S. and McKay, G. (1998) 'Sorption of Dye from Aqueous Solution by Peat', *Chemical Engineering Journal*, 70(2), pp. 115–124. doi: [https://doi.org/10.1016/S1385-8947\(98\)00076-X](https://doi.org/10.1016/S1385-8947(98)00076-X)
- Hoch, L. B. et al. (2008) 'Carbothermal Synthesis of Carbon-supported Nanoscale Zero-Valent Iron Particles for the Remediation of Hexavalent Chromium', *Environmental Science and Technology*, 42(7), pp. 2600–2605. doi: <https://doi.org/10.1021/es702589u>
- Hu, Q. et al. (2019) 'Fractal-like Kinetics of Adsorption on Heterogeneous Surfaces in the Fixed-bed Column', *Chemical Engineering Journal*, 358, pp. 1471–1478. doi: <https://doi.org/10.1016/j.cej.2018.10.165>
- Hu, Q. and Zhang, Z. (2020) 'Comment on "Exponential and Logistic Functions: The Two Faces of the Bohart–Adams Model"', *Journal of Hazardous Materials*, 394, pp. 1–6. doi: <https://doi.org/10.1016/j.jhazmat.2020.122508>
- IBI (2018) FAQs - biochar-international. Available at: <https://biochar-international.org/faqs/> (Accessed: 1 June 2021).
- Johansson, C. H., Janmar, L. and Backhaus, T. (2014) 'Toxicity of Ciprofloxacin and Sulfamethoxazole to Marine Periphytic Algae and Bacteria', *Aquatic Toxicology*, 156, pp. 248–258. doi: <https://doi.org/10.1016/j.aquatox.2014.08.015>
- Keerthan, S. et al. (2020) 'Engineered Tea-Waste Biochar for the Removal of Caffeine, a Model Compound in Pharmaceuticals and Personal Care Products (PPCPS), From Aqueous

- Media', *Environmental Technology and Innovation*, 19, p. 100847. doi: <https://doi.org/10.1016/j.eti.2020.100847>
- Krasucka, P. et al. (2021) 'Engineered Biochar – A Sustainable Solution for the Removal of Antibiotics from Water', *Chemical Engineering Journal*, 405, p. 126926. doi: <https://doi.org/10.1016/j.cej.2020.126926>
- Kumar, M. et al. (2020) 'Ball Milling as A Mechanochemical Technology for Fabrication of Novel Biochar Nanomaterials', *Bioresource Technology*, 312, p. 123613. doi: <https://doi.org/10.1016/j.biortech.2020.123613>
- Kwon, G. et al. (2020) 'A Review of Recent Advancements in Utilization of Biomass and Industrial Wastes into Engineered Biochar', *Journal of Hazardous Materials*, 400, p. 123242. doi: <https://doi.org/10.1016/j.jhazmat.2020.123242>
- Lagergren, S. (1898) 'About the Theory of So-Called Adsorption of Soluble Substances.', *Kunliga Svenska Vetenskapsakademiens*, 24, pp. 1–39.
- Langmuir, I. (1917) 'The Constitution and Fundamental Properties of Solids and Liquids', *Journal of the Franklin Institute*, 183(1), pp. 102–105. doi: [https://doi.org/10.1016/S0016-0032\(17\)90938-X](https://doi.org/10.1016/S0016-0032(17)90938-X)
- Law, X. N. et al. (2021) 'Microalgal-based Biochar in Wastewater Remediation: Its Synthesis, Characterization and Applications', *Environmental Research*, 204, p. 111966. doi: <https://doi.org/10.1016/j.envres.2021.111966>
- Lei, W. et al. (2021) 'Facile Synthesis of Fe<sub>3</sub>C Nano-particles/Porous Biochar Cathode Materials for Lithium Sulfur Battery', *Journal of Alloys and Compounds*, 853, p. 157024. doi: <https://doi.org/10.1016/j.jallcom.2020.157024>
- Leng, L. et al. (2019) 'Nitrogen containing Functional Groups of Biochar: An Overview', *Bioresource Technology*, 298, p. 122286. doi: <https://doi.org/10.1016/j.biortech.2019.122286>
- Levasseur, W., Perré, P. and Pozzobon, V. (2020) 'A Review of High Value-added Molecules Production by Microalgae in Light of the Classification', *Biotechnology Advances*, 41, p. 107545. doi: <https://doi.org/10.1016/j.biotechadv.2020.107545>
- Li, Q. et al. (2021a) 'Removal of Organic Compounds by Nanoscale Zero-valent Iron and Its Composites', *Science of the Total Environment*, 792, p. 148546. doi: <https://doi.org/10.1016/j.scitotenv.2021.148546>
- Li, X. et al. (2021b) 'Preparation and Application of Fe/biochar (Fe-BC) Catalysts in Wastewater Treatment: A Review', *Chemosphere*, 274, p. 129766. doi: <https://doi.org/10.1016/j.chemosphere.2021.129766>

<https://doi.org/10.1016/j.chemosphere.2021.129766>

Liu, Q. et al. (2021) 'Role of the Biochar Modified with ZnCl<sub>2</sub> and FeCl<sub>3</sub> on the Electrochemical Degradation of Nitrobenzene', *Chemosphere*, 275. doi: <https://doi.org/10.1016/j.chemosphere.2021.129966>

Lonappan, L. et al. (2019) 'Removal of Diclofenac using Microbiochar Fixed-bed Column Bioreactor', *Journal of Environmental Chemical Engineering*, 7(1), p. 102894. doi: <https://doi.org/10.1016/j.jece.2019.102894>

Luo, H. et al. (2019) 'Iron-rich Microorganism-Enabled Synthesis of Magnetic Biocarbon for Efficient Adsorption of Diclofenac From Aqueous Solution', *Bioresource Technology*, 282, pp. 310–317. doi: <https://doi.org/10.1016/j.biortech.2019.03.028>

Maculewicz, J. et al. (2021) 'Transformation Products of Pharmaceuticals in the Environment: Their Fate, (Eco)Toxicity and Bioaccumulation Potential', *Science of The Total Environment*, p. 149916. doi: <https://doi.org/10.1016/j.scitotenv.2021.149916>

Maged, A. et al. (2021) 'New Mechanistic Insight into Rapid Adsorption of Pharmaceuticals from Water Utilizing Activated Biochar', *Environmental Research*, 202, p. 111693. doi: <https://doi.org/10.1016/j.envres.2021.111693>

Meng, F. et al. (2021) 'Removal of Trichloroethene by Iron-based Biochar from Anaerobic Water: Key Roles of Fe/C Ratio and Iron Carbides', *Chemical Engineering Journal*, 413, p. 127391. doi: <https://doi.org/10.1016/j.cej.2020.127391>

Ok, Y. S. et al. (2018) 'Biochar from Biomass and Waste: Fundamentals and Applications', in *Biochar from Biomass and Waste: Fundamentals and Applications*. San Diego: Elsevier, pp. 3–14. doi: <https://doi.org/10.1016/C2016-0-01974-5>

Özçimen, D. and Ersoy-Meriçboyu, A. (2008) 'A Study on the Carbonization of Grapeseed and Chestnut Shell', *Fuel Processing Technology*, 89(11), pp. 1041–1046. doi: <https://doi.org/10.1016/j.fuproc.2008.04.006>

Parida, V. K. et al. (2021) 'Emerging Contaminants in Wastewater: A Critical Review on occurrence, Existing Legislations, Risk Assessment, and Sustainable Treatment Alternatives', *Journal of Environmental Chemical Engineering*, 9(5), p. 105966. doi: <https://doi.org/10.1016/j.jece.2021.105966>

Patel, H. (2019) 'Fixed-Bed Column Adsorption Study: A Comprehensive Review', *Applied Water Science*, 9(3), pp. 1–17. doi: <https://doi.org/10.1007/s13201-019-0927-7>

Patel, M. et al. (2019) 'Pharmaceuticals of Emerging Concern in Aquatic Systems: Chemistry, Occurrence, Effects, and Removal Methods', *Chemical Reviews*, 119(6), pp.

3510–3673. doi: <https://doi.org/10.1021/acs.chemrev.8b00299>

Patel, M. et al. (2021) ‘Ciprofloxacin and Acetaminophen Sorption onto Banana Peel Biochars: Environmental and Process Parameter Influences’, *Environmental Research*, 201(May), p. 111218. doi: <https://doi.org/10.1016/j.envres.2021.111218>

Peter, L. (2011) ‘IR and Raman Spectra-Structure Correlations: Characteristic Group Frequencies’, in *Infrared and Raman Spectroscopy: Principles and Spectral Interpretation*. Amsterdam: Elsevier, pp. 73–115. Available at: <http://search.ebscohost.com.ezproxy.cc.lut.fi/login.aspx?direct=true&db=e000xww&AN=367681&site=ehost-live>.

Piccin, J. S. et al. (2017) ‘Adsorption isotherms in liquid phase: Experimental, modeling, and interpretations’, in Bonilla-Petriciolet, A., Mendoza-Castillo, D. I., and Reynel-Ávila, H. E. (eds.) *Adsorption Processes for Water Treatment and Purification*, pp. 19–51. doi: [https://doi.org/10.1007/978-3-319-58136-1\\_2](https://doi.org/10.1007/978-3-319-58136-1_2)

Qiu, H. et al. (2009) ‘Critical Review in Adsorption Kinetic Models’, *Journal of Zhejiang University: Science A*, 10(5), pp. 716–724. doi: <https://doi.org/10.1631/jzus.A0820524>

Rizzo, L. et al. (2020) ‘Best Available Technologies and Treatment Trains to Address Current Challenges in Urban Wastewater Reuse for Irrigation of Crops in EU Countries’, *Science of the Total Environment*, 710, p. 136312. doi: <https://doi.org/10.1016/j.scitotenv.2019.136312>

Ronsse, F. et al. (2013) ‘Production and Characterization of Slow Pyrolysis Biochar: Influence of Feedstock Type and Pyrolysis Conditions’, *GCB Bioenergy*, 5(2), pp. 104–115. doi: <https://doi.org/10.1111/gcbb.12018>

Rouquerol, J. et al. (2014a) ‘Assessment of Mesoporosity’, in *Adsorption by Powders and Porous Solids: Principles, Methodology and Applications*. 2nd edn. Elsevier Ltd, pp. 269–302. doi: <https://doi.org/10.1016/B978-0-08-097035-6.00008-5>

Rouquerol, J. et al. (2014b) ‘Introduction’, in *Adsorption by Powders and Porous Solids: Principles, Methodology and Applications*. 2nd edn. Elsevier Ltd, pp. 1–24. doi: <https://doi.org/10.1016/B978-0-08-097035-6.00001-2>

Santhosh, C. et al. (2020) ‘Synthesis and Characterization of Magnetic Biochar Adsorbents for the Removal of Cr(VI) and Acid Orange 7 Dye from Aqueous Solution’, *Environmental Science and Pollution Research*, 27(26), pp. 32874–32887. doi: <https://doi.org/10.1007/s11356-020-09275-1>

Schwaiger, J. et al. (2004) ‘Toxic Effects of the Non-steroidal Anti-Inflammatory Drug



- Diclofenac. Part I: Histopathological Alterations and Bioaccumulation in Rainbow Trout', *Aquatic Toxicology*, 68(2), pp. 141–150. doi: <https://doi.org/10.1016/j.aquatox.2004.03.014>
- Sharma, R. et al. (2021) 'Recent Advances in Microalgae-based Remediation of Industrial and Non-Industrial Wastewaters with Simultaneous Recovery of Value-Added Products', *Bioresource Technology*, p. 126129. doi: <https://doi.org/10.1016/j.biortech.2021.126129>
- Shirani, Z., Song, H. and Bhatnagar, A. (2020) 'Efficient Removal of Diclofenac and Cephalexin from Aqueous Solution Using *Anthriscus sylvestris*-derived Activated Biochar', *Science of the Total Environment*, 745, p. 140789. doi: <https://doi.org/10.1016/j.scitotenv.2020.140789>
- Sing, K. S. W. et al. (1985) 'Reporting Physisorption Data for Gas/Solid Systems with Special Reference to the Determination of Surface Area and Porosity (Recommendations 1984).', *Pure and Applied Chemistry*, 57(4), pp. 603–619. doi: <https://doi.org/10.1351/pac198557040603>
- Singh, A. et al. (2021) 'Engineered Algal Biochar for Contaminant Remediation and Electrochemical Applications', *Science of the Total Environment*, 774, p. 145676. doi: <https://doi.org/10.1016/j.scitotenv.2021.145676>
- Singh, G. and Patidar, S. K. (2018) 'Microalgae Harvesting Techniques: A Review', *Journal of Environmental Management*, 217, pp. 499–508. doi: <https://doi.org/10.1016/j.jenvman.2018.04.010>
- Sips, R. (1948) 'On the Structure of a Catalyst Surface', *The Journal of Chemical Physics*, 16(5), pp. 490–495. doi: <https://doi.org/10.1063/1.1746922>
- Sodhi, K. K. and Singh, D. K. (2021) 'Insight into the Fluoroquinolone Resistance, Sources, Ecotoxicity, and Degradation with Special Emphasis On Ciprofloxacin', *Journal of Water Process Engineering*, 43, p. 102218. doi: <https://doi.org/10.1016/j.jwpe.2021.102218>
- Sousa, J. C. G. et al. (2018) 'A Review on Environmental Monitoring of Water Organic Pollutants Identified by EU Guidelines', *Journal of Hazardous Materials*, 344, pp. 146–162. doi: <https://doi.org/10.1016/j.jhazmat.2017.09.058>
- Vieira, Y. et al. (2021) 'Effective Treatment of Hospital Wastewater with High-concentration Diclofenac and Ibuprofen using a Promising Technology Based on Degradation Reaction Catalyzed by Fe<sup>0</sup> Under Microwave Irradiation', *Science of the Total Environment*, 783, p. 146991. doi: <https://doi.org/10.1016/j.scitotenv.2021.146991>
- Vieno, N. and Sillanpää, M. (2014) 'Fate of Diclofenac in Municipal Wastewater Treatment Plant - A Review', *Environment International*, 69, pp. 28–39. doi: <https://doi.org/10.1016/j.envint.2014.05.014>

<https://doi.org/10.1016/j.envint.2014.03.021>

Wang, J. et al. (2017) 'Treatment of Refractory Contaminants by Sludge-derived Biochar/Persulfate System via Both Adsorption and Advanced Oxidation Process', *Chemosphere*, 185, pp. 754–763. doi: <https://doi.org/10.1016/j.chemosphere.2017.07.084>

Wang, J. and Guo, X. (2020) 'Adsorption Kinetic Models: Physical Meanings, Applications, and Solving Methods', *Journal of Hazardous Materials*, 390(January), p. 122156. doi: <https://doi.org/10.1016/j.jhazmat.2020.122156>

Weber, W. and Morris, J. C. (1963) 'Kinetics of Adsorption on Carbon from Solution', *Journal of the Sanitary Engineering Division*, 89(2), pp. 31–59. doi: <https://doi.org/10.1061/JSEDAI.0000430>

Worch, E. (2012) 'Basic Concepts and Definitions', in *Adsorption Technology in Water treatment - Fundamentals, Processes, and Modeling*. Berlin: Walter de Gruyter, pp. 2–5. Available at: <https://app.knovel.com/hotlink/pdf/id:kt00U4CCR9/adsorption-technology/some-general-thermodynamic> (Accessed: 13 June 2021).

Wurzer, C. and Mašek, O. (2021) 'Feedstock Doping using Iron Rich Waste Increases the Pyrolysis Gas Yield and Adsorption Performance Of Magnetic Biochar For Emerging Contaminants', *Bioresource Technology*, 321. doi: <https://doi.org/10.1016/j.biortech.2020.124473>

WWAP (United Nations World Water Assessment Programme) (2017) *The United Nations World Water Development Report 2017. Wastewater: The Untapped Resource*. Paris, UNESCO.

Xia, S. et al. (2019) 'Pyrolysis of Chinese Chestnut Shells: Effects of Temperature and Fe Presence on Product Composition', *Bioresource Technology*, 287, p. 121444. doi: <https://doi.org/10.1016/j.biortech.2019.121444>

Yang, K. and Xing, B. (2010) 'Adsorption of Organic Compounds by Carbon Nanomaterials in Aqueous Phase: Polanyi Theory and Its Application', *Chemical Reviews*, 110(10), pp. 5989–6008. doi: <https://doi.org/10.1021/cr100059s>

Yang, Y. et al. (2017) 'Occurrences and Removal of Pharmaceuticals and Personal Care Products (PPCPs) in Drinking Water and Water/Sewage Treatment Plants: A Review', *Science of the Total Environment*, 596–597, pp. 303–320. doi: <https://doi.org/10.1016/j.scitotenv.2017.04.102>

Yu, K. L. et al. (2017) 'Microalgae from Wastewater Treatment to Biochar – Feedstock Preparation and Conversion Technologies', *Energy Conversion and Management*, 150, pp.

1–13. doi: <https://doi.org/10.1016/j.enconman.2017.07.060>

Zeng, S. and Kan, E. (2021) ‘Chemosphere Adsorption and Regeneration on Iron-Activated Biochar for Removal of Microcystin-LR’, *Chemosphere*, 273, p. 129649. doi: <https://doi.org/10.1016/j.chemosphere.2021.129649>

Zeng, Z. W. et al. (2018) ‘Comprehensive Adsorption Studies of Doxycycline and Ciprofloxacin Antibiotics by Biochars Prepared at Different Temperatures’, *Frontiers in Chemistry*, 6, pp. 1–11. doi: <https://doi.org/10.3389/fchem.2018.00080>

Zhao, N. et al. (2019) ‘Removal of Organic Dye by Biomass-based Iron Carbide Composite with an Improved Stability and Efficiency’, *Journal of Hazardous Materials*, 369, pp. 621–631. doi: <https://doi.org/10.1016/j.jhazmat.2019.02.077>

Zhao, N. et al. (2020) ‘Singlet Oxygen Mediated the Selective Removal of Oxytetracycline in C/Fe<sub>3</sub>C/Fe<sub>0</sub> System as Compared to Chloramphenicol’, *Environment International*, 143, p. 105899. doi: <https://doi.org/10.1016/j.envint.2020.105899>

Zhu, S. et al. (2019) ‘Iron Sludge-derived Magnetic Fe<sub>0</sub>/Fe<sub>3</sub>C Catalyst for Oxidation of Ciprofloxacin via Peroxymonosulfate Activation’, *Chemical Engineering Journal*, 365, pp. 99–110. doi: <https://doi.org/10.1016/j.cej.2019.02.011>